POLITECNICO DI TORINO

Mechatronic Engineering

Department of Electronics and Telecommunications

Master Degree Thesis

Design of a fluorescence-based microfluidic sensing device for continuous pH measurement



Supervisor:
Prof. Guido Perrone
Co-supervisor:
Dott.ssa Chiara Bellezza Prinsi

Candidate: Leonardo Degl'Innocenti

October 2025

Acknowledgments

I would like to dedicate this thesis to my grandfather, Carlo, whose unwavering encouragement and support laid the very foundations of my education. I would have loved for him to witness this milestone.

I am deeply grateful to my family, and especially my parents, Ilaria and Stefano, for their boundless love, support, and for giving me the opportunities that made this journey possible.

My friends and fellow students have shared with me the hardships and triumphs of this demanding period at university, I thank them for their priceless support.

Special thanks go to Professor Guido Perrone, whose kind guidance and the opportunity to undertake this research were a great completion of this chapter of my life. I am also profoundly indebted to Chiara for her patient mentorship; she led me through every step, leveraging the knowledge and materials from part of her own Ph.D work.

Contents

1	Introduction					
	1.1	Hydroponics				
		1.1.1 Importance of pH monitoring				
		1.1.2 Methods for pH monitoring				
		1.1.3 Other relevant parameters				
	1.2 State of the art for pH measurement					
		1.2.1 Glass-electrode potentiometry				
		1.2.2 Silicon-based ISFET (Ion-Sensitive Field-Effect Transistor)				
	1.3	Fluorescence				
		1.3.1 Jablonski Diagram				
		1.3.2 Absorption				
		1.3.3 Stokes shift				
		1.3.4 Franck-Condon principle				
		1.3.5 Fluorescence lifetime and quantum yield				
		1.3.6 Factors affecting fluorescence				
	1.4	Microfluidic circuits				
		1.4.1 Reynolds number				
		1.4.2 Navier-Stokes Equations and Stokes Flow				
		1.4.3 Exact solution to microfluidic flow equations				
		1.4.4 Navier Stokes Equations in Single Phase Microfluidics				
		1.4.5 Molecular Diffusion				
		1.4.6 Microfluidic mixing techniques				
		1.4.7 Materials and production processes for microfluidic devices				
		1.4.7.1 PDMS - Polydimethylsiloxane				
		1.4.7.2 PDMS soft lithography				
		1.4.7.3 PMMA - polymethyl-methacrylate				
		1.4.7.4 PLA - Polylactic acid				
2	Preliminary laboratory analysis 33					
	2.1	Initial analysis of the spectra obtained from the samples				
		2.1.1 Influence of temperature to the fluorescence peak				
		2.1.2 Characterization of the relation between the fluorescence peak and pH . 35				
		2.1.3 Preparation of the buffer samples				
	2.2	Simulation of a 8-channel mini-spectrometer				
	2.3	LED drift problem				
	2.4	Improvement to the tracer solution formula				
	2.5	Analysis of the obtained data				
		·				
3	Mea	asurement device prototype design 52				
	3.1	Mechanical design: microfluidic circuit for mixing				
		3.1.1 Lab tests on a scaled up version of the microfluidic circuit 58				
		3.1.2 Drift compensation mount for testing				
	3.2	Electronic design: custom PCB board				
		3.2.1 Peristaltic pumps control circuits				

			3.2.1.1 H-Bridge configuration	64
			3.2.1.2 Characterization of the peristaltic pumps	65
		3.2.2	Temperature acquisition circuit	67
		3.2.3	Battery charger circuit	69
		3.2.4	LED driver circuit	70
	3.3	Softwa	are design: data harvesting and evaluation	72
		3.3.1	Web interface to test and characterize the available peristaltic pumps	73
		3.3.2	Measurement cycle flow control	74
		3.3.3	Initial hints at a machine learning stack	75
			3.3.3.1 Effect of the LED drift on data analysis	76
	~			
4	Con	nclusio	ns	77

1 Introduction

Continuous pH control plays a key role in many sectors, such as agriculture, food processing, chemical production, and water-quality testing. In hydroponics, for example, accurate pH control is fundamental to maintain nutrient solutions suitable for plant growth. However, while many sensors are available for occasional or manual pH checks, robust solutions for real-time and continuous monitoring are still largely missing.

The main goal of this thesis is to develop the prototype of a compact pH-measurement system, designed for continuous operation and suitable for in-field operation. The proposed device relies on fluorescence analysis, exploiting the relationship between the fluorescence peak of a suitable fluorophore and pH. In particular, the experiments have been carried out using Sodium Fluorescein (Uranine), a polar dye that dissolves easily in aqueous solutions. Initial tests confirmed a clear relationship between fluorescence peak and pH but also revealed significant limitations: the very small quantity of dye compared with the sample volume made dosing highly sensitive, so even small errors caused large measurement deviations. To improve robustness, a new preparation method was developed to relax dosing tolerances, complemented by the design of a passive microfluidic mixing device capable of homogenizing the dye-sample solution without external actuation.

The complete prototype is composed of a microfluidic circuit, an electronic control board, and a software for data acquisition and management. The microfluidic circuit has been designed in Autodesk Fusion 360 and simulated in COMSOL Multiphysics, with two inlet ports and a channel geometry engineered to induce chaotic advection and promote diffusion, ensuring efficient passive mixing. The electronic board features the acquisition system, the circuits to drive peristaltic pumps, and for temperature sensing and LED excitation, and a mini-spectrometer for fluorescence detection. A custom PCB was developed in KiCad to integrate these functions. Battery powered and equipped with efficient boost and buck-boost converters, the board drives the pumps in PWM H-bridge mode, reads data from an NTC thermistor and the AS7341 mini-spectrometer, and controls the LED source. All communication and power management are consolidated through a single USB-C port, which also supports WebUSB connectivity to a browser-based interface for cross-platform use, with Bluetooth as an additional option. The data retrieval, processing, and visualization software is enhanced by the integration of machine-learning techniques to improve accuracy and adaptability.

1.1 Hydroponics

Hydroponics is a modern way to grow plants **without soil**. The word *hydroponics* derives from the ancient Greek *hydor* (water) and *ponos* (labor), underscoring water's role as the primary active medium. By providing the roots with a precisely controlled mixture of water, oxygen and dissolved macro- and micro-elements, hydroponic systems can grow crops with far less land, water and time than conventional soil agriculture. This makes hydroponics a practical option for urban farms, dry regions, and any situation where resources are limited.

Plants grown hydroponically absorb nutrients from water more efficiently than plants grown in soil. This makes the growth significantly faster.

Hydroponic systems can be grouped into two basic types:

- With substrate: plants grow in a medium such as perlite, sand, or expanded clay that is regularly watered with a nutrient solution.
- Without substrate: plants are suspended directly in a continuous flow of the nutrient solution.

In both setups, oxygen delivery is vital; insufficient oxygen can kill the plants, so the oxygenation level must be carefully monitored and controlled.

Although the fundamental idea of cultivating plants in a nutrient-rich liquid can be traced back to ancient Mesopotamia (cuneiform records from the era of the Hanging Gardens of Babylon describe water-based growing techniques) hydroponics did not become a systematic agricultural method until the twentieth century. In 1930, Dr. Gericke at the University of California, Berkeley, demonstrated controlled nutrient-solution cultivation in a laboratory setting, laying the groundwork for modern hydroponics. Over the last few decades, advances in automation, sensor technology, and closed-loop nutrient delivery have turned hydroponics into a scalable, resource-efficient, and environmentally friendly approach to mass food production.

1.1.1 Importance of pH monitoring

Definition of pH

pH is a scale used to measure the acidity or basicity of a solution. Its value goes from 0 to 14 and is related to the relative concentration of hydrogen atoms H⁺ and hydroxide ions OH⁻ in aqueous solutions. If the first prevails, we are in presence of a acidic solution, while if the second prevails we are dealing with an alkaline solution. A pH equal to 7 is considered *neutral*.

$$pH = -\log_{10}[H^+] \tag{1}$$

where $[H^+]$ is the hydrogen atom concentration.

pH is a logarithmic quantity

Each step of +1 means a solution is ten times more alkaline, while each step of -1 means a solution is ten times more acidic.

In hydroponic culture pH is a critical parameter: if the pH is too high, most nutrients become insoluble and cannot be taken up; if it is too low, the roots may suffer damage. In soil systems the natural buffering capacity of the medium maintains an acceptable pH, but in a closed hydroponic circuit the solution must be monitored and adjusted manually. The pH of the nutrient solution governs the solubility of macro- and micro-nutrients, thereby influencing plant health, growth rate, and ultimately yield. Most crops grown with this technique thrive at a slightly acidic range, which is typically $5.5 \le \text{pH} \le 6.5$. Maintaining the solution within this window ensures optimal nutrient availability and maximizes production.

pH not only affects nutrient availability, it also regulates the activity of plant enzymes that drive metabolism. A balanced pH keeps these enzymes functioning at optimal rates, while a deviation can slow growth or even shut down essential pathways. Moreover, the microbial

community that associates with roots is pH-sensitive. A well-maintained pH (5.5–6.5 in most hydroponic systems) suppresses pathogenic bacteria and supports beneficial microbes such as nitrogen-fixers. Conversely, a wrong pH can create a favorable environment for harmful microbes, leading to disease or root damage.

1.1.2 Methods for pH monitoring

Let's have a look to the three most common pH-monitoring approaches for hydroponics (from simplest to most complex):

- pH Testing Strips: thin paper pads coated with reagents that change color upon contact with a solution. The color is compared to a chart to infer the pH. Although inexpensive and easy to use for hobby or small-scale work, strips lack the precision and reproducibility required for professional, real-time monitoring, and interpreting the color can be subjective (standard expected accuracy is between 0.5 pH and 1 pH), this is not enough for serious applications. They're also single-use, so this is a cost that can easily add up over time.
- Digital pH Pens (pH Meters): handheld electronic devices that use a glass electrode (sensitive to hydrogen ions) and a reference electrode. The voltage difference between the glass electrode and a reference electrode is correlated to the H^+ concentration. The reference electrode provides a constant reference voltage. To use them they just need to be dipped inside the solution and can provide a quite accurate reading (usually within 0.01 pH). However, they require constant calibration using a specific pH calibration solution. They also require frequent battery replacement.
- **pH Controllers**: this is considered the industry-standard solution for hydroponics. They match the accuracy of digital pH meters (±0.01 pH) and add an automatic feedback loop that adjusts the solution's pH with dosing pumps, keeping the level within the desired range without manual intervention.

1.1.3 Other relevant parameters

Other critical parameters that must be tightly regulated in a hydroponic system include temperature, humidity, CO_2 concentration, light intensity and photoperiod, ventilation, and pathogen presence.

1.2 State of the art for pH measurement

Let's analyze a couple of technologies that are frequently employed to measure pH.

1.2.1 Glass-electrode potentiometry

A glass membrane that is selective for H^+ ions measures the potential compared to a reference (usually Ag). This method has a very high accuracy (around ± 0.01 pH and a broad range), but requires calibration and it's temperature-sensitive. The **Nerst Equation** is used to calculate the electrochemical Zn-Cu cell potential at any known pressure, temperature, and concentration. The electrochemical cell consists of two half-cells, each containing a different

electrode immersed in an electrolyte solution. A conductive pathway allows electrons to freely flow between them.

$$E = E^0 - \frac{RT}{nF} \ln Q \tag{2}$$

where E is the cell potential under non-standard conditions, E^0 is the cell potential under standard conditions, R is the universal gas constant, F is the Faraday constant, Q is the reaction quotient (ratio of the concentrations of products to reactants at any given moment).

$$Q = \frac{[C]^{c}[D]^{d}}{[A]^{a}[B]^{b}} \tag{3}$$

where A, B, C, D are the molar concentrations of the chemical species and a, b, c, d are the coefficients from the balanced chemical equation.

In a pH-sensor, the target ion is the proton H^+ . A voltmeter connected to a Zn plate (-) and a Cu plate (+), each immersed in one of the two half-cells. The measured voltage is directly proportional to the natural logarithm of the H^+ activity (pH), which is the *only* species activity that appears in Q. Thus

$$E = E^{0} - \frac{RT}{nF} \cdot \ln\left(\frac{[H_{x}^{+}]^{2}}{[H_{ref}^{+}]^{2}}\right) = -\frac{RT}{2F} \cdot 2 \ln[H_{x}^{+}]$$
(4)

where $[H_{\text{ref}}^+]$ is the concentration of H^+ ions in the reference solution, while $[H_x^+]$ is the concentration of the H^+ ions in the solution to be measured. We finally obtain the relation

$$E = -\frac{RT}{F} \cdot \ln[H_x^+] \tag{5}$$

This means that the measurement of the cell potential provides a direct measurement of pH.

1.2.2 Silicon-based ISFET (Ion-Sensitive Field-Effect Transistor)

This method is the heart of many modern pH-pens. The working principle has at its core an *ISFET*, which is composed of:

- a **silicon channel** (p-type or n-type) as a conductive strip that carries current between source and drain;
- a Gate dielectric (e.g. SiO₂) that insulates the channel from the external solution. It also embeds a ion-selective membrane;
- a **ion-selective membrane** (glassy silicate or functionalized polymer) that only exposes H⁺ ions to the gate, effectively converting their activity into a surface charge;
- the **Source/Drain contacts** provide the source-drain current that is modulated by the gate potential.

What's being measured is the surface charge caused by the absorption of H^+ ions by the ion-selective membrane. The surface charge induces an electric field at the gate dielectric, which controls the density of charge carriers (holes or electrons, depending on the type) in the channel. The drain current I_D changes according to the Nerst equation and a microcontroller can measure it to obtain a pH value.

This solution only requires a very low power (a few μA of bias current), so a small battery is sufficient to last several days. No reference solution is needed in this case.

1.3 Fluorescence

1.3.1 Jablonski Diagram

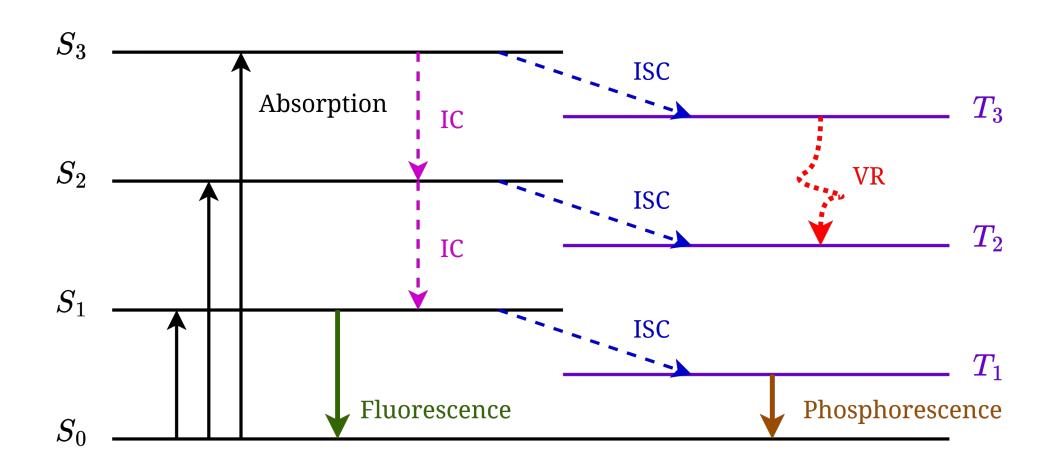


Figure 1: Jablonski diagram

The Jablonski Diagram (Figure 1) is a tool that helps to depict the electronic and vibrational energy levels of molecules:

• Singlet excited state: we obtain such a state when there's no change in the spin of the excited electron.

$$S = \frac{1}{2} + \left(-\frac{1}{2}\right) = 0\tag{6}$$

$$M_s = 2S + 1 = 2 \cdot 0 + 1 = 1 \tag{7}$$

As we can see, there is only one possible orientation of the total spin, which is characteristic of a singlet state. The total spin of the system S is zero.

• Triplet excited state: we obtain such a state when the excited electron flips its spin.

$$S = \frac{1}{2} + \frac{1}{2} = 1 \tag{8}$$

$$M_s = 2S + 1 = 2 \cdot 1 + 1 = 3 \tag{9}$$

Now there are three possible orientations of the total spin, which is characteristic of a triplet state.

The duration of the initial absorption phase lasts just 10^{-15} s. Let's now analyze the non-radiative transitions:

- ISC Internal System Crossing: Energy is dissipated in the transition between states of different spin. This transition takes between 10^{-10} to 10^{-8} s.
- IC Internal Conversion: Energy is dissipated through molecular collisions or heat. This transition takes between 10^{-11} to 10^{-9} s.

• VR - Vibrational Relaxation: Process by which an excited molecule loses vibrational energy and transitions from a higher vibrational state to a lower vibrational state within the same electronic energy level. This transition takes between 10^{-12} to 10^{-10} s.

Then there are the two radiative transitions:

- Fluorescence: This *immediate emission* (fast emission) happens as long as the process of absorption goes on. This transition takes between 10^{-10} to 10^{-7} s.
- **Phosphorescence**: This *delayed emission* (slow emission) continues even when the process of absorption stops. It's caused by a molecule returning to the ground state from the triplet excited state.

Figure 2 shows all the various luminescence process that occur in time.

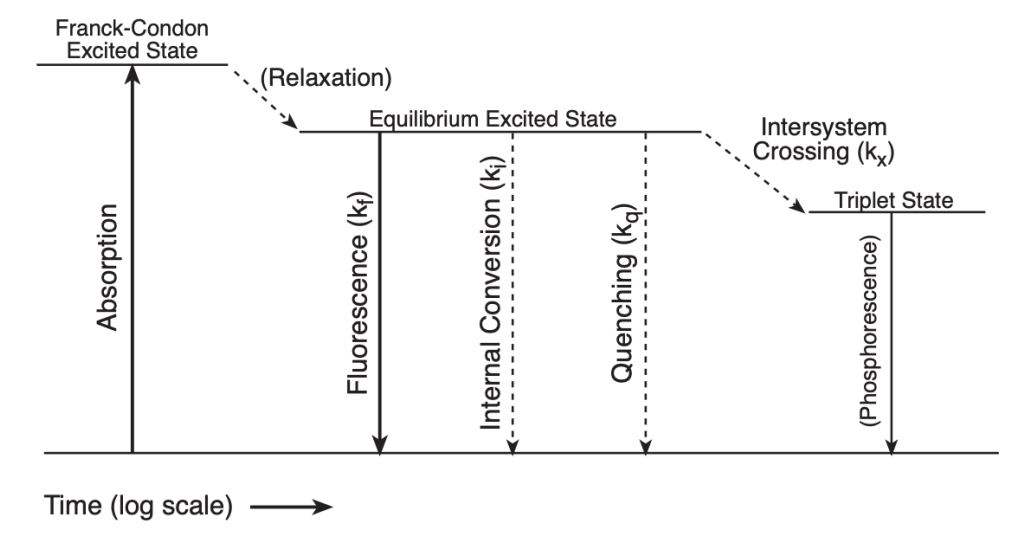


Figure 2: Summary of luminescence processes

Since fluorescence lifetimes are typically around 10^{-8} seconds, internal conversion is typically finished prior to emission. As a consequence, fluorescence emission generally comes from a thermally equilibrated excited state, and specifically the lowest energy vibrational state of S_1 . The conversion from singlet to triplet states is known as *intersystem crossing*. The opposite transition is prohibited. This leads to rate constant for triplet emission that are several orders of magnitude smaller than those for fluorescence.

There's a **similarity between absorption and emission spectra** when electronic transitions involve minimal changes in nuclear geometry. In fact, electronic excitation doesn't significantly alter it. The term *mirror* refers to the reversed direction of transitions, not the energy spacing itself.

1.3.2 Absorption

Absorption of electromagnetic radiation is how matter takes up a photon's energy and transforms it into internal energy of the absorber.

Each molecule contains the following energy orbitals (due to different types of covalent bonds):

- σ bonds (–): These are the strongest type of covalent bond. They consist in an easy head-on overlap of atomic orbitals (s-s, s-p or p-p orbitals) and this makes the attraction between the nuclei and the shared electrons very strong. They allow rotation (no effect of rotation on the overlap of orbitals) and are the first bonds that are formed.
- π bonds (=): These are weaker bonds, easier to break. Let's suppose we're dealing with p-orbitals and that one of the three (P_x, P_y, P_z) is involved in a σ bond. The other two orbitals are rotated 90° from the first one and cannot form any other σ bond with the same other atom (they aren't aligned). Consequently, the other two p-orbitals bend to form a weaker π bond. The two sideways overlap creates two areas of electron density (above and below the σ bond). Rotations are no longer allowed, as a twist would break the π bonds.
- N bonds: These are lone pairs of electrons (not bounded) and are the most energetic states.
- σ^* and π^* anti-bonds: They are formed when atomic orbitals combine in such a way that they interfere destructively. This happens when the wave functions of combining atomic orbitals are out of phase. This leads to a region of reduced electron density. A node is created and thus the bond is weakened or even negated. The associated energy is thus higher.

As more energy is required to break a sigma bond, electrons that participate in the energy jump are mostly in π and N orbitals. This means that absorption is augmented in compounds with more densely populated orbitals.

For molecules with conjugated double bonds (alternating single and double bonds between atoms in a molecule) the wavelength of maximum absorption is higher. In fact, the amount of delocalization of the bond increases.

bond delocalization increases \implies longer wavelength (shorter frequency) maximum absorption

longer wavelength maximum absorption \implies less energy to promote an electron

There's less energy gap between the bonding and anti-bonding orbitals as the amount of delocalization increases.

1.3.3 Stokes shift

The **Stokes shift** is the difference between the peak in the absorption spectra and the peak in the emission spectra corresponding to the same electronic transition.

After the transition to an excited state fueled by the absorption of a photon, a system can resume its ground state either

• by **releasing a photon** or

• by dissipating the energy in collisions with other atoms or molecules.

Main causes of Stokes shift

The main causes of the Stokes shift are

- vibrational relaxation (dissipation);
- solvent reorganization.

When a fluorophore (dipole), surrounded by solvent molecules, enters an excited state, the dipole moment changes. The surrounding solvent molecules cannot immediately re-adjust their orientation, the re-alignment process is called **vibrational relaxation**. This process requires energy and thus contributes to the falling of the molecule to a lesser excited state.

Solvent relaxation consists in the assistance of solvent molecules in the process of stabilizing and further lowering the energy level of the excited state by re-orienting around the excited fluorophore. This is a slow process that results in a **redshift** (to longer wavelengths) of the fluorescence emission.

The greater the difference in polarity between solute and solvent, the stronger is the red-shift.

1.3.4 Franck-Condon principle

The **Franck-Condon principle** is a concept in spectroscopy and quantum chemistry that describes the intensity of vibronic transitions. When a molecule absorbs or emits a photon with the appropriate energy, simultaneous alterations in the electronic and vibrational energy levels occur.

This principle states that during an electronic transition, a transition between two vibrational energy levels is more likely to happen when the overlap between their vibrational wave functions is more pronounced.

Electronic transitions are very fast compared with nuclear motions, so the favored vibrational levels are those that **correspond to minimal change in the nuclear coordinates**. Let's analyze what happens:

- 1. During the electronic transition, the nucleus remains stationary due to it having a much greater mass than the electrons.
- 2. The inter-nuclear separation (distance between the nuclei of two atoms in a molecule or a crystal) doesn't change after the absorption.
- 3. The intensity of the electronic transition is maximum between the vibration states that are arranged vertically in the different electronic states.
- 4. The Franck-Condon principle states that the transition of electrons from the ground to the excited state occurs without any change in the position of the nucleus.

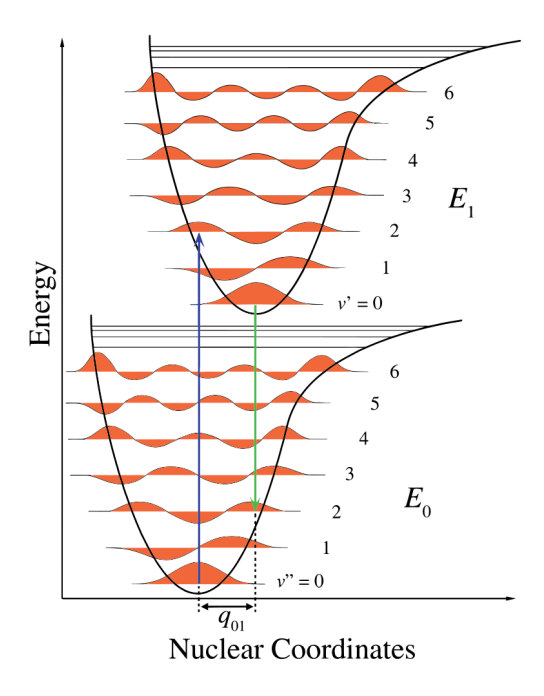


Figure 3: Transitions between the different electronic states [2]

Figure 3 illustrates the electronic transitions that occur on a timescale which is far shorter than nuclear motion. The most intense vibrational transitions are those in which the nuclei only experiences a minimal displacement.

1.3.5 Fluorescence lifetime and quantum yield

Quantum yield measures the efficiency of a photo-physical or photo-chemical process. It's defined as the ratio between the number of events (e.g. photons emitted or chemical reactions occurring) and the number of photons absorbed.

It's usually expressed as a dimensionless number between 0 and 1 (or a percentage). A quantum yield of 1 means that every absorbed photon results in the desired event.

Photobleaching

In optics, **photobleaching**, also referred to as *termed fading*, is a photochemical alteration of a dye or a fluorophore molecule such that it's permanently unable to fluoresce.

Theoretically, a fluorophore [12] can repeatedly undergo the fluorescence process indefinitely. This property is exploited to generate signal multiple times, allowing for very sensitive techniques. However, degradation might occur due to the fluorophore's structural instability during the excited lifetime. When hit by a high-intensity light source, the fluorophore can change its structure so that it's no longer able to fluoresce.

This use of the term *lifetime* is not to be confused with the *lifetime* measured by fluorescence lifetime imaging.

The quantum yield Φ_F is given by the following ratio:

$$\Phi_F = \frac{k_{\text{rad}}}{k_{\text{rad}} + k_{\text{IC}} + k_{\text{ISC}} + k_{\text{react}}}$$
(10)

where $k_{\rm rad}$ represents the intrinsic radiative rate constant; $k_{\rm IC}$ is the depopulation contribution given by the internal conversion process; $k_{\rm ISC}$ is the contribution of intersystem crossing and $k_{\rm react}$ accounts for the various types of quenching and photochemical reactions. The fluorescence quantum yield approaches the maximum efficiency of 1 when the sum of the rates of non-radiative decays is significantly bigger the sum of the rates of radiative decays ($k_{\rm rad} \gg k_{\rm rad}$). The **observed fluorescence lifetime** τ_F , which counts how long the fluorescence lasts in practice (in the first singlet excited state), is always **shorter than the radiative lifetime** $1/k_{\rm rad}$, which is the theoretical lifetime of a molecule only decayed by emitting light. This is a consequence of the fact that **non-radiative decay** is **competing with radiative decay**, thus shortening the overall observed fluorescence lifetime. The highest is the intensity of the

The rate of change of the excited state population, which takes into account all the radiative and non-radiative phenomena, is given by

$$\frac{d[S_1]}{dt} = (k_{\text{rad}} + k_{nr})[S_1] \tag{11}$$

The solution to this equation can be expressed as

fluorescence, the more molecules are in the excited state.

$$[S_1](t) = [S_1](0) \cdot e^{-t/\tau_F} \tag{12}$$

where $[S_1](0)$ is the excited state population at time zero and τ_F is the observed fluorescence lifetime.

$$\tau_F = \frac{1}{k_{\text{rad}} + \underbrace{k_{\text{IC}} + k_{\text{ISC}} + k_{\text{react}}}_{\text{non-radiative}}}$$
(13)

1.3.6 Factors affecting fluorescence

In most cases, the fluorescence quantum yield and lifetimes, as well as the fluorescence emission spectra remain almost unaffected when the excitation wavelength changes [4]. This means that the observed fluorescence properties are not very sensitive to which wavelength are employed to excite the molecule with. Ideally the spectra of the fluorescence excitation and the one of absorption would perfectly overlap. When this is not the case, it means that this discrepancy is caused by some **excitation wavelength dependent photoinduced reactions**. Let's analyze a few causes that affect fluorescence:

1. Quencing: The reduction in the fluorescence intensity caused by quencing is related to various mechanisms, such as excited state reactions, transfers of energy between energy levels, complex formation (e.g. number of lone pairs of ions), and collisional quenching. This last process is also defined dynamic quenching, as it involves the collision between a fluorescent molecule and a quencher (usually part of the solvent) in the excited state. This collision results in a energy transfer without radiation (reduced fluorescence). On the other side, static quenching occurs as a result of the formation of a non-fluorescent

complex without any molecular collision. When the concentration of the solution is too high, the probability of two fluorophores colliding increases significantly. This leads to self-quencing effects, where energy is transferred from one fluorophore to another one.

- 2. **Reabsorption**: The emitted light related to the fluorescence phenomenon can be absorbed again by the same substance before it can propagate out. This could also lead to an increase of the Stokes shift. The effect is very evident when the **excitation and emission spectra of a substance overlap significantly**. This means that a smaller Stokes shift results a greater reabsorption.
- 3. **Temperature**: According to some research [8], exceeding a certain temperature causes an increase in quenching. Temperature also affects the emission spectra, by moving the peak emission wavelength (Stokes shift), permanently degrades the fluorophores faster (photobleaching), and slows the diffusion rates of fluorophores by changing the viscosity of the solvent.
- 4. **Solvent**: As already mentioned in 1.3.3, the difference in polarity between solute and solvent can influence fluorescence. If both the solvent and the solute are polar, fluorescence is increased, while if the solute is non-polar, fluorescence is dramatically decreased. Redshift is directly proportional to the difference in polarity between solute and solvent (solvent relaxation).
- 5. **pH**: This is the main focus of this work of thesis. The color and brightness of fluorescence is heavily correlated on the pH of the surrounding environment [9]. The effect on the arrangement of electrons impacts how the molecule absorbs and emits light. The molecule can bond or dissociate an H^+ according to the changes in pH. In the case of the fluorophore used for this work of thesis, passing from a strongly acidic solution to a neutral/basic solution, Fluorescein passes from a predominance of the cationic species to a predominance of the dianionic species due to the ionization. For pH between 4.3 and 6.4 a monoanionic form is present.

The core idea is that the molecule's ability to fluoresce becomes greater as it becomes more ionized (protons are lost gaining negative charges).

The presence of OH^- donor groups, which are the main characteristic of more alkaline solutions, promotes ionization, and as a direct consequence increases fluorescence. This is because protons are pulled away from the molecule, leading to a more ionized state.

The higher the pH, the higher the quantum yield and the smaller the breath of the spectrum.

As it can be observed in the measurements that have been made for this work of thesis, a very alkaline or very acidic pH environment can destroy the molecule structure and heavily affect fluorescence.

1.4 Microfluidic circuits

To reliably transport and merge small volumes of liquid while preserving precise control over their interactions, a microfluidic circuit can be employed. By confining the fluids to micro-scale channels, **laminar flow dominates**, enabling deterministic mixing and precise dosage.

1.4.1 Reynolds number

The **Reynolds number** is the ratio of inertial forces to viscous forces within a fluid in which there's a relative internal movement due to different fluid velocities.

$$Re = \frac{uL}{\nu} = \frac{\rho uL}{\mu} \tag{14}$$

where

- ρ is the density of the fluid $[kg/m^3]$;
- u is the flow speed [m/s];
- L is the characteristic length [m];
- μ is the dynamic viscosity of the fluid $[N \cdot s/m^2]$;
- ν is the kinematic viscosity of the fluid $[m^2/s]$.

For a flow in a pipe or tube, the Reynolds number is

$$Re = \frac{uD_H}{\nu} = \frac{\rho uD_H}{\mu} = \frac{\rho QD_H}{\mu A} \tag{15}$$

where

- D_H is the hydraulic diameter of the pipe [m];
- Q is the volumetric flow rate $[m^3/s]$;
- A is the pipe's cross-sectional area;

1.4.2 Navier-Stokes Equations and Stokes Flow

In fluid dynamics, the Navier–Stokes equations are the fundamental mathematical description of how viscous fluids move: they relate the velocity field of the liquid to its pressure distribution, viscosity, and any external forces (gravity, electric fields, etc.).

Although they admit closed-form solutions only in very simple geometries, they remain the most powerful and widely used tool for predicting fluid behavior, like the laminar flow in a micro-channel.

In microfluidic applications the characteristic Reynolds number is typically far below one (more details in paragraph 1.4.1), which simplifies the equations (inertia terms can be neglected), but

the Navier–Stokes framework is still essential for accurately capturing the subtle balance between viscous drag and pressure gradients that governs how two tiny streams interact, mix, or remain separated.

Let's consider the density of a fluid

$$\boldsymbol{\rho} = \rho(x, y, z, t) \tag{16}$$

Then, we can define the velocity \boldsymbol{u} :

$$\mathbf{u} = u_x \hat{i} + u_y \hat{j} + u_z \hat{k} \tag{17}$$

Let's now consider a fluid particle moving of dx, dy, dz during a time dt. The velocity variation $d\mathbf{u}$ is

$$d\mathbf{u} = \frac{\partial \mathbf{u}}{\partial x}dx + \frac{\partial \mathbf{u}}{\partial y}dy + \frac{\partial \mathbf{u}}{\partial z}dz + \frac{\partial \mathbf{u}}{\partial t}dt$$
 (18)

Let's now consider a fluid particle p, we can define the **material derivative** Du/dt as

$$\left(\frac{d\mathbf{u}}{dt}\right)_{p} = \frac{\partial \mathbf{u}}{\partial t} + \frac{\partial \mathbf{u}}{\partial x}\frac{dx}{dt} + \frac{\partial \mathbf{u}}{\partial y}\frac{dy}{dt} + \frac{\partial \mathbf{u}}{\partial z}\frac{dz}{dt} \tag{19}$$

Recalling that we can write dx/dt as u_x , the **total acceleration of a particle** is then given by

$$\implies \boxed{\frac{D\boldsymbol{u}}{Dt} = \underbrace{\frac{\partial \boldsymbol{u}}{\partial t}}_{\text{local acceleration}} + \underbrace{u_x \frac{\partial \boldsymbol{u}}{\partial x} + u_y \frac{\partial \boldsymbol{u}}{\partial y} + u_z \frac{\partial \boldsymbol{u}}{\partial z}}_{\text{convective acceleration}}}$$
(20)

The acceleration in fluid mechanics accounts for the fact that the mass is moving. For example, when a fluid accelerates, the distribution of its mass and the forces acting on it will influence how it flows and behaves under different conditions.

- The **local acceleration** term is 0 in case of *steady flow* (the flow parameters, such as velocity, pressure, and density, remain constant at each point in the fluid). In a steady flow we can still have a change in velocity.
- The **convective acceleration** term expresses the change in velocity due to the spacial position.

Expanding the material derivative term we get

$$\frac{D\mathbf{u}}{Dt} = \frac{\partial \mathbf{u}}{\partial t} + \mathbf{u} \cdot \nabla \mathbf{u}
= \left(\frac{\partial u_x}{\partial t} + u_x \frac{\partial u_x}{\partial x} + u_y \frac{\partial u_y}{\partial y} + u_z \frac{\partial u_z}{\partial z}\right) \hat{i}
+ \left(\frac{\partial u_y}{\partial t} + u_x \frac{\partial u_y}{\partial x} + u_y \frac{\partial u_y}{\partial y} + u_z \frac{\partial u_y}{\partial z}\right) \hat{j}
+ \left(\frac{\partial u_z}{\partial t} + u_x \frac{\partial u_z}{\partial x} + u_y \frac{\partial u_z}{\partial y} + u_z \frac{\partial u_z}{\partial z}\right) \hat{k}$$
(21)

Let's start by evaluating the **Continuity Equation** (conservation of mass). To do so, we consider an elemental fluid volume. We want to find the mass balance in point O, which is the center of the dxdydz cube. To do so, we consider the Taylor series expansion about point O. In general, let's recall a generic Taylor expansion:

$$f(x) = f(a) + f'(a)(x - a) + \frac{f''(a)}{2!} + \cdots$$
 (22)

The density at the right phase, taking into account that higher order terms can be neglected:

$$\rho = \rho_O + \left(\frac{\partial \rho}{\partial x}\right)_O \frac{dx}{2} + \left(\frac{\partial^2 \rho}{\partial x^2}\right)_O \frac{1}{2!} \left(\frac{dx}{2}\right)^{2*0} \tag{23}$$

$$\implies \rho = \rho_O + \left(\frac{\partial \rho}{\partial x}\right)_O \frac{dx}{2} \qquad u_x = u_{x,0} + \left(\frac{\partial \rho}{\partial x}\right)_O \frac{dx}{2} \tag{24}$$

The density at the left phase is:

$$\rho = \rho_O - \left(\frac{\partial \rho}{\partial x}\right)_O \frac{dx}{2} \qquad u_x = u_{x,0} - \left(\frac{\partial \rho}{\partial x}\right)_O \frac{dx}{2} \tag{25}$$

Now we can evaluate the **mass flux** at the two interfaces:

• Left interface:

$$(\rho u_x dA)_L = \left[\rho_O - \left(\frac{\partial \rho}{\partial x}\right)_O \frac{dx}{2}\right] \cdot \left[u_{x,0} - \left(\frac{\partial u}{\partial x}\right)_O \frac{dx}{2}\right] dy dz \tag{26}$$

• Right interface:

$$(\rho u_x dA)_R = \left[\rho_O + \left(\frac{\partial \rho}{\partial x}\right)_O \frac{dx}{2}\right] \cdot \left[u_{x,0} + \left(\frac{\partial u}{\partial x}\right)_O \frac{dx}{2}\right] dy dz \tag{27}$$

Figure 4 shows an elemental volume of fluid. In order to evaluate the **net outflow** across the fluid volume, we have to evaluate the difference between the right and the left interface's mass flux:

$$(\rho u_x dA)_R - (\rho u_x dA)_L = \left[u_{x,0} \left(\frac{\partial \rho}{\partial x} \right)_O + \rho_O \left(\frac{\partial u_x}{\partial x} \right)_O \right] dx dy dz = \left[\frac{\partial (\rho u_x)}{\partial x} \right]_O dx dy dz \qquad (28)$$

Doing the same for each direction we get the **total net mass outflow**:

$$\left[\frac{\partial(\rho u_x)}{\partial x} + \frac{\partial(\rho u_y)}{\partial y} + \frac{\partial(\rho u_z)}{\partial z}\right] dx dy dz \tag{29}$$

The mass must be conserved, consequently the total net mass outflow must match the rate of change of mass inside the volume:

$$-\frac{\partial \rho}{\partial t} \underline{dx dy dz} = \left[\frac{\partial (\rho u_x)}{\partial x} + \frac{\partial (\rho u_y)}{\partial y} + \frac{\partial (\rho u_z)}{\partial z} \right] \underline{dx dy dz}$$
(30)

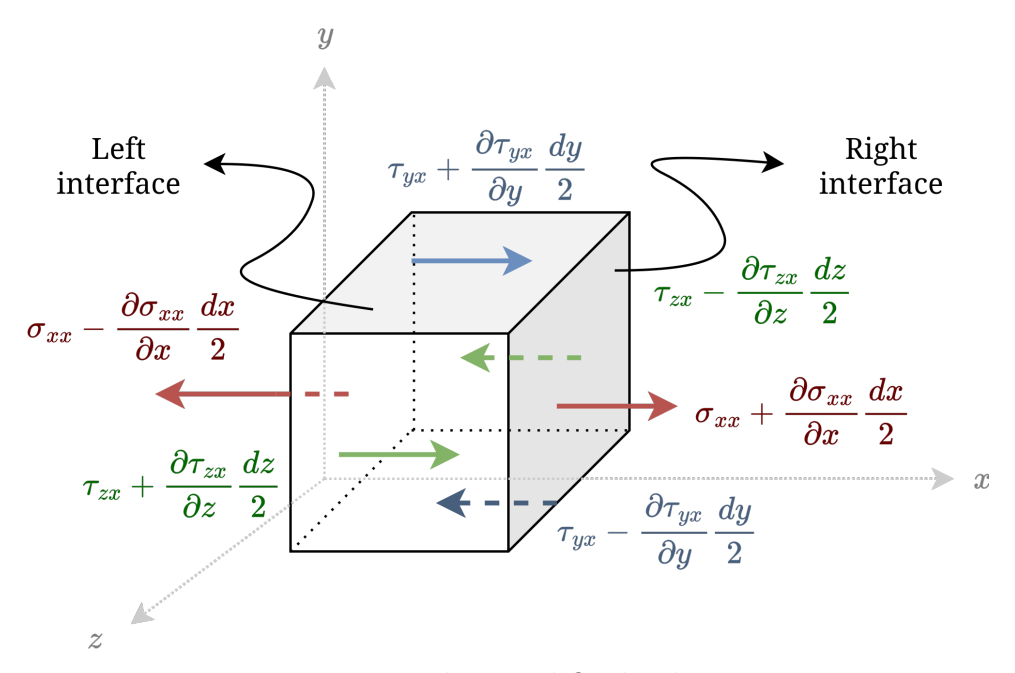


Figure 4: Elemental fluid volume

We've obtained the first of the two Navier-Stokes equations, in compact form:

$$\nabla \cdot \boldsymbol{u} = 0 \tag{31}$$

while in cartesian form we can write this as

$$\frac{\partial u_x}{\partial x} + \frac{\partial u_y}{\partial y} + \frac{\partial u_z}{\partial z} = 0 \tag{32}$$

Let's now focus on the **Conservation of momentum** equation, which resembles a *force bal-ance*. From Newton's second law, we know that

$$\mathbf{F} = m\mathbf{a} \tag{33}$$

We can then express the total force acting on the fluid cube element, per unit volume, as

$$\rho \frac{D\boldsymbol{u}}{Dt} = \cdots \tag{34}$$

The goal is now expanding this expression. We can begin by evaluating the **surface force**:

$$d_{f_{sx}} = \left(\sigma_{xx} - \frac{\partial \sigma_{xx}}{\partial x} \frac{dx}{2}\right) dydz - \left(\sigma_{xx} + \frac{\partial \sigma_{xx}}{\partial x} \frac{dx}{2}\right) dydz \tag{35}$$

$$+\left(\tau_{yx} + \frac{\partial \tau_{yx}}{\partial y} \frac{dy}{2}\right) dxdz - \left(\tau_{yx} - \frac{\partial \tau_{yx}}{\partial y} \frac{dy}{2}\right) dxdz \tag{36}$$

$$+\left(\tau_{zx} + \frac{\partial \tau_{zx}}{\partial z} \frac{dz}{2}\right) dxdy - \left(\tau_{zx} - \frac{\partial \tau_{zx}}{\partial z} \frac{dz}{2}\right) dxdy \tag{37}$$

We can greatly simplify this long expression:

$$d_{f_{sx}} = \left(\frac{\partial \sigma_{xx}}{\partial x} + \frac{\partial \tau_{yx}}{\partial y} + \frac{\partial \tau_{zx}}{\partial z}\right) dx dy dz \tag{38}$$

Now we can account for body forces, which usually comprises gravity (in this case the direction of the gravity pull g_x is along the x direction):

$$d_{f_x} = \underbrace{d_{f_{S_x}}}_{\text{surface forces}} + \underbrace{d_{f_{B_x}}}_{\text{body forces}} = \left(\rho g_x + \frac{\partial \sigma_{xx}}{\partial x} + \frac{\partial \tau_{yx}}{\partial y} + \frac{\partial \tau_{zx}}{\partial z}\right) dx dy dz$$
(39)

The differential momentum equation for the x direction is then:

$$\rho \frac{Du}{Dt} = \rho g_x + \frac{\partial \sigma_{xx}}{\partial x} + \frac{\partial \tau_{yx}}{\partial y} + \frac{\partial \tau_{zx}}{\partial z}$$

$$\tag{40}$$

The same can be done for y and z directions:

$$\rho \frac{Dv}{Dt} = \rho g_y + \frac{\partial \tau_{xy}}{\partial x} + \frac{\partial \sigma_{yy}}{\partial y} + \frac{\partial \tau_{zy}}{\partial z}$$
(41)

$$\rho \frac{Dw}{Dt} = \rho g_z + \frac{\partial \tau_{xz}}{\partial x} + \frac{\partial \tau_{yz}}{\partial y} + \frac{\partial \sigma_{zz}}{\partial z}$$
(42)

In fluid mechanics, shear stresses arise from velocity gradients (i.e., from the relative motion of adjacent fluid layers) whereas normal stresses result from the isotropic pressure acting perpendicular to a surface.

The precise steps to derive the following relation of **stress in terms of velocity** would be too long to mention in detail. However, the following can be derived:

$$\begin{cases}
\tau_{xy} = \tau_{yx} = \mu \left(\frac{\partial v}{\partial x} + \frac{\partial u}{\partial y} \right) \\
\tau_{yz} = \tau_{zy} = \mu \left(\frac{\partial w}{\partial y} + \frac{\partial v}{\partial z} \right) \\
\tau_{zx} = \tau_{xz} = \mu \left(\frac{\partial u}{\partial z} + \frac{\partial w}{\partial x} \right)
\end{cases}$$

$$\begin{cases}
\sigma_{xx} = -p - \frac{2}{3}\mu\nabla \cdot \mathbf{u} + 2\mu\frac{\partial u}{\partial x} \\
\sigma_{yy} = -p - \frac{2}{3}\mu\nabla \cdot \mathbf{u} + 2\mu\frac{\partial v}{\partial y} \\
\sigma_{zz} = -p - \frac{2}{3}\mu\nabla \cdot \mathbf{u} + 2\mu\frac{\partial w}{\partial z}
\end{cases}$$

$$(43)$$

By treating the fluid as **incompressible** and **Newtonian** (i.e., assuming a constant viscosity and a linear relation between shear stress and velocity gradient) we can greatly simplify the governing equations. Let's have a look at the equation for direction x:

$$\rho \frac{Du}{Dt} = \rho g_x - \frac{\partial p}{\partial x} + \mu \left(\frac{\partial^2 u}{\partial x^2} + \frac{\partial^2 u}{\partial y^2} + \frac{\partial^2 u}{\partial z^2} \right)$$
(44)

In compact form and for each direction x, y, z we obtain

$$\rho \frac{D\mathbf{u}}{Dt} = -\nabla \mathbf{p} + \mu \nabla^2 \mathbf{u} + \rho \mathbf{g}$$
(45)

which is the **momentum balance equation** (Navier-Stokes Equation). Now we can make the terms dimensionless, so that we obtain a set of equations in which all variables are scaled by characteristic length, velocity, and pressure, yielding a **dimensionless form** where the scale goes from 0 to 1.

$$\mathbf{u}' = \frac{u}{\mathbf{u}} \qquad p' = \frac{p}{\frac{\mu u}{L}} \qquad t' = \frac{t}{\frac{L}{u}} \qquad \nabla' = L\nabla \tag{46}$$

Pressure scaling at higher velocities

When inertial effects are significant, the pressure fluctuations caused by the fluid's motion (the dynamic pressure ρu^2) become the appropriate scale for nondimensionalizing the pressure field:

$$p' = \frac{p}{\rho u^2}$$

Let's neglect gravity:

$$\rho \frac{D\mathbf{u}}{Dt} = -\nabla \mathbf{p} + \mu \nabla^2 \mathbf{u} + \rho \mathbf{g}$$
 (47)

Expanding the terms and plugging in the dimensionless terms in 46, we get

$$\rho\left(\frac{\partial u}{\partial t} + \mathbf{u} \cdot \nabla \mathbf{u}\right) = \rho\left(\underbrace{\frac{u}{L/u}\frac{\partial \mathbf{u}'}{\partial t'}}_{t=t'(L/u)} + \underbrace{\frac{u^2}{L}\mathbf{u}' \cdot \nabla \mathbf{u}'}_{\nabla = \nabla'/L}\right) = \underbrace{-\frac{\mu u}{L^2}\nabla' p'}_{\nabla = \nabla'/L} + \underbrace{\frac{\mu u}{L^2}\nabla'^2 \mathbf{u}'}_{\nabla = \nabla'/L} \underbrace{\frac{\mu u}{u = u/u'}}_{u=u/u'}$$
(48)

Rearranging we finally get

$$\underbrace{\frac{\rho u L}{\mu}}_{\text{Reynolds number}} \underbrace{\left(\frac{\partial \mathbf{u}'}{\partial t} + \mathbf{u}' \cdot \nabla' \mathbf{u}'\right)}_{\text{Inertial terms}} = \underbrace{-\nabla' p}_{\text{Pressure term}} + \underbrace{\nabla'^2 \mathbf{u}'}_{\text{Viscous term}} \tag{49}$$

When the Reynolds number $Re \ll 1$, the inertial term in the Navier–Stokes equations becomes negligible compared with the viscous term, and the flow is governed by the **linearized Stokes equations**.

A **Stokes flow** therefore arises under any of the following three situations:

- 1. Small-scale devices: the characteristic length L is below roughly 10^{-3} m (1 mm).
- 2. Slow flows: the characteristic velocity u is below about 10^{-3} m/s (1 mm/s).
- 3. **High viscosity fluids**: the dynamic viscosity μ exceeds roughly 10^{-3} Pa · s (i.e., the fluid is at least as viscous as water).

In any one of these regimes, the Reynolds number falls well below unity and the flow can safely be treated as a **Stokes flow**:

$$\left[-\nabla' p + \nabla'^2 \mathbf{u}' = 0 \right] \tag{50}$$

with the Continuity Equation

$$\nabla' \cdot \mathbf{u}' = 0 \tag{51}$$

Characteristics of Stokes flow

- 1. Negligible inertia: Re $\ll 1$ so the convective term can be dropped from the Navier–Stokes equations.
- 2. **Time-reversibility**: a reversal of the forcing (i.e., wall) instantaneously reverses the velocity field.
- 3. **Linear**, **analytically solvable**: the governing equations reduce to the linear Stokes equations, which admit closed-form solutions for many canonical geometries.

1.4.3 Exact solution to microfluidic flow equations

Let's now analyze the case of a creeping flow through a high aspect-ratio rectangular channel, as shown in *Figure 5*.

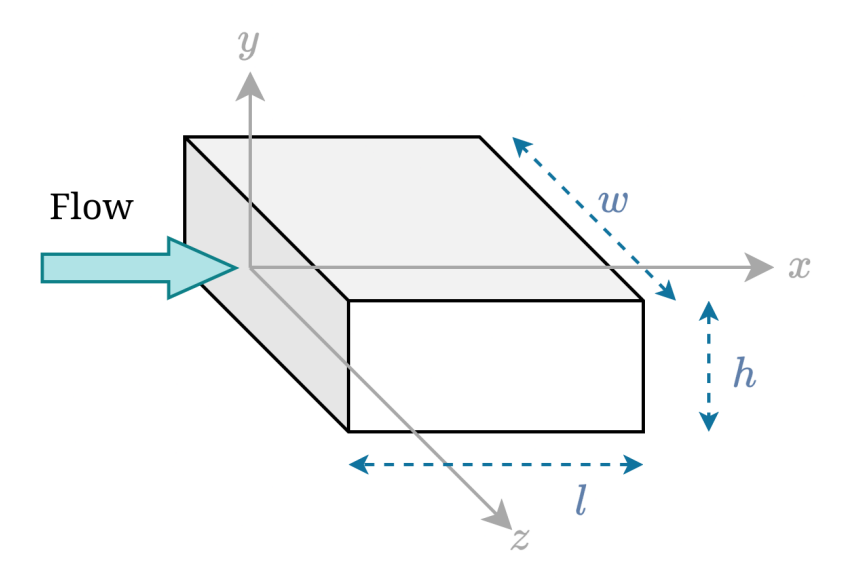


Figure 5: Flow in a block of dimension w, h, l along the x direction

Now we want to obtain actual flow description out of the equations obtained in the previous paragraph. Not the full equations, that have no closed-form solution, but the dimensionless ones with the simplification of low Reynolds number (equations 50 and 51). The flow is sustained by a pressure gradient in the x direction. The pressure drop is only in the x direction:

$$\frac{\partial p}{\partial y} = 0 \qquad \frac{\partial p}{\partial z} = 0 \tag{52}$$

As fluids cannot pass through walls, we can define the following **boundedness condition**:

$$u_y = 0 \qquad u_z = 0 \tag{53}$$

As we only have the velocity component along x left (u_x)

$$\frac{dp}{dx} = \mu \frac{\partial^2 u_x}{\partial x^2} + \mu \frac{\partial^2 u_x}{\partial y^2} + \mu \frac{\partial^2 u_x}{\partial z^2}$$
 (54)

and applying the continuity condition 51

$$\frac{\partial u_x}{\partial x} + \frac{\partial u_y}{\partial y} + \frac{\partial u_z}{\partial z} = 0 \implies \frac{\partial u_x}{\partial x} = 0 \implies \frac{\partial^2 u}{\partial x^2} = 0$$
 (55)

Combining 56 and 55 we get

$$\frac{dp}{dx} = \mu \frac{\partial^2 u_x}{\partial y^2} + \mu \frac{\partial^2 u_z}{\partial z^2} \tag{56}$$

Let's now assume this pressure gradient is linear and negative, as p is lower downstream $(-\Delta p/l)$. Now we can again use nondimensionalization:

$$y' = \frac{y}{h} \quad z' = \frac{z}{h} \quad u_x' = \frac{u_x}{u_c} \tag{57}$$

where u_c is the **characteristic speed** caused by the pressure drop which drives the flow. As we can clearly see, the z' term isn't a O(1), as the width is along the z direction (Figure 5) and due to the high aspect-ratio we have that $w \gg h$. By replacing the terms in 57 in $dp/dx = -\Delta p/l$ (56).

$$-\frac{\Delta p}{l} = \underbrace{\frac{\mu u_c}{h^2} \frac{\partial^2 u_x'}{\partial y'^2}}_{u_x = u_c u_x'} + \underbrace{\frac{\mu u_c}{h^2} \frac{\partial^2 u_x'}{\partial z'^2}}_{u_x = u_c u_x'} \implies -\frac{\Delta p \cdot h^2}{\mu u_c l} = \frac{\partial^2 u_x'}{\partial y'^2} + \frac{\partial^2 u_x'}{\partial z'^2}$$
(58)

Now we can re-scale the equation, by choosing $u_c = \frac{h^2 \Delta p}{ul}$:

$$-1 = \frac{\partial^2 u_x'}{\partial u^2} + \frac{\partial^2 u_x'}{\partial z^2} \tag{59}$$

Let's introduce another O(1) scaling factor $\hat{z}' = \epsilon z'$ where $\epsilon = h/w$.

$$z' = \frac{z}{h} \implies \hat{z}' = \frac{h}{w} \frac{z}{h} = \frac{z}{w} \tag{60}$$

The nondimensionalization of 59 becomes

$$-1 = \frac{\partial^2 u_x'}{\partial y^2} + \epsilon^2 \frac{\partial^2 u_x'}{\partial z^2}$$
 (61)

where the second term goes to zero beacuse we're dealing with a microfluidic channel with a high aspect ratio, which means $\epsilon = h/w \ll 1$, so $\epsilon^2 \ll 1$. We then obtain

$$-1 = \frac{\partial^2 u_x'}{\partial y'^2} \quad \text{as } \epsilon \to 0 \tag{62}$$

Up until now the main goal was to make this equation as simple as possible, to make finding a solution feasible. Now we can go back to the dimensional equations

$$\frac{dp}{dx} = \mu \frac{\partial^2 u_x}{\partial y^2} \tag{63}$$

and use the following terms for another nondimensionalization:

$$u'_{x} = \frac{u_{x}}{U} \qquad y' = \frac{y}{h} \qquad x' = \frac{x}{h} \qquad p' = \frac{p}{\mu U/h}$$

$$\tag{64}$$

where U is the average flow speed. Now we can apply these to 63:

$$\frac{\mu V}{h^2} \frac{dp'}{dx'} = \frac{\mu V}{h^2} \frac{\partial^2 u_x'}{\partial y'^2} \implies \underbrace{\frac{dp'}{dx'}}_{f(x')} = \underbrace{\frac{\partial^2 u_x'}{\partial y'^2}}_{f(y')}$$
(65)

It's now clear that this is only possible if

$$\frac{dp'}{dx'} = -K \tag{66}$$

which means that the dimensionless pressure gradient must be equal to a constant (K). Recalling that x is the flow direction and y is along the height of the channel, let's state the boundary conditions:

$$u_x'\left(\frac{1}{2}\right) = 0 \qquad \frac{\partial u_x'}{\partial y'}(0) = 0 \tag{67}$$

where 1/2 is the height at which the wall is present (no slip condition) and due to symmetry we have that the derivative in the middle of the channel (between the walls in the interval [-1/2; 1/2]) must be 0. Now we can solve the simplified equation we've previously stated:

$$\frac{dp'}{dx'} = \frac{\partial^2 u_x'}{\partial y'^2} = -K \implies \frac{\partial u_x'}{\partial y'} = -Ky' + c_1 \implies u_x'(y') = \frac{-Ky'^2}{2} + c_1y' + c_2 \tag{68}$$

By applying the boundary conditions, we can obtain c_1 and c_2 :

$$\begin{cases}
\frac{\partial u_x'}{\partial y'}(0) = 0 \implies \boxed{c_1 = 0} \\
\frac{u_x'}{\partial y'}(1/2) = 0 \implies \boxed{c_2 = K/8}
\end{cases}$$
(69)

The **velocity profile** is then

$$u_x'(y') = \frac{K}{8}(1 - 4y'^2)$$
(70)

The average flow speed U is

$$U = \frac{1}{A} \int u_x dA \implies U = \frac{1}{h} \int_{-h/2}^{h/2} u_x dy \tag{71}$$

where the area is given by A = wh. Now we can plug in the velocity profile obtained in 70 dimensionlessly:

$$1 = \int_{-1/2}^{1/2} u_x' dy' \implies 1 = \int_{-1/2}^{1/2} \left(\frac{1}{8}K - \frac{1}{2}Ky'^2\right) dy' \tag{72}$$

Doing the calculations we can evaluate K:

$$1 = \left(\frac{1}{8}Ky' - \frac{1}{6}Ky'^3\right)\Big|_{-1/2}^{1/2} \implies K = 12$$
 (73)

The **final equation** that we get is:

$$u_x'(y') = \frac{3}{2} \left[1 - (2y')^2 \right]$$
 (74)

This is clearly a f(y') that only depends on y'. Note that this is valid for all flows through micro-channels, as long as the hypotheses hold true (low Reynolds number and high aspect-ratio).

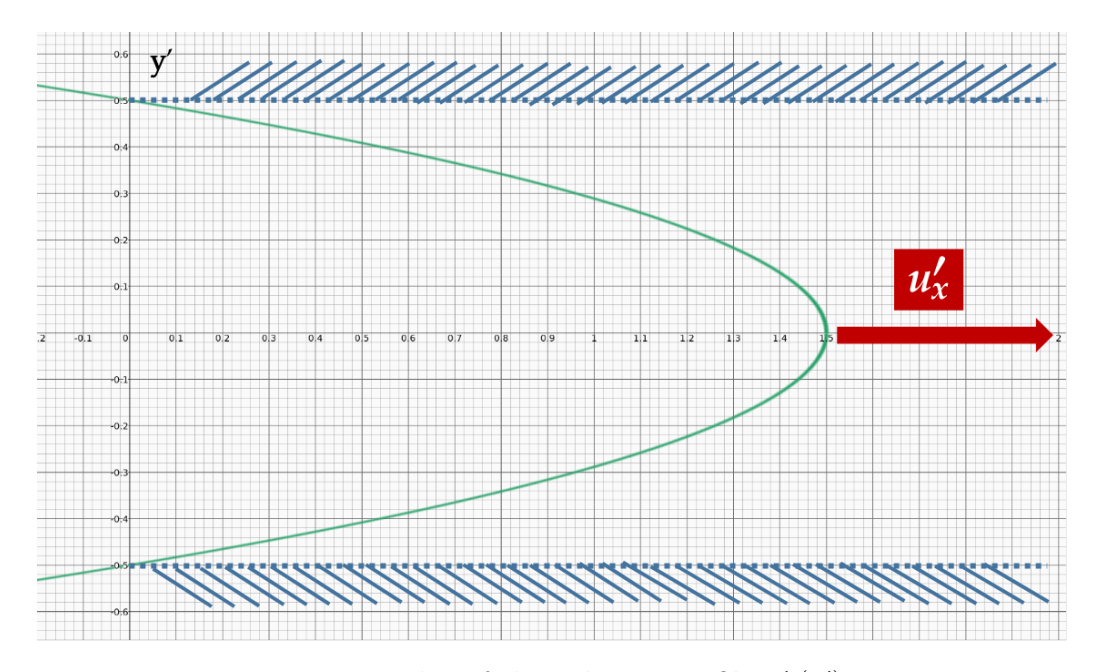


Figure 6: Plot of the velocity profile $u'_x(y')$

Let's analyze what happens when dp/dx changes:

$$\frac{dp}{dx} = \frac{\mu u}{h^2} \frac{dp'}{dx'} \tag{75}$$

When the pressure gradient changes, then the average velocity U changes. We can now easily evaluate the **maximum speed** and where it occurs by studying

$$\frac{du'_x}{dy'} = -12y' = 0 \implies y' = 0 \implies u_{x,\text{MAX}} = 1.5 \tag{76}$$

1.4.4 Navier Stokes Equations in Single Phase Microfluidics

First, let's make a few assumptions about the fluid we're dealing with:

- **Newtonian**: A fluid is *Newtonian* if the viscosity remains constant whatever the shear rate (rate at which a progressive shear strain is applied to some material). If ketchup was Newtonian, patting the bottle wouldn't help making the fluid flow.
- Incompressible
- Isothermal: We consider no loss or gain of heat.

The Second Newton Law states that:

$$m\mathbf{a} = \sum F \tag{77}$$

If we consider each individual point by dividing per unit of volume:

$$\rho \mathbf{a} = \sum F \implies \rho \frac{d\mathbf{u}}{dt} = \sum F \tag{78}$$

where ρ is the density of the fluid. The Navier-Stokes Equations are

$$\begin{cases} \nabla \cdot \mathbf{u} = 0 & \to \text{Conservation of mass} \\ \rho \frac{d\mathbf{u}}{dt} + \rho(\mathbf{u} \cdot \nabla)\mathbf{u} = -\nabla \mathbf{p} + \mu \nabla^2 \mathbf{u} + \mathbf{F} & \to \text{Conservation of momentum} \end{cases}$$
(79)

where $\mathbf{u} = u_x \hat{\mathbf{x}} + u_y \hat{\mathbf{y}} + u_z \hat{\mathbf{z}}$ is the velocity, $\nabla \mathbf{p}$ is the pressure gradient, $\mu \nabla^2 \mathbf{u}$ is the friction (due to viscosity μ) and \mathbf{F} takes into account all the external forces acting on the flowing fluid.

$$\mathbf{F} = F_{\text{gravity}} + F_{\text{surface tension}} + F_{\text{other contributions}} \tag{80}$$

As we're dealing with microfluidic circuits:

- Low Reynolds Number: The term $\rho(\mathbf{u} \cdot \nabla)\mathbf{u}$, that would be a tricky non-linear term, disappears as the viscous forces become much more significant than inertial forces. We know that this is a momentum term, as it contains the fluid density term ρ .
- Low Bond Number: The term F_{gravity} takes into account the gravity the fluid is subject to. The bond number is defined as:

$$Bo = \frac{\rho g L^2}{\sigma} \tag{81}$$

In microfluidic circuits gravitational forces are less significant due to the small dimension of them.

• Single phase flow: We're dealing with fluids in which we suppose there are no water bubbles or droplets, the term $F_{\text{surface tension}}$ can be neglected.

The Navier-Stokes Equation can be greatly simplified:

$$\rho \frac{d\mathbf{u}}{dt} + \underbrace{\rho(\mathbf{u} \nabla)\mathbf{u}}_{\text{Low Reynolds Number}} = -\nabla \mathbf{p} + \mu \nabla^2 \mathbf{u} + \underbrace{F_{\text{gravity}}}_{\text{Low Bond Number}} + \underbrace{F_{\text{surface tension}}}_{\text{Single phase flow}}$$
(82)

and thus we obtain

$$\rho \frac{d\mathbf{u}}{dt} = -\nabla \mathbf{p} + \mu \nabla^2 \mathbf{u}$$
(83)

At steady state, we simply have

$$\nabla \mathbf{p} = \mu \nabla^2 \mathbf{u} \tag{84}$$

1.4.5 Molecular Diffusion

Molecular diffusion evaluates how molecules flow inside a fluid. In particular molecules tend to flow to areas with lower concentration.

• First Law of Diffusion: This law describes the rate of flow from high to low concentration. The *diffusive flux* of the i-th species J_i is

$$J_i = -D\frac{dC_i}{dx} \left[\frac{\text{mol}}{\text{s}} \right] \tag{85}$$

where D is the **diffusion coefficient** (that can be estimated through the Stokes Einstein Relation) and C_i is the concentration of the i-th species (in [mol/L].

• Second Law of Diffusion: This law describes how diffusion causes the concentration field to change with time.

$$\frac{dC_i}{dt} = D\frac{d^2C_i}{dx^2} \left[\frac{\text{mol}}{\text{s}} \right] \tag{86}$$

The diffusion parameter D can be predicted with the **Stokes Einstein Relation**:

$$D = \frac{kT}{6\pi\mu R_p} \tag{87}$$

where k is the Boltzmann constant and R_p is the molecule radius. This means that smaller molecules diffuse faster than bigger ones.

In order to estimate the distance traveled by a diffused molecule after a time t, it's possible to use the following relation:

$$\overline{x} = \sqrt{2Dt} \tag{88}$$

1.4.6 Microfluidic mixing techniques

The efficiency of mixing in microfluidic devices is **significantly constrained by the laminar-flow regime**, which typically produces two adjacent, parallel streams that mix only through diffusion.

Mixing only happens by diffusion at low Reynolds Number.

Let's now analyze **passive mixing methods**:

- 1. Advective mixing with 3D Serpentine channels: these are passive devices that don't require any pulsatile drives (*Figure* 7). They're quite hard to manufacture.
 - 3D serpentines are much more effective than their 2D counterparts, but are far more difficult to fabricate.
 - The higher the flow rate (the higher the Reynolds Number Re), the higher the mixing rate
 - Thanks to the L-shaped turns, they allow to achieve mixing in a very short length of a few mm.

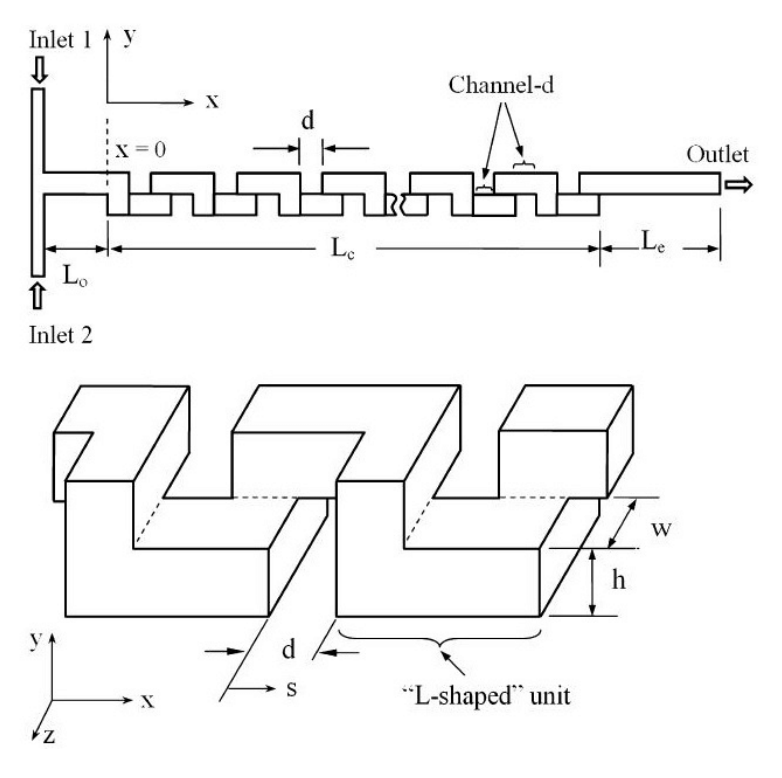


Figure 7: Advective Mixing with 3D Serpentine channels [11]

2. **Surface topology mixing**: one of the surfaces of the channel is carved in a suitable way to generate single of multiple vortexes that stir the two fluids together. To do so, a transverse stress component is introduced into an otherwise exclusively longitudinal laminar flow and this induces a **rotating motion**. This is a way easier method than the previous one.

Let's now analyze active mixing methods:

- 1. Active mixing using Acoustic Streaming: a piezoelectric transducer at 70 kHz/8V creates vibrations in the channel using a *micro-bubble*, which is a spot in the middle of the channel with a different acoustic impedance with respect to the surrounding fluid. This method has a very high performance, making it possible to obtain a nearly instant mixing [3]. When the bubble trapped in an *horse-shoe shaped* piezoelectric transducer vibrates back and forth inside a liquid, it induces rotational forces within the liquid.
- 2. Active Rotary Mixer using micro-valves: this method involves micro-valves and peristaltic pumps. Liquids are trapped in a rotary mixer and the peristaltic pumps are used to make them flow. Complete mixing requires a few seconds.
- 3. Vortex Mixer driven by micro-valves: this method mimics the process of manually pipetting in and out. This requires about 1 second.

1.4.7 Materials and production processes for microfluidic devices

Let's analyze a few materials that can be employed to fabricate microfluidic circuits and the pros and cons of each presented choice.

1.4.7.1 PDMS - Polydimethylsiloxane

Polydimethylsiloxane, or PDMS $(C_2H_6OSi)_n$ (Figure 8), is a widely used polymer in the field of fabrication of microfluidic chips. The fragmented formula is:

$$CH_3[Si(CH_3)_2O]_nSi(CH_3)_3$$

$$H_3C$$
 H_3C
 CH_3
 CH_3
 CH_3
 CH_3
 CH_3
 CH_3
 CH_3
 CH_3

Figure 8: PDMS molecule

Cross-link is a bond or a short sequence of bonds that links polymer chains to each other. They can be covalent bonds or ionic bonds.

The fabrication procedure of microfluidic devices consists in the mixing of liquid Polydimethyl-siloxane with a **cross-linking agent**, which is poured into a microstructured mold and heated to obtain a elastomeric replica of the mold. Even when mixed with the cross-linking agent, it remains liquid at room temperature for many hours. A very **high resolution** is possible, even reaching few nanometers.

Let's define the size of the monomers chain as n. When n is high, the material is almost in a liquid state; when n is low, the material is a semi-solid structure.

The organic functional group (Si-O-Si) results in a flexible polymer chain that has a high level of viscoelasticity (they're both viscous and elastic under deformation). This high viscosity doesn't facilitate the flow of liquids.

After cross-linking, PDMS becomes an **hydrophobic elastomer**. Wetting the PDMS with a polar solvent, such as water, isn't easy (water beads form and don't spread). This can lead to the absorption of hydrophobic contaminants from water on the material surface.

SiOH termination on the surface can be produced in order to change the surface chemistry and obtain a **temporarily hydrophilic material** and thus protecting it from the absorbtion of hydrophobic and negativiely-charged molecules.

Regardless of if the surface is plasma oxidized or not, it **doesn't allow water infiltration**. This makes it an excellent choice to avoid micro-structure deformation. It's also gas permeable. It's also relatively bio-compatible, inexpensive and deformable. It can **tightly bond to glass or other PDMS layers** with a plasma treatment.

Advantages of PDMS

- Low auto-fluorescence: The choice of PDMS for the purpose of fluorescence analysis is very good as it has a low autofluorescence and its transparency at optical frequencies facilitates the observation of the micro-channels using microscopes.
- **Tightly bonds to glass or other PDMS layers**: They can be achieved with a simple plasma treatment. This allows to overcome the limits of PDMS by exploiting the technological possibilities offered by glass surfaces (such as metal deposition, oxide deposition or surface functionalization).
- Multi-layers and micro-valves integration: Spin coating can be used to control thickness, allowing to fabricate multilayer devices and integrate micro-valves.
- Bio-compatibility

Limits of PDMS

The limits of this material are:

- Impossibility to perform metal and dielectric deposition: this makes it very difficult to embed electrodes and resistors. This can be overcome by using glass bonding.
- PDMS aging: the mechanical properties of the material can change after a few years.
- Permeable to water vapor: it doesn't handle evaporation well.

1.4.7.2 PDMS soft lithography

This technique can be considered as a complementary extension of photolithography, which is the main process used in the microelectronics industry. Let's have a quick overlook on the steps required for production (*Figure 9*):

- 1. A photoresist is deposited on the silicon wafer (Figure 9.a). A photoresist is a light-sensitive material that can be of two types:
 - **Positive photoresist**: In this case light weakens the resist and this results in a hole being created. As an example, a positive photoresist is a material whose solubility changes by the photogenerated acid.
 - **Negative photoresist**: In this case light toughens the resist and creates an etch resistant mask. In this case the photoresist becomes unsoluble when exposed to a suitable light source.
- 2. After UV light exposure, the mask is removed and the photoresist is either dissolved or toughened in correspondence to the empty spaces left by the mask, obtained a *master* (Figure 9.d).

3. Up until now the procedure is analogue to the standard photolithography one. Now PDMS is poured on the master and then peeled away. Now the microstructures have been embossed to the PDMS layer (*Figure 9.*f).

Why soft?

The term *soft* arises due to the fact that, unlike photolithography, soft lithography allows to deal with a wide range of elastomeric materials, which are mechanically soft materials.

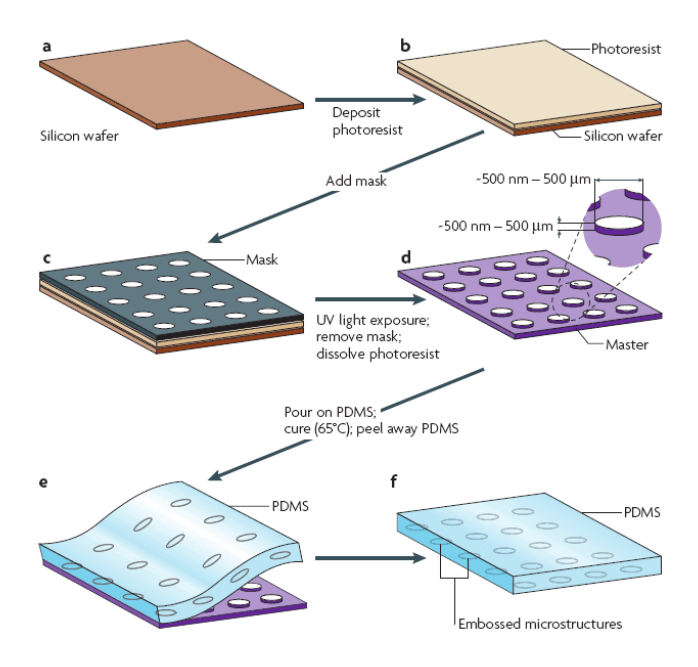


Figure 9: PDMS fabrication steps [6]

In microfluidics it's essential to be able to obtain a **sealed device**. In order to achieve such a requirement there are two main ways:

- Glass slide enclosure: The circuit is simply closed with a glass slide over the circuit.
- PDMS bonding between two PDMS layers: This involves the bonding of another PDMS layer.

This method is quite expensive. As bio-compatibility isn't required, a more cost-effective procedure and material would be preferred (such as PMMA).

1.4.7.3 PMMA - polymethyl-methacrylate

PMMA (which constitutive repeating unit is shown in *Figure 10*), which is also known as *acrylic glass*, allows to fabricate more cost-effective prototypes at a scale which is higher than the micro-metric one. Modern 3D printers can achieve reasonably fine resolution, allowing for the creation of relatively small channels.

Because the material has a refractive index of 1.49 at 589.3 nm and exhibits only **weak aut-ofluorescence**, it is compatible with fluorescence-based sensing without introducing excessive

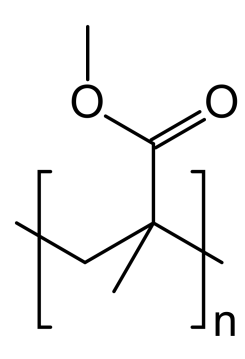


Figure 10: Poly(methyl methacrylate) or PMMA repeating unit

background noise signals. Additionally, PMMA can be sealed by thermal bonding, and it is chemically resistant to most aqueous reagents, making it a practical substrate for microfluidic devices.

PMMA is **somewhat transparent**, allowing for visual inspection of the flow.

1.4.7.4 PLA - Polylactic acid

The only promptly available material that could be employed to quickly test the designed microfluidic circuit during the thesis work was PLA, which is a great material for prototyping items that don't require high strength or heat resistance. It's a **type of bioplastic** derived from renewable resources like cornstarch or sugarcane.

Limits of PLA

- **Porosity**: PLA is slightly porous, which affects fluid flow (especially for very small volumes).
- Swelling: PLA can sometimes swell if exposed to certain solvents. This means that a certain amount of a liquid can be absorbed by it.
- Limited durability: PLA isn't as flexible or durable as PDMS, so it's not suited for repeated use.
- Channel size limitations: PLA's printing resolution may limit the smallest achievable channel size compared to PDMS.

2 Preliminary laboratory analysis

The initial phase of the study evaluated the feasibility and limitations of the pH-measurement method under investigation. Sodic Fluorescein (Uranine) was chosen as the tracking agent because its polar nature permits easy dissolution in aqueous media. In addition, Sodic Fluorescein has photophysical and chemical characteristics that make it ideally suited for pH-sensing:

- pH responsiveness: the fluorescence peak intensity shift monotonically across the pH range of interest for many applications such as hydroponics (pH 4-9). This predictable behavior allows to use it as a tracker for pH measurement. The fluorescence of this molecule is very intense; peak excitation occurs at 437 nm and peak emission at 515 nm [7].
- Low toxicity: this dye, which is commercially available in high purity form, should be treated as a special waste, but it's not correlated to significant levels of toxicity and thus not considered hazardous.
- Commercial availability and low cost: this dye is widely distributed and inexpensive. It can be obtained with consistent quality, simplifying experimental replication.

For the measurements the protonation-induced changes in the Sodic Fluorescein fluorophore's electronic structure is used to obtain a **measurable change in emitted light**.

In order to **cover other pH ranges**, alternative fluorophores can be introduced, as suggested by a previous thesis work on fluorescent dyes [5]. A good candidate is *Rhodamine B*, which remains chemically intact and retains its fluorescence quantum yield across the 12.5–14.25 pH interval. While the peak intensity diminishes as the solution becomes more alkaline, the emission maximum stays essentially fixed. When the experimentally measured pH values are plotted against the corresponding peak intensities, the relationship is almost perfectly linear, enabling a straightforward calibration curve. An even more robust option is *Rhodamine 6G*. Its fluorescence response is both rapid and stable over a wide pH range, and, like Rhodamine B, the emission wavelength does not shift appreciably with pH.

Because neither Rhodamine B nor Rhodamine 6G degrades in highly alkaline solutions, each dye yields a distinct, reproducible spectral fingerprint for every pH value, unlike Sodic Fluorescein, whose structure is compromised under the same conditions.

2.1 Initial analysis of the spectra obtained from the samples

In order to evaluate the efficacy of Fluorescein in pH tracking, the samples have been prepared by mixing 0.15 g of powder Fluorescein (Hanse Pro Uranina, 100 g) with 120 ml of water. The main idea is **correlating the fluorescence peak to the sample pH**.

Figure 11 represents the laboratory setup. The sample was inserted in a Thorlabs CVH100 cuvette holder, in which a Thorlabs M450LP2 450 nm mounted LED was added, along with the fiber cable for the spectrographic analysis.

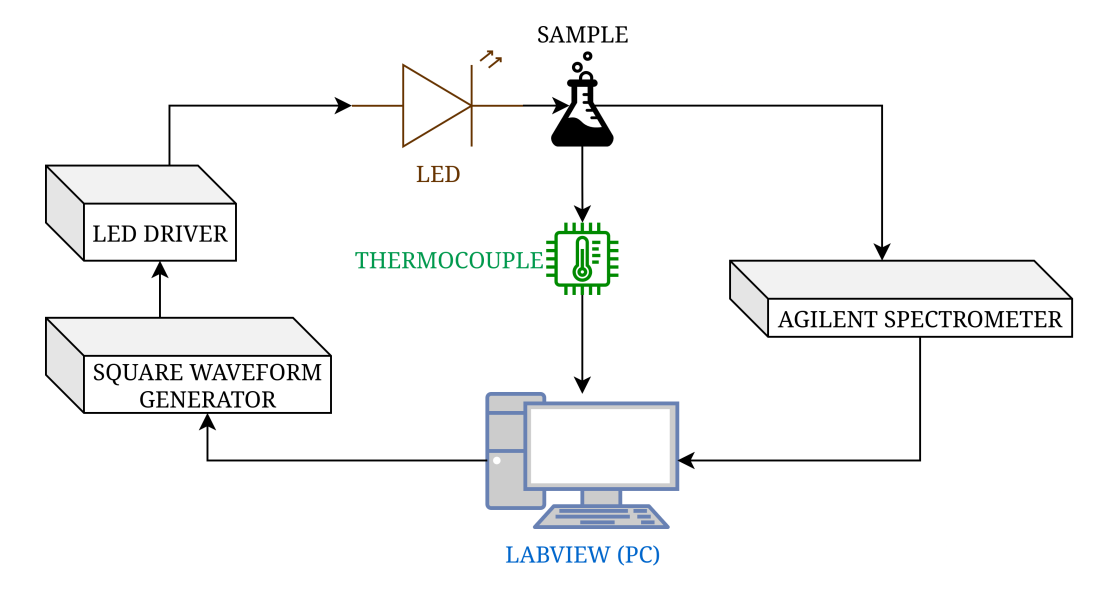


Figure 11: Laboratory setup

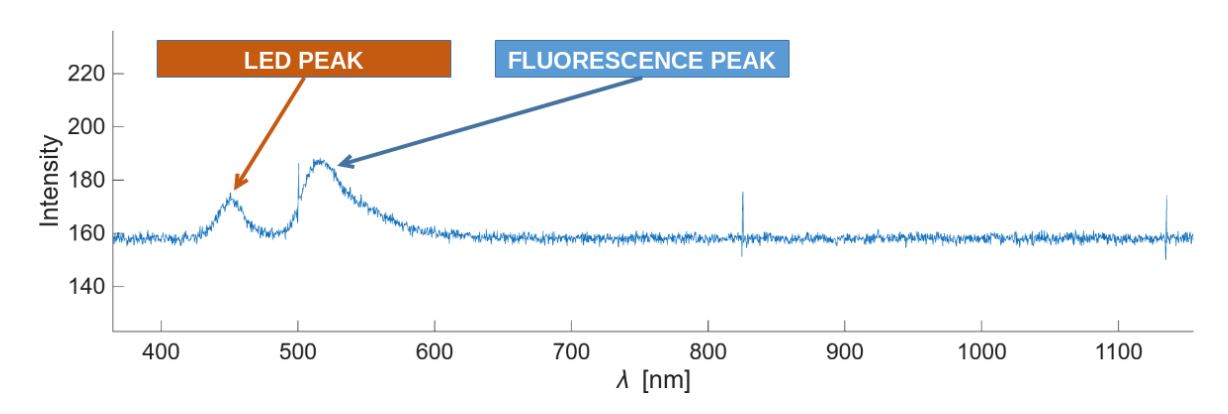


Figure 12: Example of a spectra obtained using the Agilent spectrometer

Figure 12 shows an example of spectra that was recorded by the spectrometer and then imported in Matlab to be analyzed.

At first, during the whole acquisition period the LED was left turned on. A significant decay of the peak intensity recorded by the spectrometer was observed (Figure 13), while the temperature of the liquid rose due to the LED continuous exposure. When the temperature was brought back to room temperature, the peak intensity didn't recover. This suggests that the observed phenomenon could be related to **photo-bleaching**, which is a permanent change in the structure of the fluorophore that disrupts its fluorescence. As this phenomenon constitutes a significant interference to the pH measurement, the LED switch on time was reduced from a 100% to a 5% duty cycle, which corresponded to a 3 seconds exposure every minute. In order to do so a National Instruments square waveform generator was connected to the LED driver and was driven by a LabVIEW script that also handled the acquisition of the samples. In order to eliminate the effect of the variations in the LED intensity, caused by the inconsistent action of the LED driver, the data was normalized over the measured LED peak.

To mitigate the influence of LED-output fluctuations, caused by the inconsistent behavior of the LED driver, the fluorescence data were normalized by the simultaneously recorded LED peak

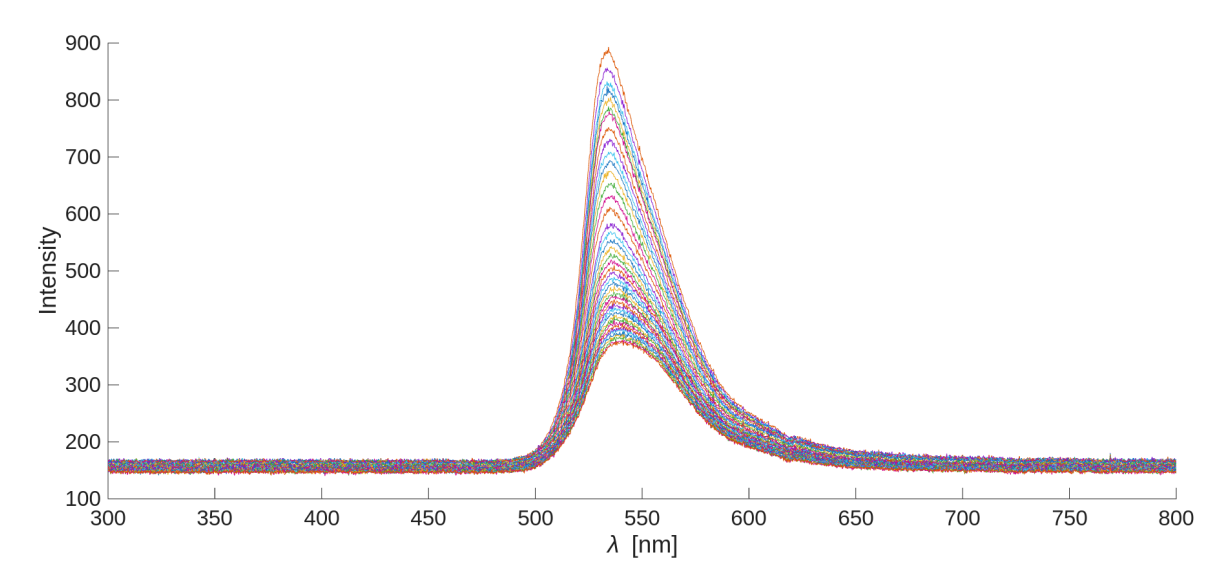


Figure 13: Superposition of the spectra captured by the laboratory spectrometer, with the sample exposed to an always on LED

intensity. This procedure removes common-mode variations in excitation power, allowing the remaining spectral features to reflect only changes in the sample's fluorescence rather than variations in the light source. In *Figure 14* we can see the effect of the always on LED on the fluorescence peak.

2.1.1 Influence of temperature to the fluorescence peak

To investigate the temperature dependence of the fluorescence peak, the aqueous sample was cooled to $21^{\circ}C$ while a reference measurement was taken at ambient room temperature ($30^{\circ}C$). Since photo-bleaching was effectively suppressed by limiting the sample's exposure to light, the remaining decrease in peak intensity can be attributed to temperature, displaying an inverse relationship. Figure 15 illustrates the fluorescence peak after normalization to the LED peak intensity.

The fluorescence-peak dependence on temperature is best described by a logarithmic fit, as shown in *Figure 16*. In order to obtain a pure number representing the time elapsed with respect to the start time, the timestamps have been converted to a serial format (purely numerical representation). The mathematical fit has been calculated using the *fitnlm* function for dealing with nonlinear regression models offered by a MATLAB plugin. The obtained function shown in *Figure 16* is:

$$y_{\text{fit}} = -a\log(x+c) + b \approx -0.2901\log(x+0.0342) + 0.4445$$
 (89)

2.1.2 Characterization of the relation between the fluorescence peak and pH

To investigate how the fluorescence peak intensity varies with pH, a series of samples with precisely defined pH values was prepared and their spectra recorded. The initial set of experiments included solutions at pH 6, 7, 8.5, 9, and 10. In *Figure 17*, the fluorescence peak, normalized to the LED peak intensity, is observed to increase with pH up to a value of 8.5. Beyond this

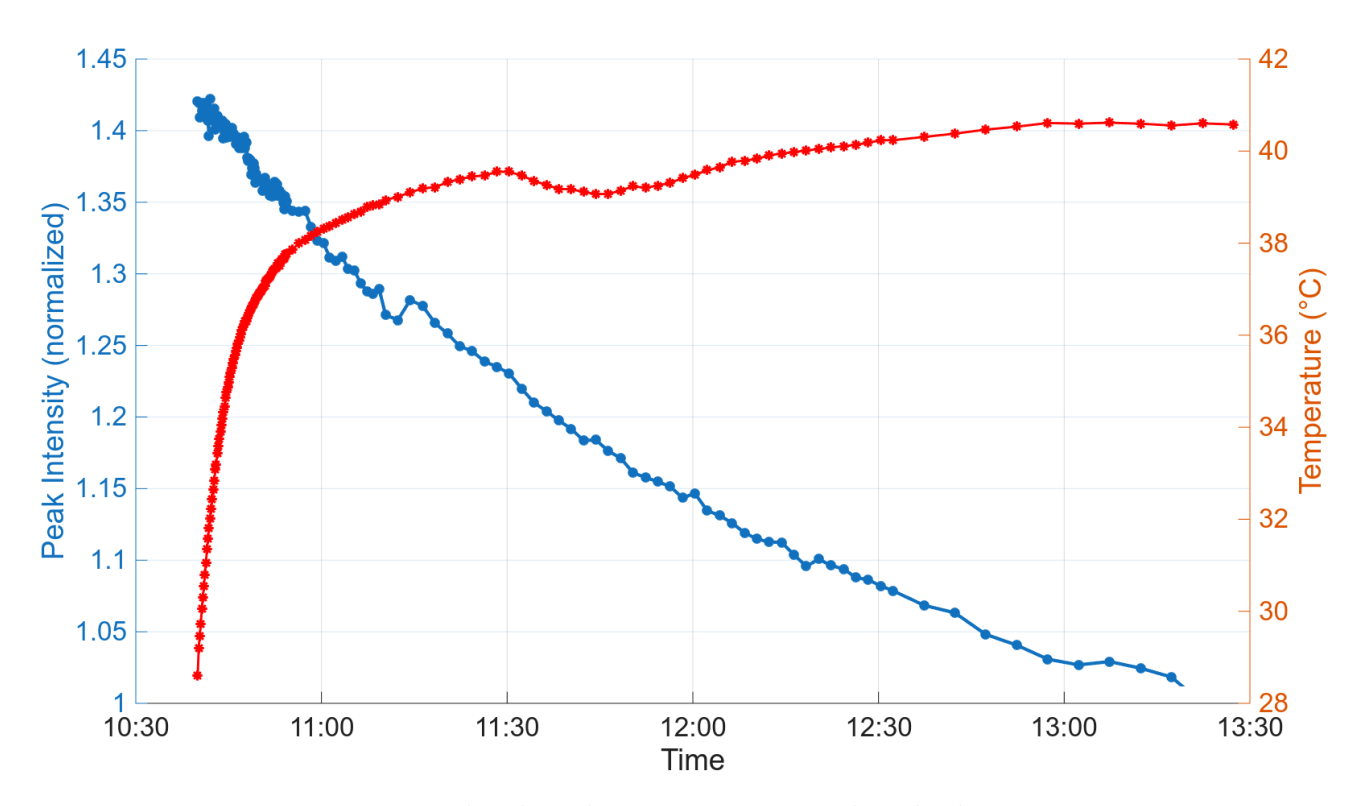


Figure 14: Normalized peak intensity captured with always on LED

threshold, the intensity begins to decline, and the fluorescence peak at pH 10 falls below that measured for the lower pH samples. No significant decrease of the fluorescence peak was observed over a 10-minute interval, indicating that photo-bleaching effects observed before can now be regarded as negligible.

In order to obtain the fluorescence peak, the findpeaks Matlab function was used, which locates the most prominent local maxima in a spectrum. A threshold on peak prominence allows to ignore all local maximums whose prominence is lower than the provided value. Prominence is the vertical distance between a peak and its nearest surrounding valleys, so that noise-related peaks are ignored.

Limitations of the initial analysis

- Limited repeatability: The volume of the tracer solution is several orders of magnitude smaller than that of the sample, which makes accurate dosing of the two components difficult and reduces reproducibility.
- Suppression of fluorescence in basic solutions: For pH > 8.5 the fluorescence peak intensity no longer increases monotonically with pH, indicating a pronounced loss of signal in more alkaline media and that now it's no longer possible to uniquely fingerprint a pH value.

Errors in the dosing of the tracer solution were identified as the primary potential cause of the initial lack of repeatability.

Multiple repetitions of the same experiment resulted into inconsistent outcomes: the pH at

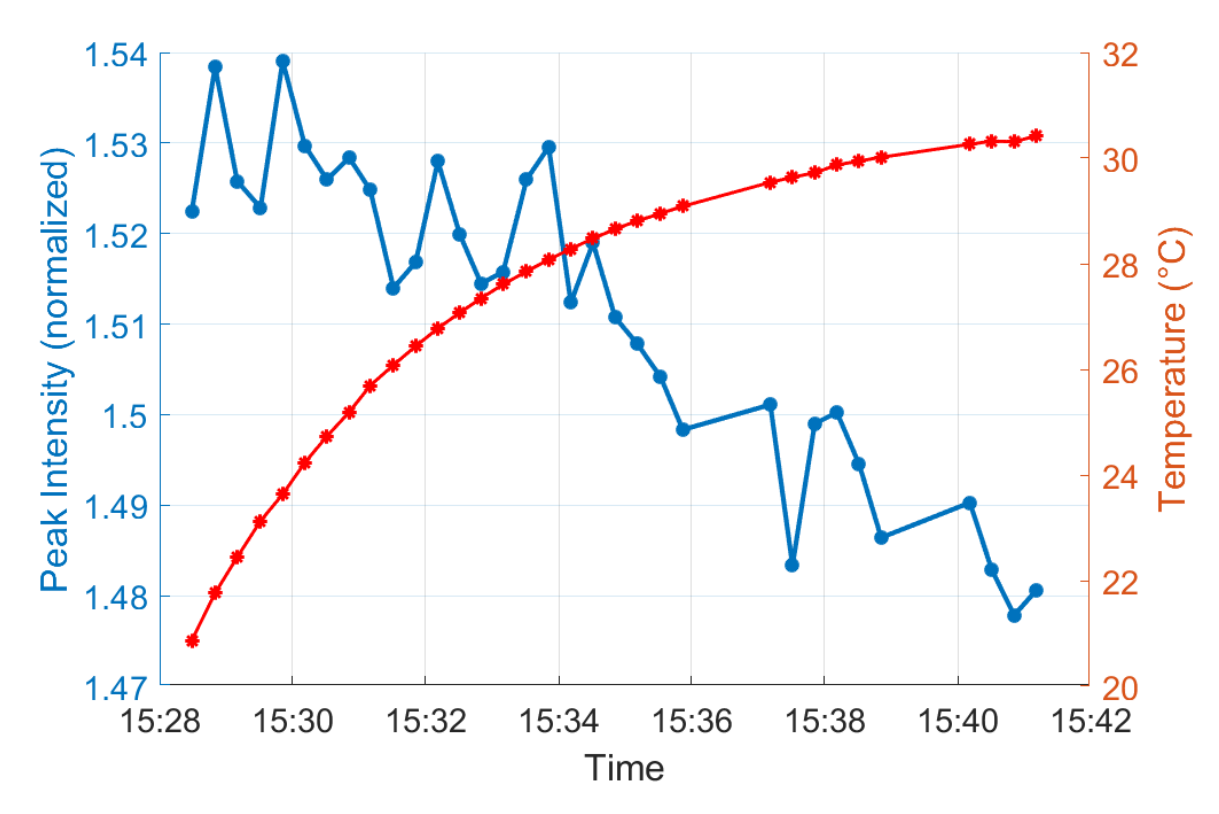


Figure 15: Colder water analysis: effect of temperature on the peak intensity

which the fluorescence peak began to decline varied, and the absolute peak-intensity values recorded for identical pH settings differed markedly, as shown in *Figure 18*.

Table 1: Composition of the tracer mixture

Ingredient	Mass (g)	Relative weight (%)
Fluorescein (Uranine)	0.15	0.12
Water	125.0	99.88
Total	140.0	100.00

The data presented in *Table 1* suggest that the concentration of the tracer solution is 1.2 g/L and thus **very distant from the NIH-reported solubility limit** of 40 g/L [10]. Exceeding this limit could constitute a significant source of error. To further mitigate this risk, the tracer solution was mixed thoroughly before being combined with the tracked solution. The tracer solution is prepared with distilled water to minimize noise.

2.1.3 Preparation of the buffer samples

pH is defined as the negative logarithm of the H^+ ion concentration:

$$pH = -\log_{10}[H^+] \tag{90}$$

Hence

$$[H^+] = 10^{-pH} (91)$$

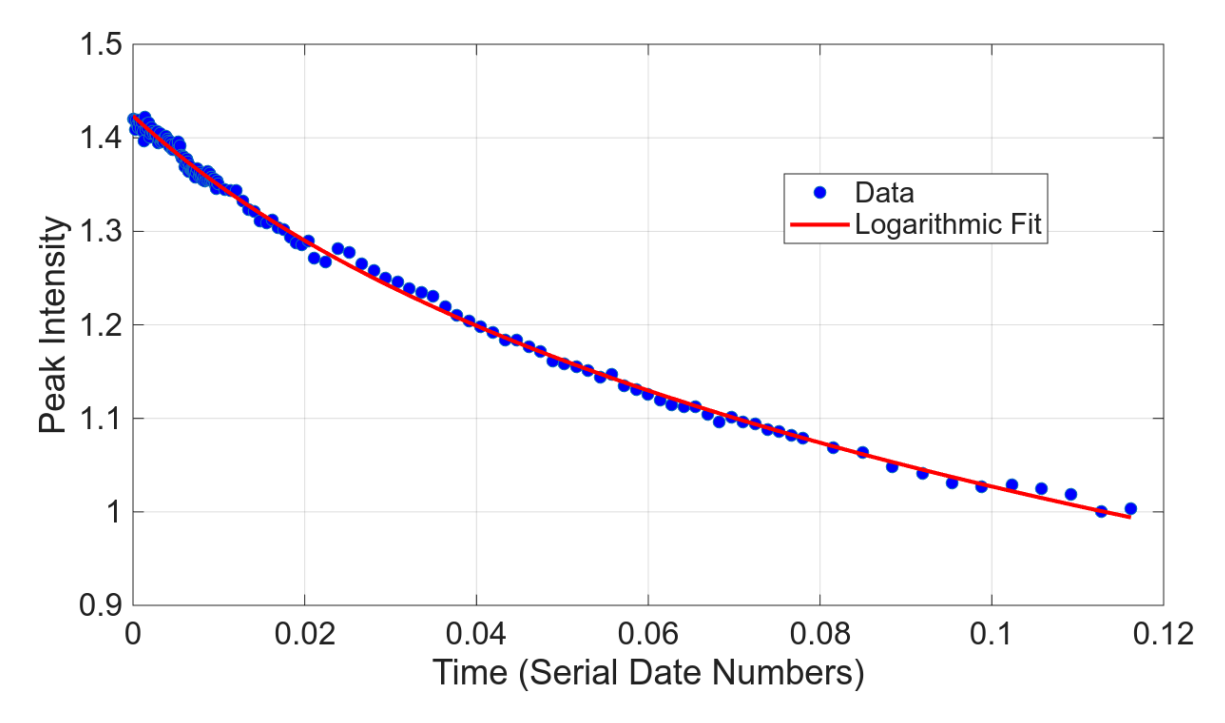


Figure 16: Logarithmic fit of the peak intensity decay over temperature

The pH scale is then logarithmic. Let's consider the pH range from 4 to 7 and let's define $x = 10^{-pH_t}$ as the target $[H^+]$ concentration at the target pH. At the edges of the interval we have

$$x_{\text{low}} = 10^{-7}$$
 (92)

which corresponds to the lower bound of the window and

$$x_{\text{high}} = 10^{-4}$$
 (93)

which corresponds to the upper bound of the window. We can then evaluate the total width of the window in $[H^+]$ units:

$$x_{\text{high}} - x_{\text{low}} = 10^{-4} - 10^{-7} \tag{94}$$

The distance in H^+ units from the target to the lower bound is:

$$x - x_{\text{low}} = 10^{-\text{pH}_t} - 10^{-7} \tag{95}$$

Now we have all the ingredients to evaluate the fraction of the concentration interval in the given pH range:

$$f_{4\to7} = \frac{x - x_{\text{low}}}{x_{\text{high}} - x_{\text{low}}} \tag{96}$$

To obtain 16 mL of test solution at any desired pH from the three reference bottles (pH 4, 7 and 10), only two of the references are needed. For targets between pH 5 and pH 7 the mixture contains pH 4 and pH 7; for targets between pH 7.5 and pH 9 it contains pH 7 and pH 10 (the pure pH 7 solution is used unchanged for pH 7). Let f be the fraction of the 16 mL that comes from the lower-pH bottle. It is obtained from the hydrogen-ion concentrations:

$$f_{4\to7} = \frac{10^{-\mathrm{pH_t}} - 10^{-7}}{10^{-4} - 10^{-7}}, \qquad f_{7\to10} = \frac{10^{-\mathrm{pH_t}} - 10^{-10}}{10^{-7} - 10^{-10}}$$
(97)

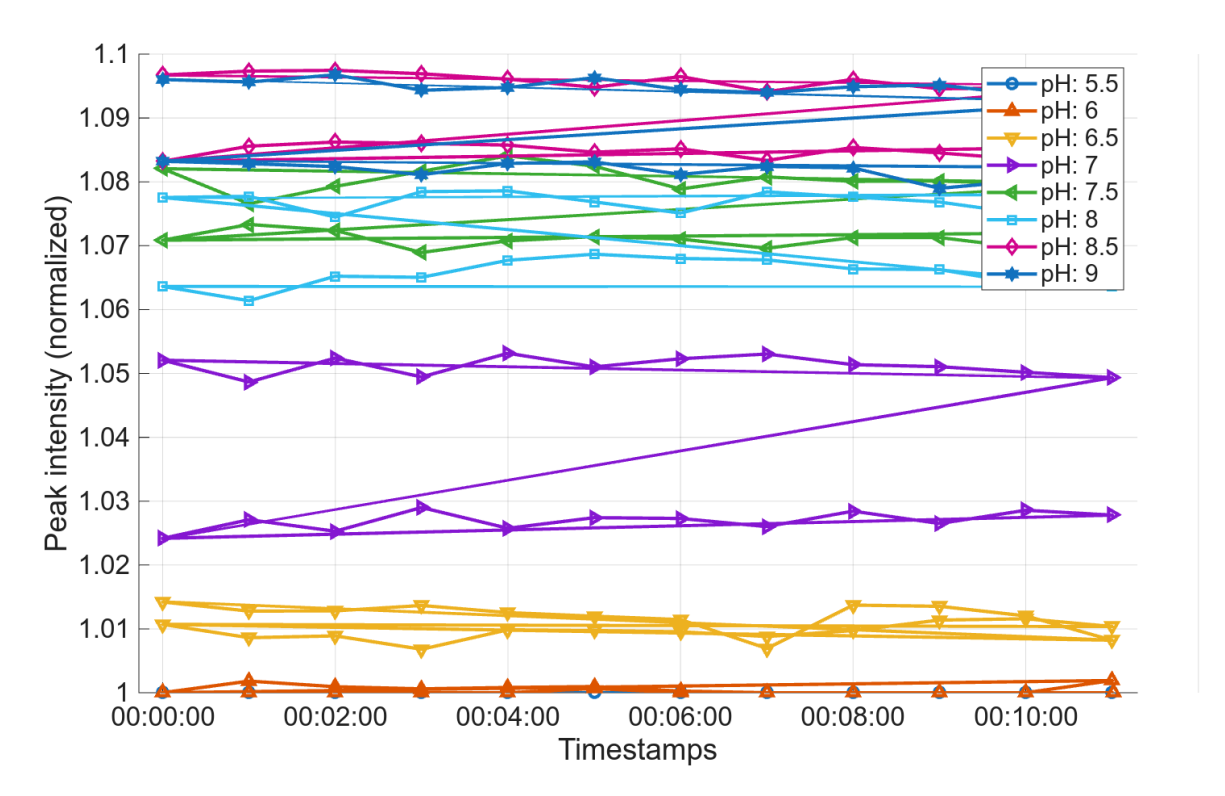


Figure 17: Intensity peaks captured by the spectrometer for every tested pH value

By multiplying the appropriate fraction by 16 mL the volume from the lower-pH bottle can be evaluated. It can then be subtracted that from 16 mL to get the volume from the higher-pH bottle. The two volumes have been then pipetted in a 20 mL vial. The resulting mix was then verified with a pH-meter with a minimum error of ± 0.1 pH (it's realistically greater due to probable errors during the manual calibration procedure). Figure 19 shows some of the pH buffers that were prepared and checked with a commercial pH pen device. As calibration, mixing and human errors are difficult to estimate, only a minimum error can be provided, which is the one provided by the datasheet of the pH pen (± 0.1 pH) [1].

Table 2: Volumes (mL) for 16 mL target solutions

Target pH	pH4 (mL)	pH7 (mL)	pH10 (mL)
5.0	1.4400	14.5600	0.0000
5.5	0.4904	15.5096	0.0000
6.0	0.1440	15.8560	0.0000
6.5	0.0344	15.9656	0.0000
7.0	0.0000	16.0000	0.0000
7.5	0.0000	5.0496	10.9504
8.0	0.0000	1.5856	14.4144
8.5	0.0000	0.4904	15.5096
9.0	0.0000	0.1440	15.8560

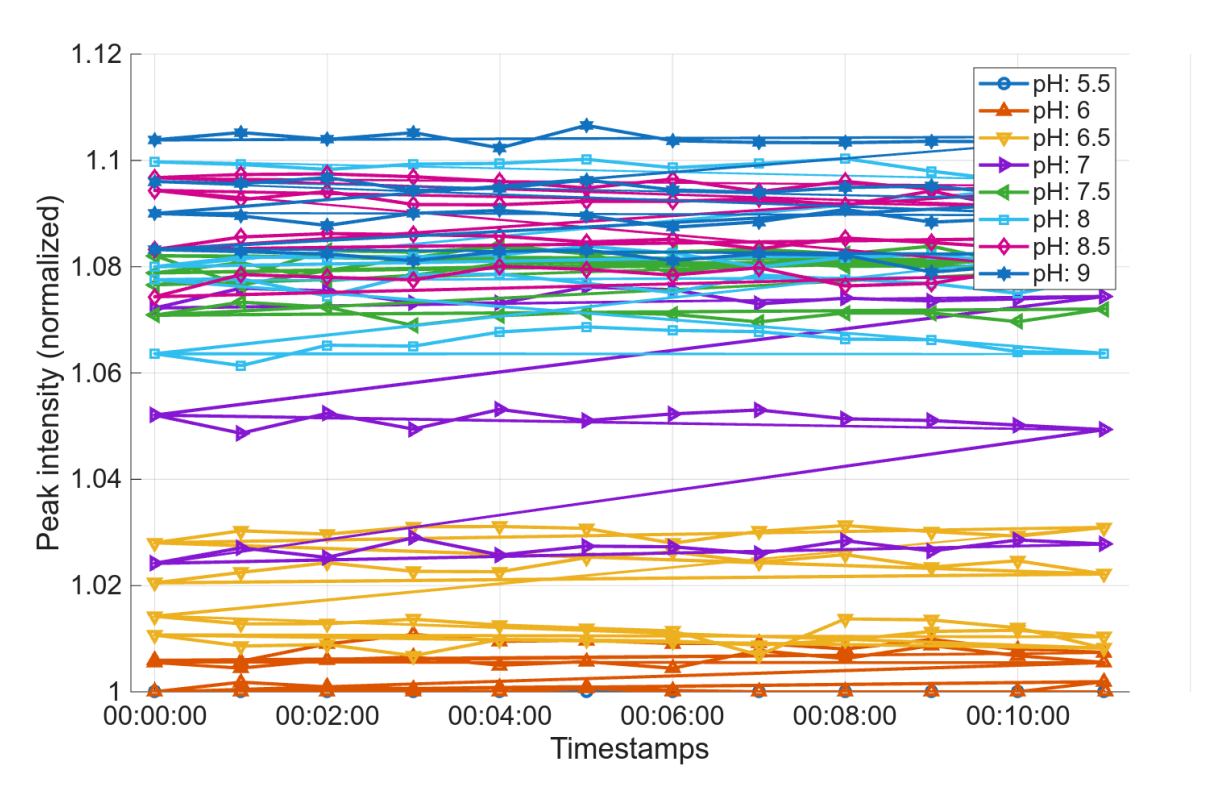


Figure 18: Comparison of intensity peaks captured by the spectrometer on multiple tests for each pH value



Figure 19: Some of the pH buffers prepared for data acquisition

2.2 Simulation of a 8-channel mini-spectrometer

The main goal of this thesis is to determine whether a practical, low-cost pH sensing device can be realized by exploiting fluorescence without the need for continuous recalibration. Relying on a broadband spectrometer that captures the full emission spectrum would result in a cost that amounts to several hundred euros per unit, rendering a compact, commercially viable device prohibitively expensive. To break this cost barrier, the project investigates the feasibility of a dedicated 8-channel mini-spectrometer. By simulating the optical response of this inexpensive device (by simulating in MATLAB its spectral sensitivity) the goal is **evaluating whether the reduced spectral information is still sufficient for accurate pH determination**. In order to find a marker which effectively captures a **unique fingerprint** correlated to a single value of liquid pH, the data obtained by the spectrometer have been sampled at given wavelengths.

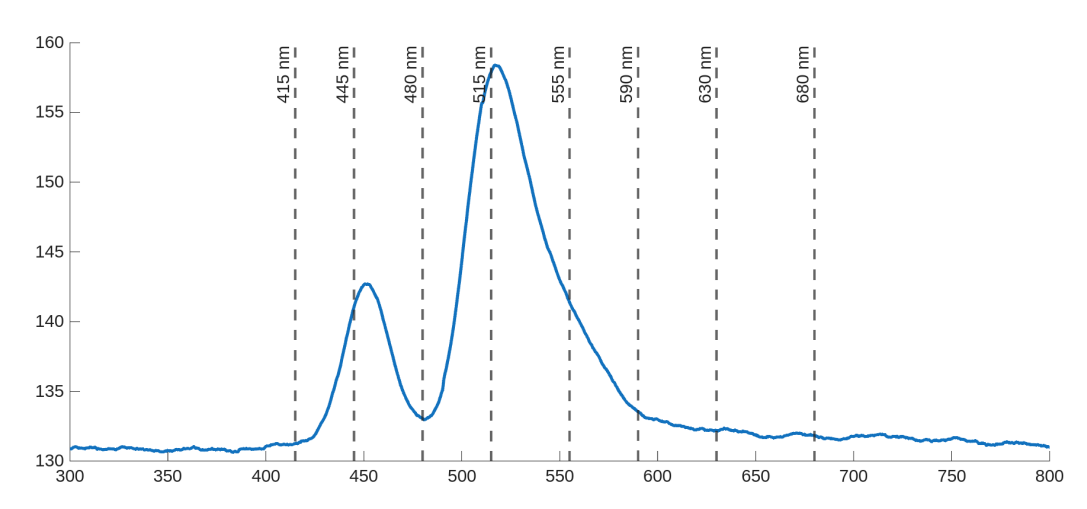


Figure 20: Example of spectra sampling to simulate a 8-channel mini-spectrometer (AS7431)

The AMS AS7341 is a 11-channel multi-spectral sensor for spectral analysis applications. 8 of the 11 optical channels cover the visible spectrum (which is the range of interest for fluorescence applications like the ones discussed in this work of thesis). The spectral response ranges approximately from 350 nm to 1000 nm. A NIR channel can complement the visible light data to provide information about the ambient light conditions. A dedicated GPIO line allows to syncronize the device to external signals. Data is provided through a I2C interface. The device has an ultra-low profile package with dimensions of 3.1mm x 2mm x 1mm.

LED as a noise source

Because the laboratory LED's intensity was difficult to keep stable, the recorded spectra were normalized to the LED's peak intensity. This normalization was intended to **decouple the spectra from instantaneous variations** in the LED's output.

Another source of noise that should be considered is the possibility of light leakage in the dark room that houses the sample and the spectrometer probe.

To determine whether a far cheaper n-channel mini-spectrometer can be used without compromising data quality beyond the threshold at which the fluorescence peak/pH correlation fails, we evaluated its performance by sampling the lab spectrometer data according to the

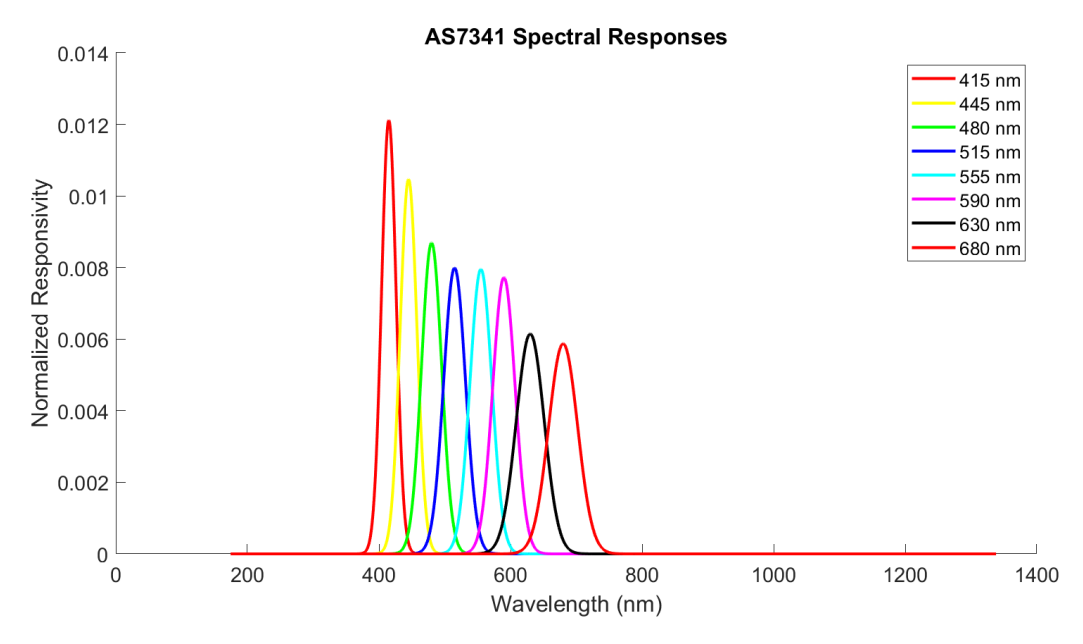


Figure 21: 8-channel AMS AS7341 datasheet spectral responses

datasheet of a commercial spectrometer ($AMS\ AS7341$). The weighted spectral responses over the 8 channels are shown in Figure 21.

The spectra recorded with the Agilent spectrometer were sampled at the central wavelengths of the eight channels, weighted by their relative sensitivities (see Figure 21). Because the spectral resolution is too coarse to resolve the peak intensity accurately, scatter plots were used to investigate whether a reproducible pattern could be reliably associated with the different pH clusters. The aim was to develop a scalable classification framework that could be refined to reach the desired precision; however, preserving the requisite data quality inevitably escalates device costs, potentially undermining its economic competitiveness relative to commercially available alternatives.

The two channels selected for analysis are 515 nm and 555 nm, because these are the only channels that exhibit significant overlap with the fluorescence peak (as clearly visible in *Figure 20*).

In Figure 22 the mean response recorded by Channel 4 (centered at 515 nm) rises monotonically with pH up until pH 8.5, whereas the signal from Channel 5 (centered at 555 nm) does not exhibit a clear monotonic trend.

Across multiple acquisitions performed on different days, recognizable but overlapping clusters emerge in the recorded data (*Figure 23*). This observation suggests that, by reducing the experimental errors that currently catastrophically limit repeatability, the resulting datasets could be grouped into well-defined clusters suitable for classification with algorithms such as support-vector machines (SVM). To do that, the cluster shouldn't overlap.

When clustering the data obtained from a single cycle of measurement at each pH, the overlap between the clusters is markedly reduced (*Figure 24*). However, the intrinsic lack of repeatability observed across different captures within the same measurement cycle remains, merely significantly diminished rather than completely eliminated.

Figure 25 shows the clustering areas found by applying the fitcecoc function in MATLAB. The plot makes it evident that the measurement resolution is constrained by the spacing of the

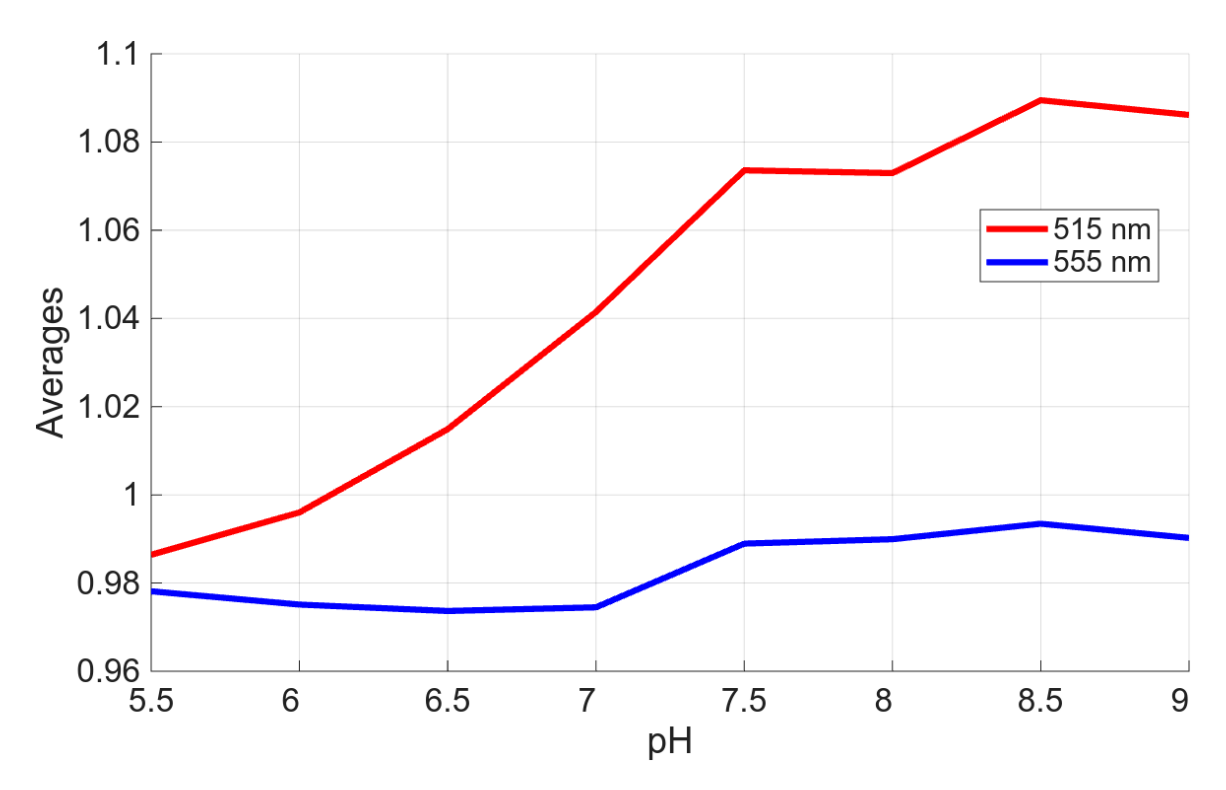


Figure 22: Intensity peaks for the two selected channels (Channel 4 at 515 nm and Channel 5 at 555 nm, normalized over Channel 2 at 445 nm) on multiple captures

training labels: the classifier can only discriminate between pH values that are separated by the Δ pH between the calibration buffers. Consequently, any finer gradation of pH would be unattainable without incorporating additional intermediate-pH training samples.

2.3 LED drift problem

A major source of uncertainty that becomes increasingly relevant when the resolution of the measurement is raised (i.e., when the classifier must distinguish a larger number of pH levels) is **LED drift**. The central wavelength of a monochromatic LED is not perfectly stable; it oscillates around its nominal value. This introduces a systematic error in the normalization step that relies on the LED peak intensity, thereby perturbing the measured fluorescence peak and compromising the consistency of the classification.

In Figure 26, a pronounced overlap is evident even when the pH values are spaced by 0.5 units; a typical 10 nm wavelength drift around 450 nm introduces sufficient variation to compromise the separation of classification zones, thereby increasing the likelihood of misclassification. The bars indicate the variation that arises from a simulated acquisition in which the normalization constant (the LED-peak intensity) is offset by ± 10 units.

Figure 27 displays the spectral transmission of a commercial Thorlabs **pass-band filter** (model FBH05450-40: centered at 450 nm, T > 90%, FWHM = 40 nm, outer diameter = 12.5 mm) overlaid with two drifted LED spectra (± 10 nm). The integrated LED intensity that reaches the photodiode when filtered by the ideal (centered) spectrum equals 33.9794; for the spectrum shifted to the right the filtered intensity is 30.2159, and for the left-shifted spectrum it is 31.1470. These values demonstrate that the pass-band filtering yields a normalization constant

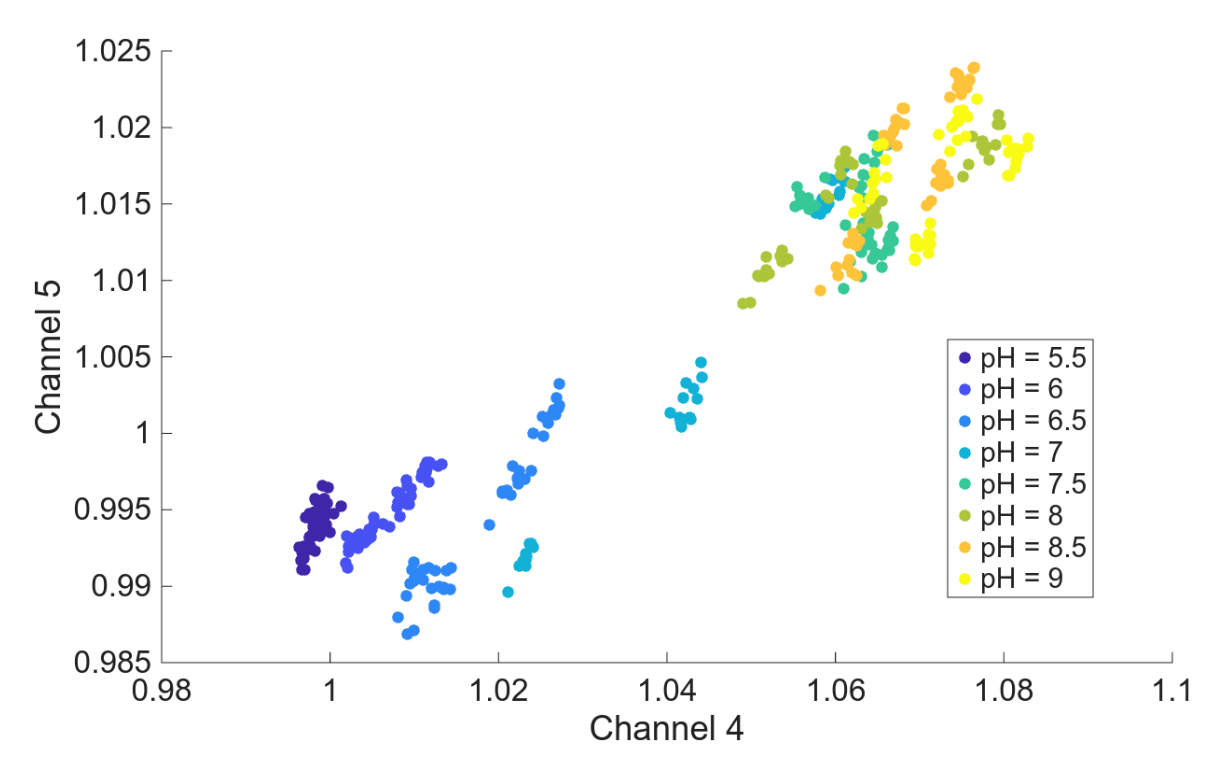


Figure 23: Superposition of scatter plot of two channels (Channel 4 at 515 nm and Channel 5 at 555 nm, normalized over Channel 2 at 445 nm) on multiple captures

that varies only by a few percent, thereby providing a sufficiently stable reference for the fluorescence-peak normalization.

To mitigate this issue, the normalization constant can be determined without sacrificing information on the LED's overall intensity. By employing a **band-pass filter**, the integrated LED intensity is recorded by an extra photodiode (*Figure 28*) over a specified spectral window rather than at a single wavelength, allowing the normalization factor to **accommodate** natural spectral drift while preserving a robust measure of the LED's power.

Another option is given by laser diodes, which exhibit a well-characterized, temperature dependent spectral drift, which can be quantified and compensated for by incorporating a temperature sensor and corresponding software correction.

2.4 Improvement to the tracer solution formula

The principal source of error in the first round of fluorescence analyses was the **extremely** tight tolerance on the ratio of tracer liquid to tracked liquid that we had initially selected. Mixing $2\mu L$ of tracer liquid with 3 mL of tracked liquid produced a large error in the fluorescence peak, even though the error in the sample preparation itself was comparatively small.

Let's assume a conservative estimation of the human error in the preparation of the samples: $\pm 0.1 \ \mu\text{L}$. Then, the relative error on the fluorescence peak, which is directly correlated to the Fluorescein concentration (whose fluctuations are considered as noise), can be evaluated starting from the nominal mass of Fluorescein present in the test sample (0.24 mg). The uncertainty in

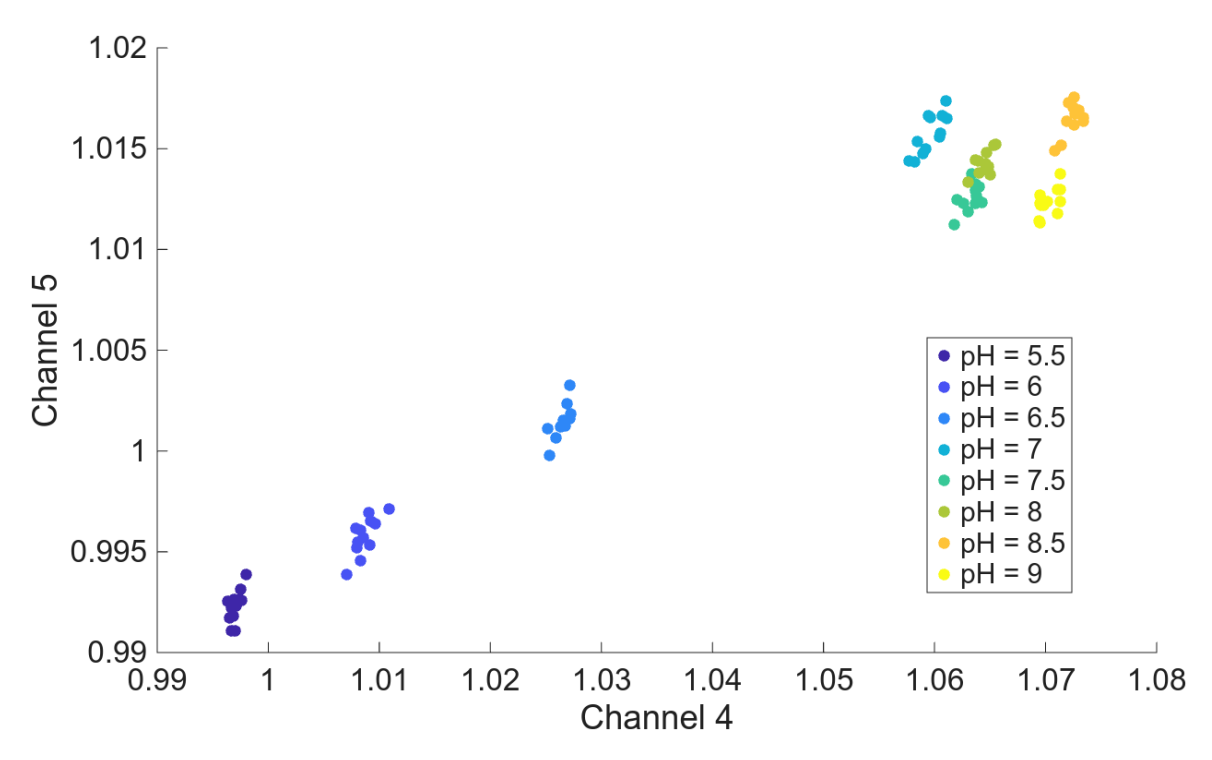


Figure 24: Scatter plot of two channels (Channel 4 at 515 nm and Channel 5 at 555 nm, normalized over Channel 2 at 445 nm) on one single cycle of measurements

the mass due to $\pm 0.1 \mu L$ error is given by

$$\Delta m = 0.12 \frac{\text{mg}}{\mu \text{L}} \cdot 0.1 \mu \text{L} = 0.012 \text{ mg}$$
 (98)

The relative percent error in the mass is then

$$\frac{\Delta m}{m_{nom}} \cdot 100\% = \frac{0.012}{0.24} \cdot 100\% = 5\% \tag{99}$$

If the error jumps to 0.2 μ L, the error doubles and reaches 10%. Increasing the tracer solution aliquot helps decreasing the relative uncertainty in mass.

In the first round of tests, 0.15 g of Fluorescein were mixed with 125 mL of water. The resulting tracer solution had a concentration of 1.2 g/L. The test samples were prepared with 3 mL of liquid to test and 2 μ L of tracer liquid. The final quantity of Fluorescein that was present in a test sample, was

$$1.2 \cdot 10^{-3} \frac{g}{mL} \cdot 0.002 \text{ mL} = 2.4 \cdot 10^{-6} \text{ g} = 2.4 \cdot 10^{-3} \text{ mg}$$
 (100)

Then, the concentration of Fluorescein in a test sample with 3 mL of liquid to analyze is

$$\frac{2.4 \cdot 10^{-3} \text{ mg}}{3 \text{ mL}} = 0.8 \frac{\text{mg}}{\text{L}}$$
 (101)

The primary objective of the second round of tests was to find a formulation that substantially relaxes the tolerances associated with sample preparation. To enhance the fluorescence peak at lower pH values, the Fluorescein present in each sample was doubled to

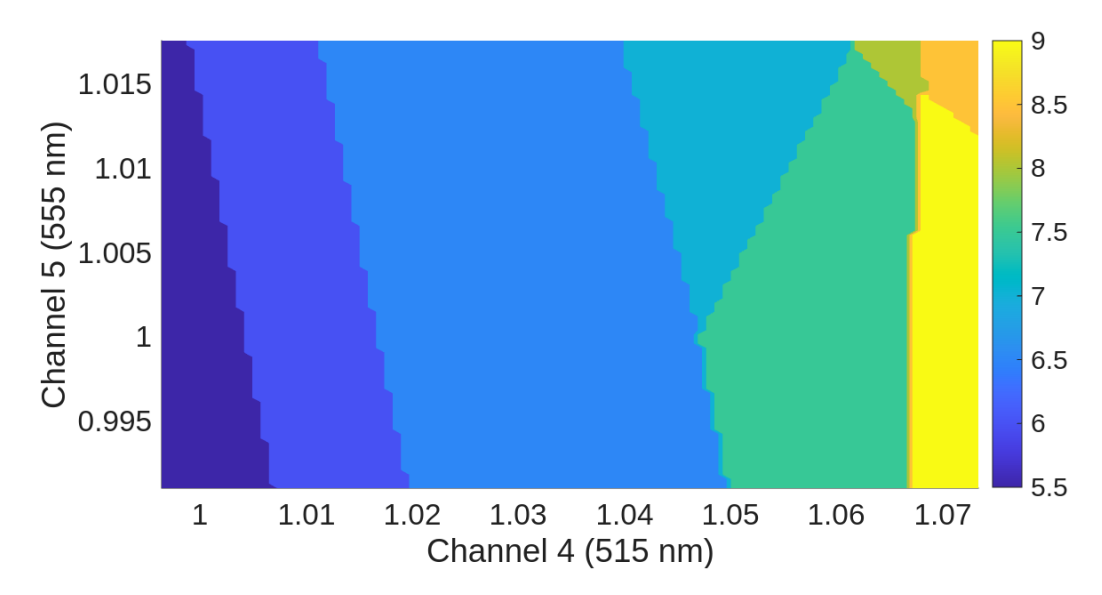


Figure 25: pH clusters obtained using SVM (fitcecoc) function in MATLAB run on Channel 4 (515 nm) and Channel 5 (555 nm)

 $4.8 \cdot 10^{-3}$ mg. Because the final goal is employing a microfluidic circuit for passive mixing, the volumes of the tracked and tracer liquids must be comparable in order to maximize the mixing efficiency. Higher volumes of tracked and tracer liquid increase the tolerance to preparation errors. The maximum water capacity of the test chamber was 4.3 mL; therefore we used 2 mL of tracked liquid and 2 mL of tracer liquid, which almost saturates the chamber while keeping the two volumes comparable.

In order to evaluate the required concentration of Fluorescein in the tracer solution to prepare, the following simple calculation was performed:

$$x \cdot 2 \text{ mL} = 4.8 \cdot 10^{-3} \text{ mg} \implies x = 2.4 \cdot 10^{-3} \frac{\text{mg}}{\text{mL}} = 2.4 \cdot 10^{-3} \frac{\text{g}}{\text{L}} = 2.4 \cdot 10^{-6} \frac{\text{g}}{\text{mL}}$$
 (102)

in which $4.8 \cdot 10^{-3}$ mg was the desired final quantity of Fluorescein in the test sample and 2 mL is the quantity of tracer liquid in the test sample.

As the precision of the balance that was available in the lab was 0.01 g, the tracer solution has been prepared by starting from a solution with a greater Fluorescein concentration, that has been then diluted to reach the final one. To prepare the solution, 0.12 g of Fluorescein have been mixed in 500 mL of water. The starting concentration was then

$$\frac{0.12 \text{ g}}{500 \text{ mL}} = 2.4 \cdot 10^{-4} \text{ g/mL}$$
 (103)

In order to prepare 500 mL of tracer solution with the target concentration of $1.2 \cdot 10^{-6}$ g/mL, 1.25 mL have been extracted from the 500 mL of starting solution previously prepared and mixed with 125 mL of water. The dilution factor has been found using the following calculation:

$$\frac{2.4 \cdot 10^{-6} \text{ g/mL}}{2.4 \cdot 10^{-4} \text{ g/mL}} = 1/100$$
 (104)

This 1:100 dilution allowed to obtain a final tracer liquid containing $1.2 \cdot 10^{-4}$ g of Fluorescein. The final concentration is then

$$1.25 \text{ mL} \cdot 2.4 \cdot 10^{-4} \frac{\text{g}}{\text{mL}} = 3 \cdot 10^{-4} \text{ g}$$
 (105)

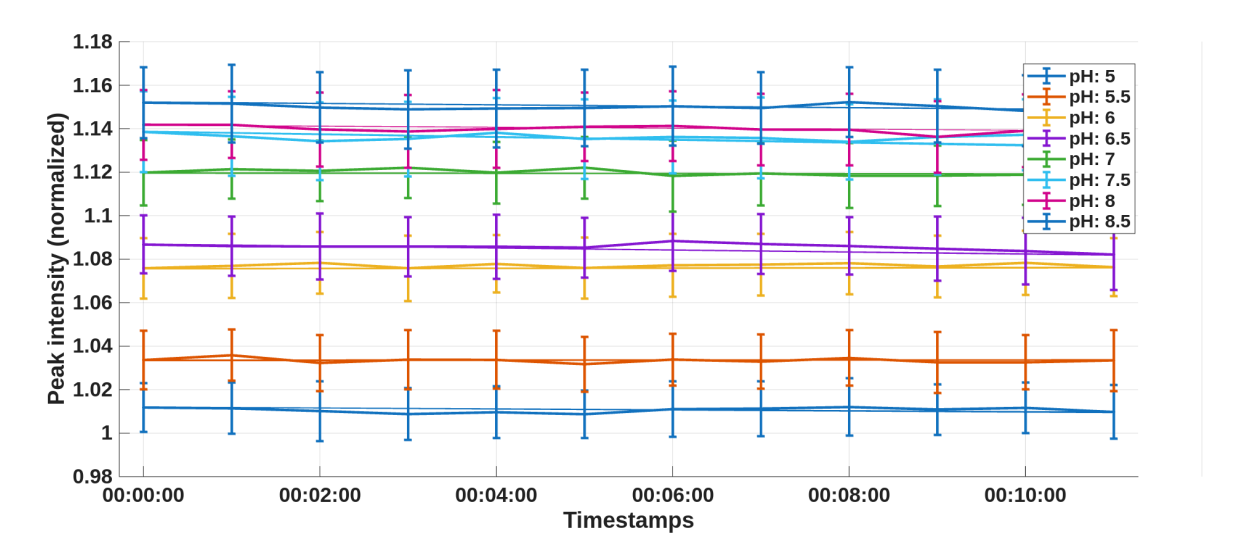


Figure 26: Simulated LED drift effect on the normalization constant (uncertainty range)

The new diluted tracer solution has now the desired concentration:

$$\frac{3 \cdot 10^{-4} \text{ g}}{125 \text{ mL}} = 2.4 \cdot 10^{-6} \text{ g/mL}$$
 (106)

Now a human error of 0.2 μ L would only have a minor impact:

$$\frac{0.1 \ \mu L}{2 \ mL} + \frac{0.1 \ \mu L}{2 \ mL} = 0.01\% \tag{107}$$

considering the sum of the errors in the dosing of the tracer solution dosing and the subsequent dosing of the liquid to analyze.

An automatic dosing machine has been built for this project and arranged in the lab (more details in 3.2.1). The systematic error of the machine has been estimated to be ± 0.1 g. Taking into account the first dose of 2 mL of tracer solution and the second dose of 2 mL liquid to test, the tracer error becomes:

$$\frac{0.1 \text{ mL}}{2 \text{ mL}} + \frac{0.1 \text{ mL}}{2 \text{ mL}} = 10\% \tag{108}$$

In order to obtain a more acceptable 1% error, we would need to increase the quantity of the two liquids to respectively 20 mL and 20 mL, which would be a massive quantity.

2.5 Analysis of the obtained data

The preliminary data indicate that the fluorescence signal measured with a 8-channel mini spectrometer can be represented by a **two-dimensional fingerprint**, where each coordinate corresponds to a pair of spectral intensities. When this fingerprint is plotted for a series of calibration solutions, distinct clusters appear, demonstrating that a supervised classifier (e.g., SVM) can distinguish pH intervals (at least for a limited pH range).

Because the fingerprint evolves smoothly with pH, a continuous monitoring scheme can track its trajectory over the target range and translate the measured coordinates into a deterministic pH value. This approach would mitigate the stochasticity of machine-learning models that are trained on limited data: the mapping from fingerprint to pH is learned empirically, so the system

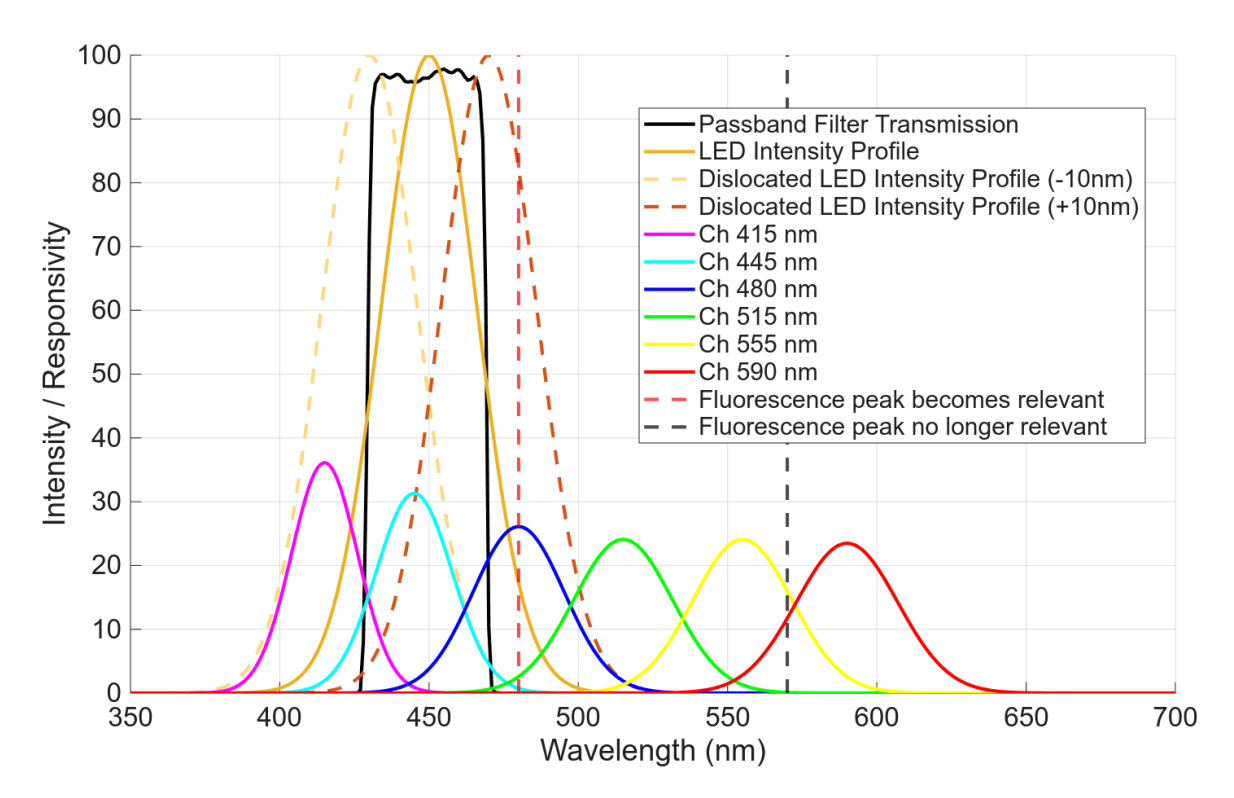


Figure 27: Simulation of an optical compensation circuit using a band-pass filter

is less sensitive to variations that would otherwise arise from an insufficiently representative training set. Expanding the training dataset would require a large number of precisely prepared intermediate pH buffers and extensive measurements, which is costly.

As a preliminary proof of concept, the fingerprint-based method allowed to show the correlation with only lower amount of spectral analyses, making it a practical compromise between accuracy and experimental effort.

Figure 30 shows that, within the pH interval 5.5–7.5, the fluorescence-peak intensity rises monotonically; however, the intensity bands associated with each calibration buffer are relatively wide, reflecting the inherent variability of the measurements. This behavior is quite robust despite the major sources of measurement noise, including but not limited to:

- Sample preparation errors: inaccuracies in buffer preparation, tracer-solution dosing, and mixing.
- LED drift: changes in the LED's peak wavelength and output intensity that disturb normalization and, consequently, the fluorescence response.
- Dark-chamber isolation: illumination leaking in the dark-chamber from external noisy light sources.
- **Temperature variations**: fluctuations that alter both the fluorescence yield and the LED spectrum.
- Electrical noise: pickup in the acquisition circuitry that corrupts the recorded signal.

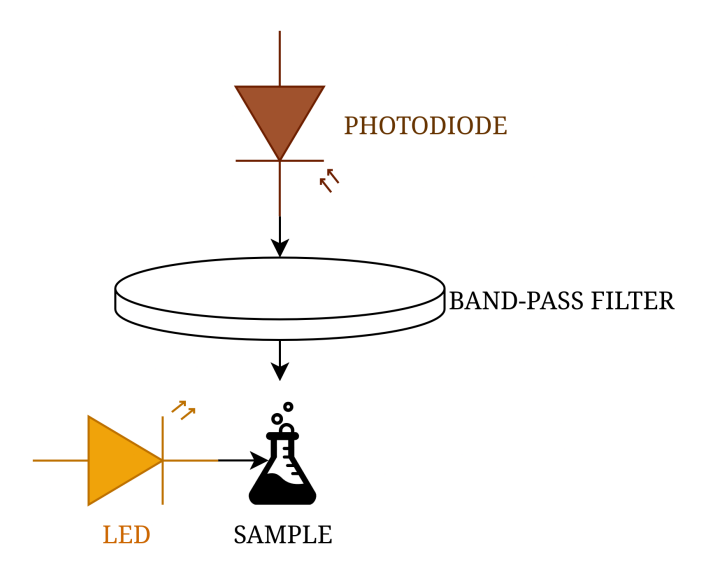


Figure 28: Proposed LED drift compensation circuit

Despite these perturbations, the monotonic trend remains evident, underscoring the reliability of the fluorescence-based pH indicator at least within the stated range.

In Figure 29 the mean response recorded by Channel 4 (centered at 515 nm) rises monotonically with pH up until pH 9 (without the new tolerances, monotonicity stopped at pH 8.5), whereas the signal from Channel 5 (centered at 555 nm) still does not exhibit a clear monotonic trend. While the mean response of Channel 4 (centered at 515 nm) increases monotonically with pH and could, in principle, serve as a single-parameter indicator, relying exclusively on a single wavelength would render the measurement more susceptible to fluctuations in illumination, LED drift, and detector noise. A multi-parameter fingerprint, obtained by combining the signals from several channels, captures a richer representation of the fluorescence spectrum and can mitigate the lack of strict monotonicity of a single channel. The next step is to characterize the full channel-by-channel response for each calibration buffer, thereby **determining** whether each pH value can be mapped to a unique, reproducible spectral finger**print**. Such a fingerprint would provide a more robust basis for a supervised learning model (e.g., SVM) to predict pH with higher precision and reduced sensitivity to noise. The ultimate goal is to generate distinct, non-overlapping clusters within a potentially high-dimensional hypercube. In this representation, each cluster encloses a volume of fingerprint points that can be unequivocally attributed to a particular pH interval. The initial segmentation thus defines the discrete pH classes that the learning model can recognize.

Once the spectral fingerprints are mapped to these volumes, the following step is to perform a continuous interpolation (or regression) over the multidimensional feature space. This would result in a smooth mapping f(x) that estimates pH directly from any fingerprint x, eliminating the reliance on hard classification boundaries and providing a continuous, **analytic measurement function**.

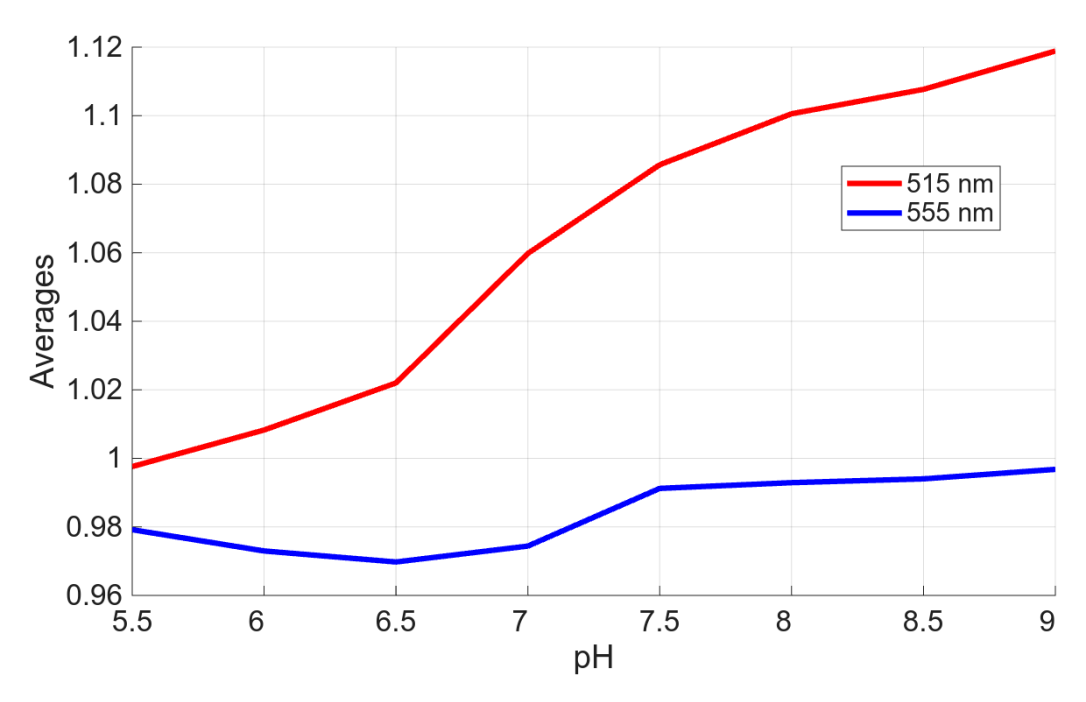


Figure 29: Intensity peaks for the two selected channels (Channel 4 at 515 nm and Channel 5 at 555 nm, normalized over Channel 2 at 445 nm) on multiple captures, with updated tracer solution

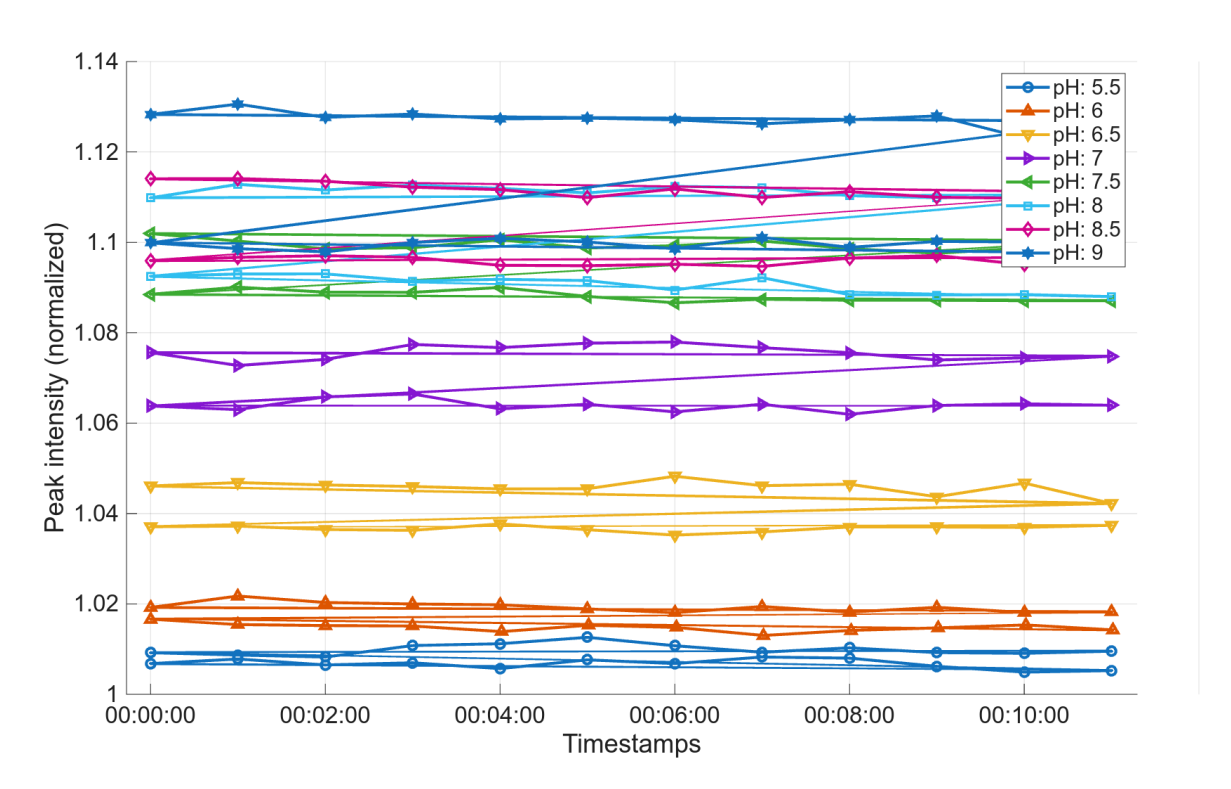


Figure 30: Intensity peaks captured by the spectrometer for every tested pH value during two acquisition cycles with the new tracer solution

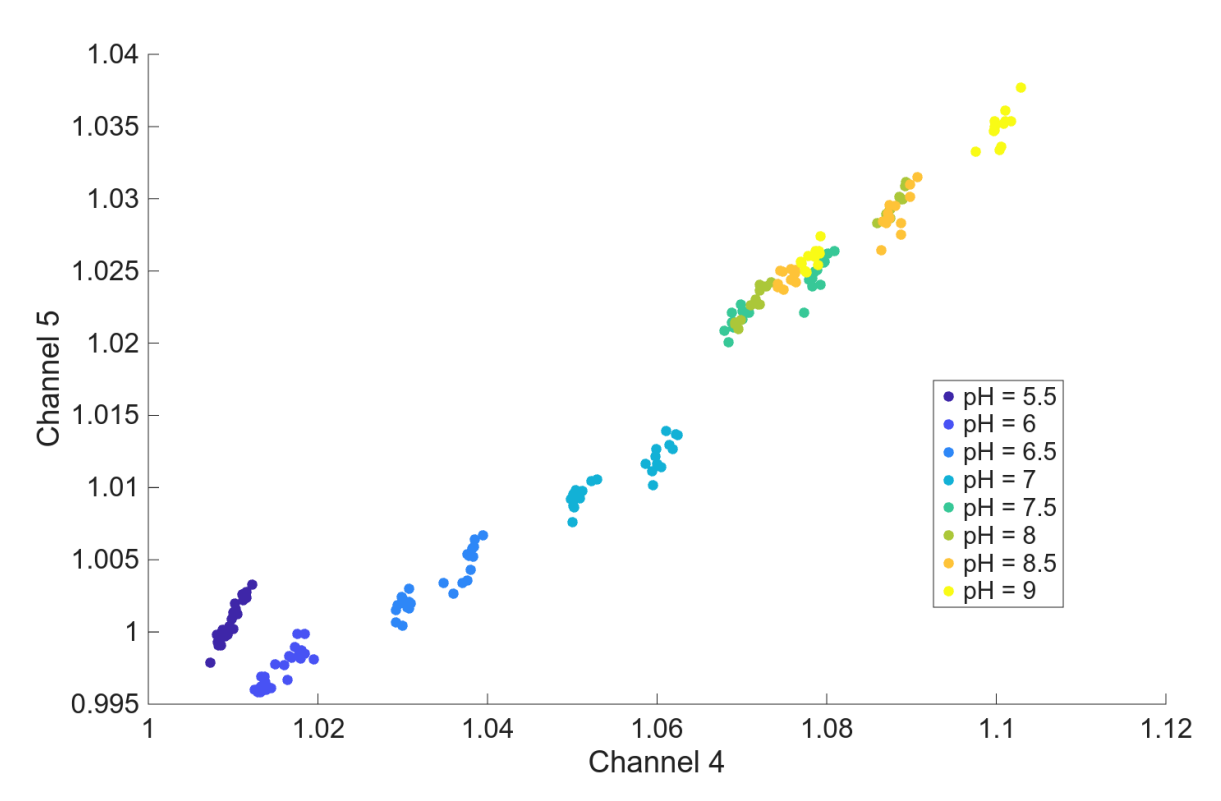


Figure 31: Superposition of scatter plot of two channels (Channel 4 at 515 nm and Channel 5 at 555 nm, normalized over Channel 2 at 445 nm) on multiple captures for the updated tracer solution

3 Measurement device prototype design

The objective was to develop a portable laboratory prototype comprising a passive mechanical mixing circuit, an electronic acquisition system to control liquid flow and capture data, and a software stack for data retrieval and processing. The CAD tool used to design the microfluidic circuit is Autodesk Fusion 360.

3.1 Mechanical design: microfluidic circuit for mixing

In order to reduce the number of required moving parts and lower the power consumption, a simple passive microfluidic circuit was designed to handle the mixing of the tracer solution and the tracked sample.

The geometry optimization began with a simple CAD model created in Autodesk Fusion 360, which was then exported to STL and imported into COMSOL Multiphysics, where it was sliced into a 2D cross-section that defined the fluidic channels. Using COMSOL's combination of physics domains (Laminar Flow interface to solve the Navier–Stokes equations for a viscous, incompressible fluid, and Transport of Diluted Species interface to track the fluorescence tracer concentration under advection and diffusion) the finite-element solver predicted the deterministic streamlines and diffusion layers that characterize laminar flow.

By gradually modifying the channel layout (adding serpentine bends, wall protrusions, or split-and-recombine chambers) and re-simulating, the design was progressively refined without the need for extensive real-life experimental testing.

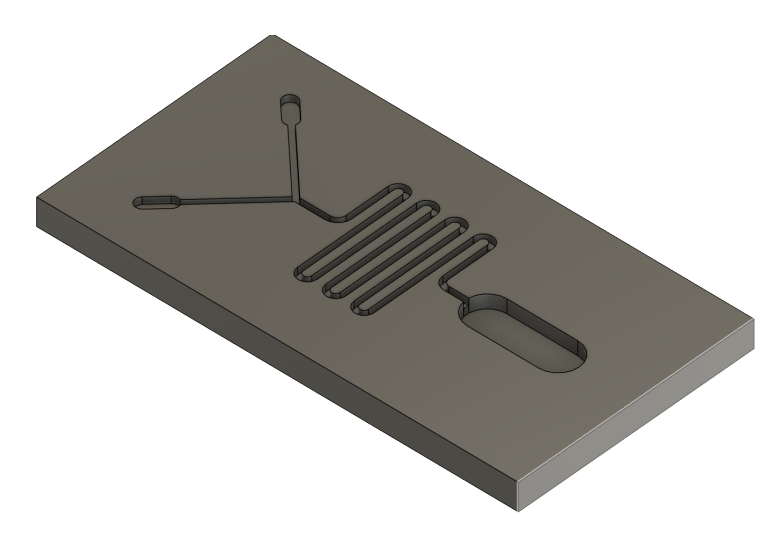


Figure 32: Primitive micro-mixer circuit design

Figure 32 shows an initial microfluidic architecture, that featured a **planar serpentine chan-**nel, the elongated path of which was intended to promote **passive mixing by diffusion**. The circuit included to inlets, one for the tracked and one for the tracer solutions and an outlet chamber to accommodate the resulting mixed solution.

In the improved design (show in *Figure 33*), the split and recombine method has been used to improve the mixing power of the device. The microfluidic circuit consists of several key components (highlighted in *Figure 34*):

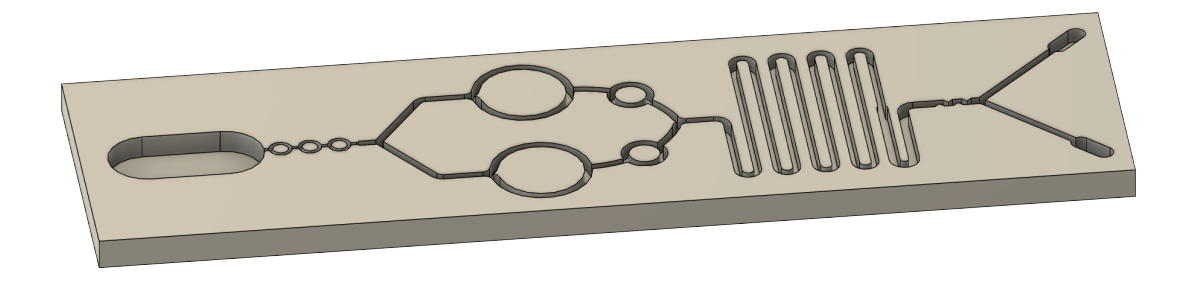


Figure 33: Multistage microfluidic mixing circuit

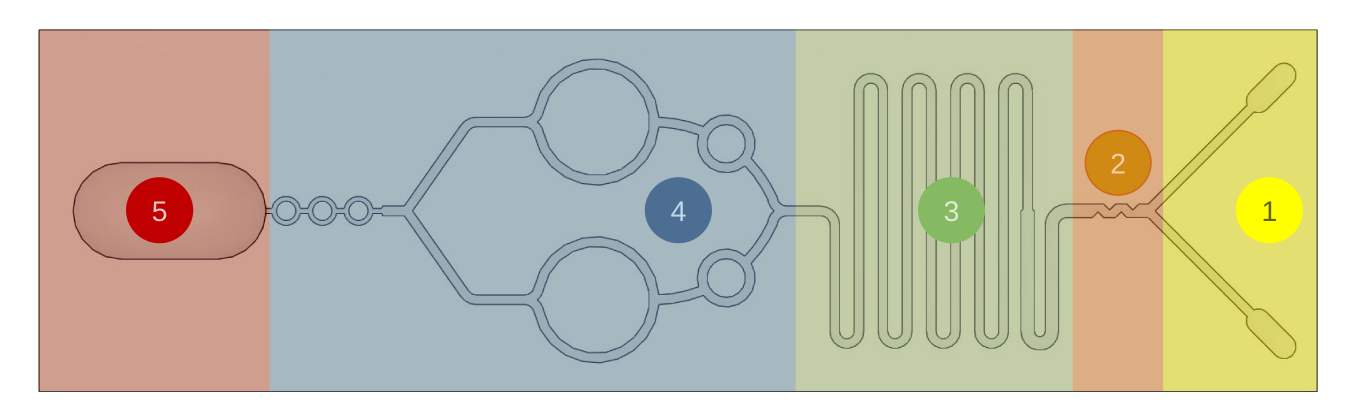


Figure 34: Sections of the microfluidic circuit

- 1. **Inlet Ports:** Two inlet ports are designed to introduce the two solutions to be mixed. One one side the water to analyze is introduced, while on the other the tracer solution.
- 2. Wall Protrusions: This microfluidic circuit employs wall protrusions after the Y junction of channels to disrupt the parallel streams of the laminar flow, enhancing the mixing of two fluids by forcing them to invade each other's flow channel.
- 3. **Serpentine:** After the inlets, the core of the mixing circuit is a long, winding, serpentine channel consisting of many bends and loops. At the beginning of the serpentine, the width of the channel is reduced to further improve the mixing power.
- 4. **Split and Recombine + Channel Width Reduction:** The two solutions then converge in circular mixing chambers, providing a further mixing stage. The streams are finally split and recombined again in three extra circular chambers. The reduced width increases shear and homogenizes the mixture.
- 5. **Output Channel:** The serpentine channel leads into a single output channel. Above the output channel the mini spectrometer and the temperature NTC sensors will analyze the liquid.

Benefits of the serpentine

- Chaotic advection: The serpentine pattern creates a complex flow pattern, while retaining the laminar characteristic of the flow, causing fluid layers to fold, stretch, and recirculate, promoting mixing.
- Increased path length: The serpentine channel increases the total path length the fluids travel, allowing more opportunities for diffusion and advection.
- Diffusion enhancement: The large surface area-to-volume ratio in microfluidic channels increases the role of diffusion, which is enhanced by the serpentine pattern and path length.
- **Simple and robust:** This design is relatively simple to fabricate using standard microfabrication techniques and doesn't require moving parts or external activation.

Role of channel width

The mixing time based purely on diffusion is approximately

$$t_D \approx \frac{w^2}{D} \tag{109}$$

where w is the width channel and D is the diffusion coefficient. The length needed for mixing is then

$$L = (\text{velocity}) \cdot (\text{mixing time}) \approx \left(\frac{Q}{h \cdot \mathscr{M}}\right) \cdot \left(\frac{w^{2}}{D}\right) = \frac{Q \cdot w}{h \cdot D}$$
 (110)

where Q is the flow rate and h is the height of the channel. We could decrease the flow rate Q, but this would be limited by the peristaltic pump specifications. The easiest thing is then reducing the width w.

This geometry is designed to achieve mixing **passively**, meaning no external forces (like magnets, heat, or electrical fields) are used. The design relies on fluid dynamics principles to create chaotic advection at the microscale.

Advection is the process by which a substance, heat, or momentum is carried through a fluid (such as air or water) by the fluid's bulk motion, transporting properties from one location to another.

$$\frac{\partial \phi}{\partial t} + \mathbf{u} \cdot \nabla \phi = 0 \tag{111}$$

where ϕ is the scalar field (e.g., temperature, concentration), **u** is the velocity field, the term $\mathbf{u} \cdot \nabla \phi$ is the mathematical representation of advection.

The design leverages fluid dynamics to simulate the effect of turbulent chaotic mixing, even if only laminar flows are present, increasing contact between solutions and promoting diffusion, ultimately achieving good passive mixing. The serpentine channel is a common and effective design for passive mixing in microfluidics due to its simplicity and ability to generate the necessary flow patterns.

Let's define the concentrations of the tracer solution and the sample to analyze as c_1, c_2 . Table 3 shows the settings used to setup the simulations in COMSOL. The best mixing occurs when the two streams are completely blended, so that they have (almost) the same concentration everywhere. In this case, **the concentration difference** $c_1 - c_2$ **would be close to zero everywhere**. A simple channel with width reduction is largely insufficient to obtain an acceptable enough mixing, as can be clearly seen in Figure 35b. The fluids are not mixing uniformly. Instead, they are forming distinct "segments" of fluid. These segments alternate between being enriched in component 1 (high c_1) and enriched in component 2 (high c_2). In Figure 36b, we can clearly see that the split-and-recombine stage alone fails to produce adequate mixing by diffusion. When it is preceded by a longer serpentine path and wall protrusions that generate chaotic advection, the mixing performance improves markedly. The performance of the full geometry guarantees a good enough mixing performance, as shown in Figure 37b.

The simple difference $c_1 - c_2$ is not a perfect mixing metric. If a region of the channel is empty (no fluid flowing whatsoever), the software will report a perfect mix (zero difference) even though no mixing has occurred. To make the metric meaningful, the two streams must be allowed to propagate throughout the entire geometry. Only then can the difference $c_1 - c_2$ be interpreted as a true indicator of mixing quality.

Name	Value	
Concentration c1	$1 [\text{mol/m}^3]$	
Concentration c2	$1 [\text{mol/m}^3]$	
Diffusion coefficient D_{c1}	$4 \cdot 10^{-10}$ [m ² /s]	
Diffusion coefficient D_{c2}	$2.3 \cdot 10^{-9}$ [m ² /s]	
Inlet inflow velocity	0.01 [m/s]	
Mesh	Extremely fine	

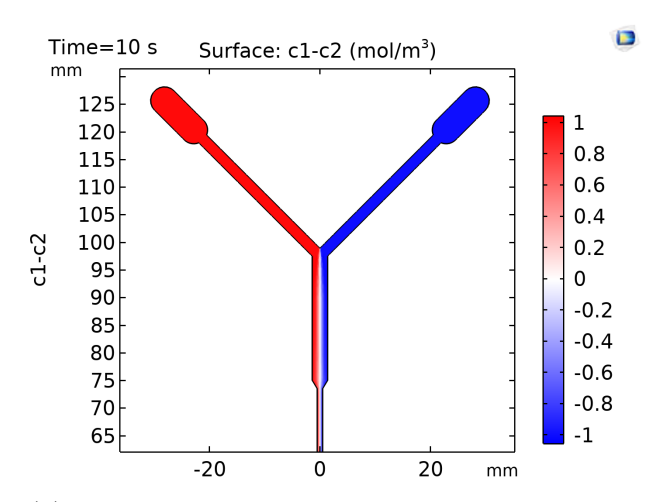
Table 3: COMSOL Multiphysics microfluidic circuit simulation parameters

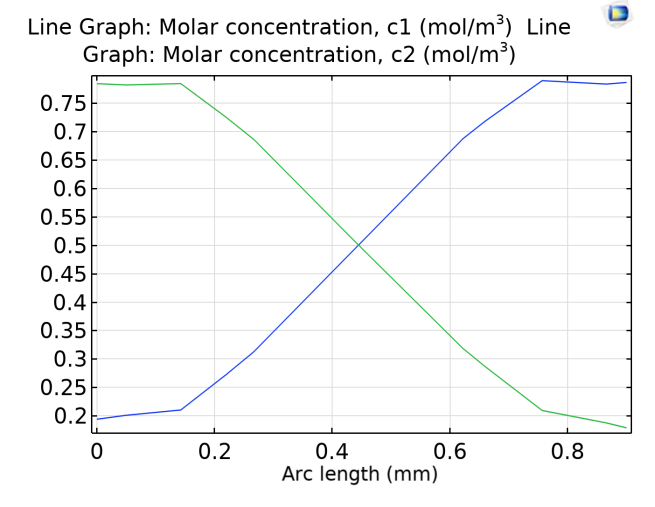
The COMSOL Multiphysics simulations showed that the sequence of a serpentine stage followed by a split-and-recombine stage delivers robust passive mixing. By eliminating the need for active mixing elements, this configuration reduces power consumption and enhances measurement repeatability, because the laminar flow behavior is more predictable.

3.1.1 Lab tests on a scaled up version of the microfluidic circuit

As a precise enough 3D printer wasn't available in the lab, a scaled up version of the device was tested. This wasn't "microfluidic" any more, as the channels were 1 mm wide. Some of the scaled dimensions of the circuit shown in *Figure 38*.

The geometry was evaluated by mixing a colored solution with a transparent one. Although the test was purely qualitative and no quantitative metrics were recorded, the results indicated that the design is sufficiently efficient for repeatable passive mixing. The experiments were





(a) Concentration difference $c_1 - c_2$ of two liquids in a microfluidic circuit simulation in COM-SOL Multiphysics with a simple geometry featuring channel-width reduction

(b) Concentrations at the entrance of the outlet of two liquids in a microfluidic circuit simulation in COMSOL Multiphysics with a simple geometry featuring channel-width reduction

Figure 35: Simulation in COMSOL Multiphysics with a simple geometry featuring channel-width reduction

constrained by the 3D-printing material. Although PLA is relatively non-porous, its high surface friction required a slow flow rate, and because the device was left unsealed the liquid tended to spill from the channels if not handled carefully.

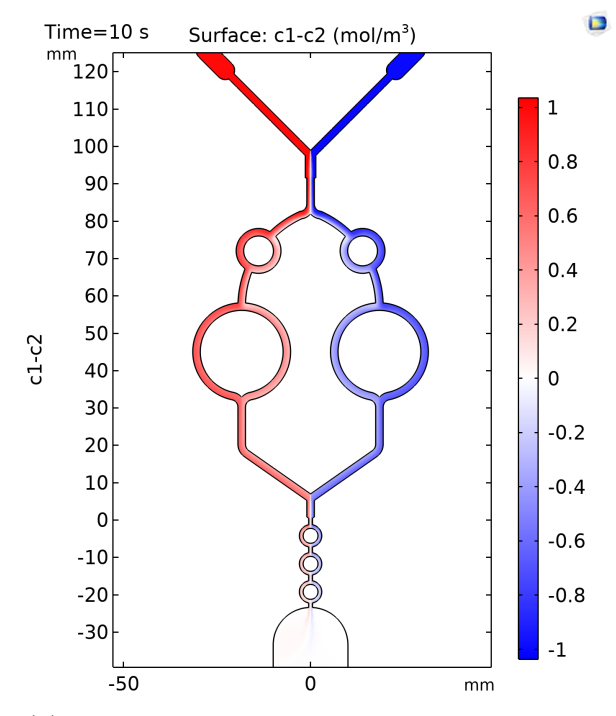
Among the next test that will need to be performed to reach a functional prototype, one of the most relevant ones is the employment of a proper PMMA microfluidic circuit with the proposed geometry.

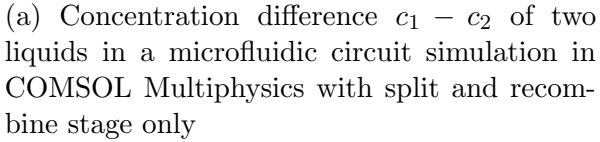
3.1.2 Drift compensation mount for testing

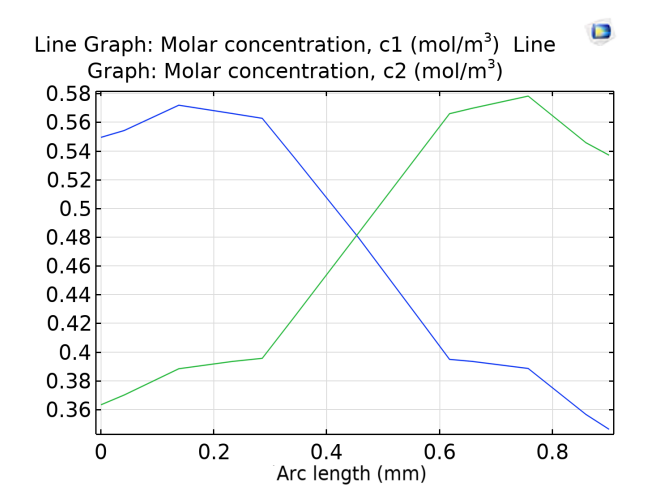
In order to test the compensation given by the compensation circuit shown in *Figure 28*, a mount for the pass-band filter and the photodiode that measures the normalization constant to compensate for the LED drift effect. A simple lock mechanism allows to easily mount the filter and a simple rotation locks it in place (as shown in *Figure 40*). The AS7341 mini-spectrometer device is hold suspended over the outlet of the microfluidic circuit. Some free screws allow to dynamically adjust the height, that should anyway remain consistent throughout the calibration and measurement cycles to avoid it negatively affecting the measurements.

Figure 39 depicts a prototype holder intended to serve as a middle-ground test platform that can be mounted onto the already-printed PLA microfluidic chip. The holder contains a circular aperture positioned at 90° with respect to the mini-spectrometer mounting face, allowing a Thorlabs LED450LW (450 nm, flat-window) to be inserted and illuminate the outlet. The LED draws 90 mW of power and emits a narrow, 450 nm spectrum.

To preserve the integrity of the aperture during fused-filament fabrication, a custom infill pattern was introduced; the pattern is a stiffened, lattice-style scaffold that keeps the hole from collapsing while the rest of the part is printed in a single pass. The holder is designed to interlock with the PLA microfluidic circuit, but because the printed tolerances required the addition



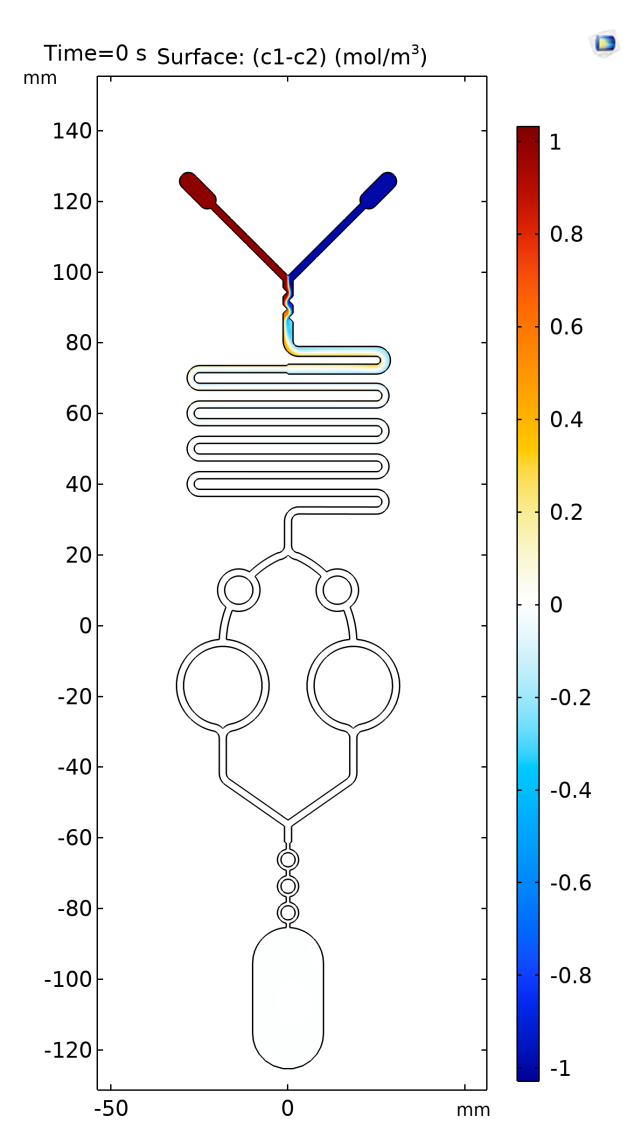




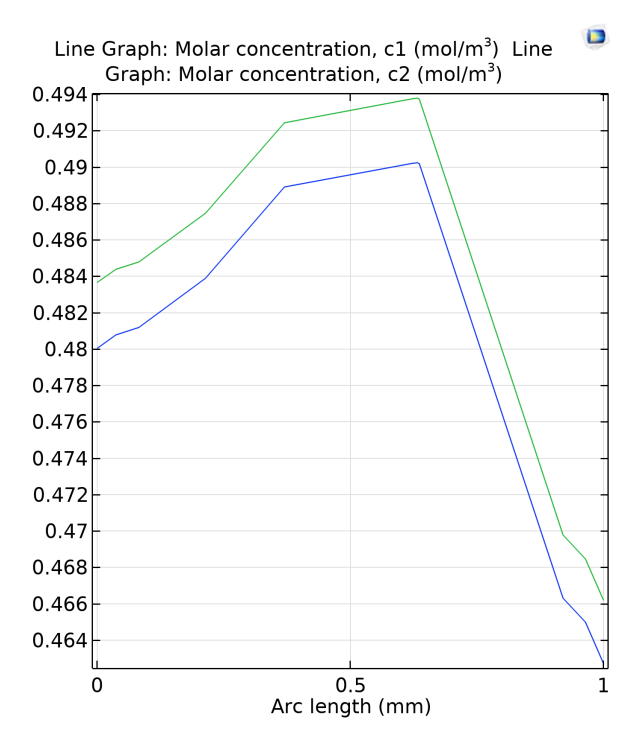
(b) Concentrations at the entrance of the outlet of two liquids in a microfluidic circuit simulation in COMSOL Multiphysics with split and recombine stage only

Figure 36: Simulation in COMSOL Multiphysics with split and recombine stage only

of some clearance, the fit is not perfectly sealed. Consequently, small gaps at the interface must be manually sealed with a thin layer of black tape or a similarly opaque, flexible adhesive, to prevent any optical leakage that could compromise the fluorescence measurements.



(a) Concentration difference c_1-c_2 of two liquids in a microfluidic circuit simulation in COMSOL Multiphysics with the full geometry



(b) Concentrations at the entrance of the outlet of two liquids in a microfluidic circuit simulation in COMSOL Multiphysics with the full geometry

Figure 37: Simulation in COMSOL Multiphysics with the full microfluidic geometry

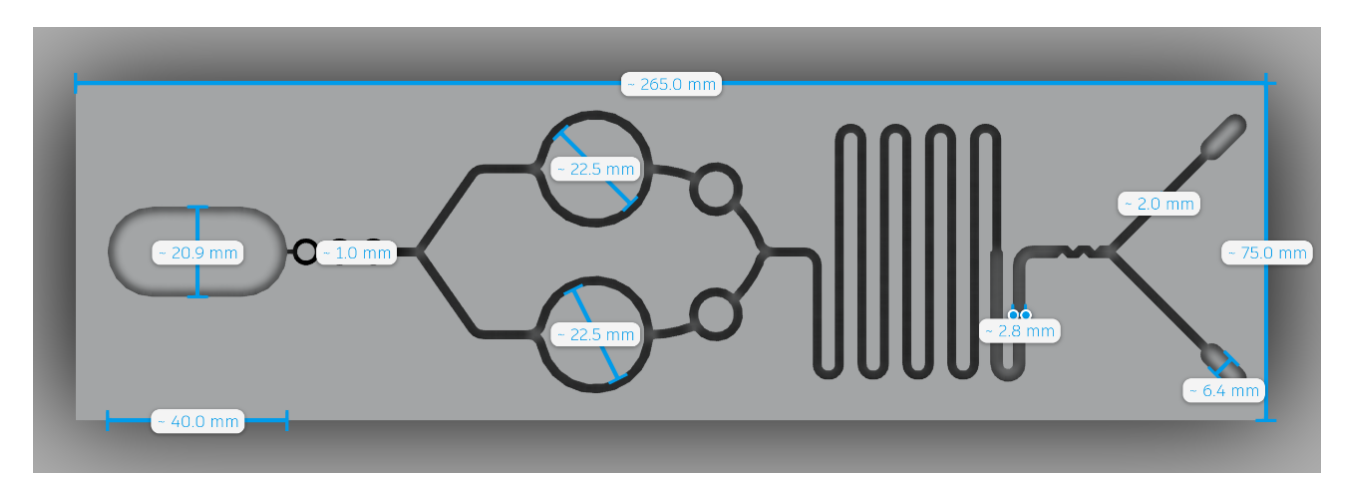


Figure 38: Dimensions of the microfluidic circuit prototype that was tested in the lab (scaled up version)

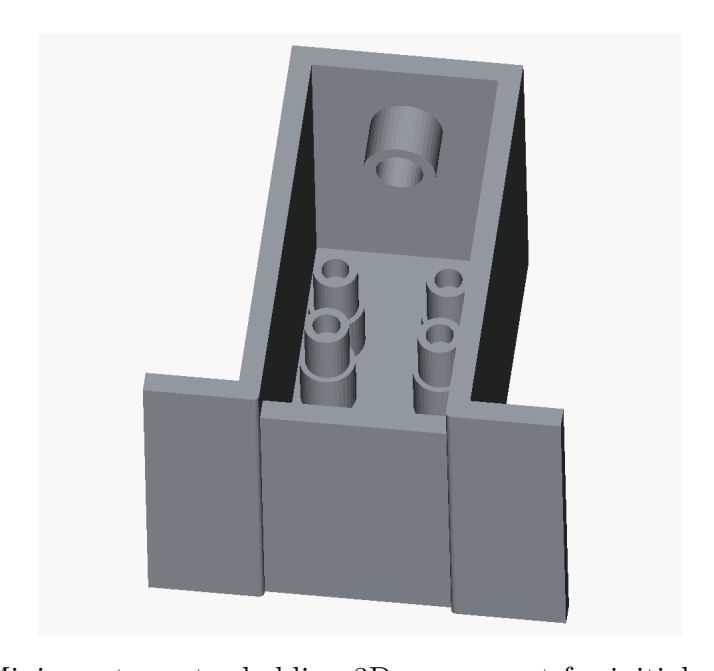


Figure 39: Mini spectrometer holding 3D component for initial circuit testing

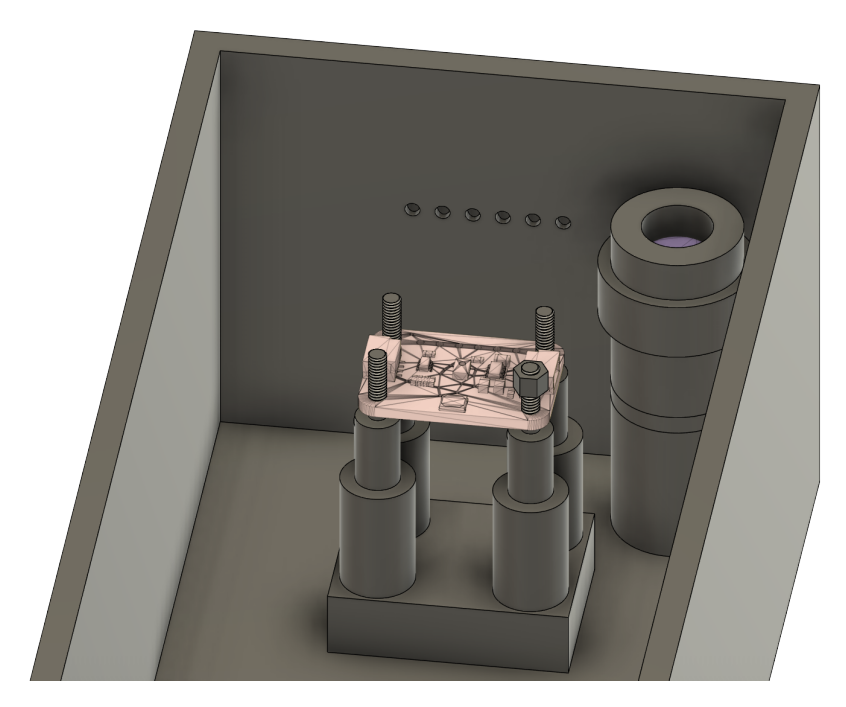


Figure 40: Microfluidic device case, mini-spectrometer mount and LED drift compensation circuit

3.2 Electronic design: custom PCB board

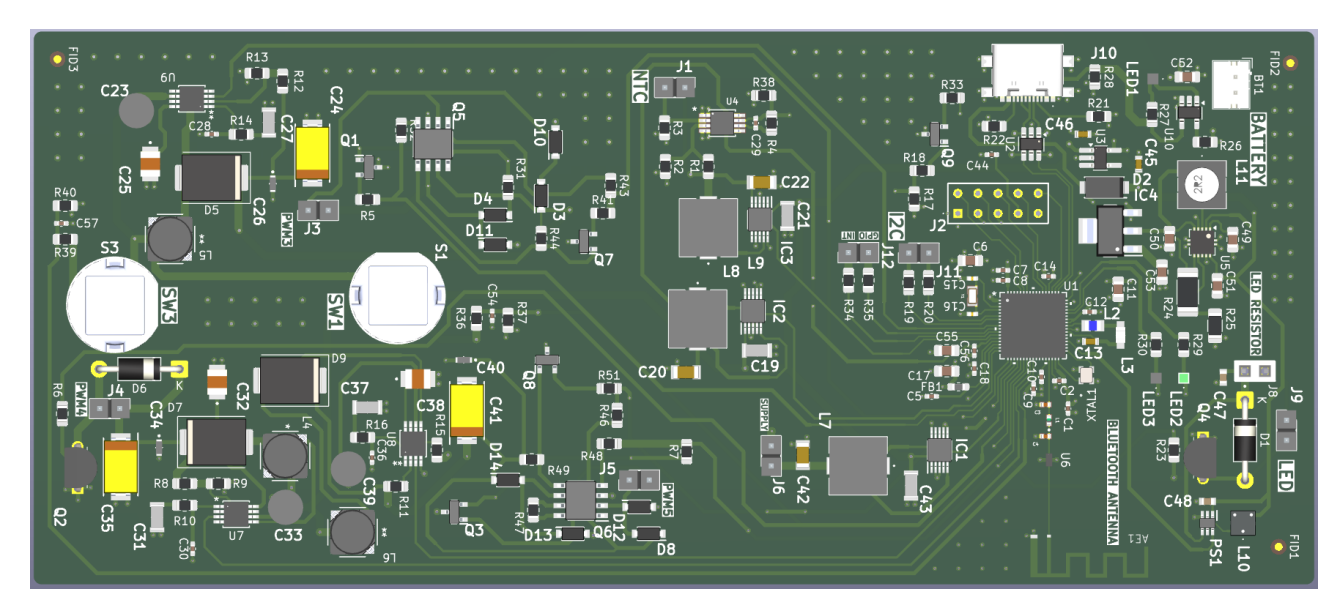


Figure 41: PCB of the custom electronic circuit for data acquisition, temperature sensing, dosing pumps control and LED control

A custom **4-layer PCB prototype** was designed to evaluate the feasibility of the proposed measurement scheme in a real-device setting, rather than relying solely on laboratory simulations. The thickness is 1.6 mm and the chosen material is standard FR4. The first layer is the one where all components are located, while the other three are dedicated to filled zones to reduce impedances and cleaner tracks.

The choice of a 4-layer stack is also to have a better control over trace width and spacing, facilitating impedance matching, which is critical for effective antenna performance. The width of the signal trace can be adjusted to achieve the desired impedance (commonly 50Ω for antennas). In a microstrip we have a trace on one side of the PCB and a ground plane on the opposite side. Impedance can be controlled by adjusting trace width and substrate thickness. Wider traces reduce impedance, while narrower traces increase it. The distance between the trace and the ground plane or adjacent traces affects impedance: increasing the spacing can lower the effective impedance.

A 4-layer PCB could also include dedicated ground planes that reduce electromagnetic interference (EMI), enhancing signal integrity for the antenna's performance.

The designed PCB board has at its core the STM32WB55RG microprocessor (VFQFPN68 package), produced by ST Microelectronics. The device has three 16-bit timers, 1 32-bit timer and two 16-bit ultra-low-power timers, Bluetooth and serial USB communication native support. The CPU is a dual-core and comprises a Arm Cortex-M4 (up to 64 MHz) and a Arm Cortex-M0+ (32 MHz). It comes with 1 MB Flash and 256 kB SRAM. Its operating voltage range is 1.71 to 3.6 V. Table 4 shows the port configuration of the microcontroller.

The implemented features are:

• Serial communication via USB-C: A web application communicates with the embedded board over a serial link through the USB-C port, allowing bidirectional transfer of

commands and sensor data. A Bluetooth radio is also present.

- Battery-charging circuitry: When a charger is connected to the USB-C port, the board is powered directly from the cable while the onboard battery is simultaneously charged and bypassed.
- **Dosing pumps control**: The board controls the dosing operations through a combination of timing and PWM control. Three pumps can be driven, two of which are equipped with H-bridge drivers to enable bidirectional flow.
- Mini-spectrometer data acquisition: The AS7341 spectrometer is addressed over I2C and is triggered to capture spectral data at predefined intervals. The board is also capable of supplying power to the external mini-spectrometer PCB.
- **Temperature sensing**: An NTC thermistor is read through a Wheatstone bridge followed by an instrumentation amplifier, providing calibrated temperature measurements.
- LED intensity control (PWM): the LED intensity can be precisely controlled using PWM. A socket to insert a suitable resistor is conveniently placed next to the pins for the LED.

Power isolation of subsystems

To protect the accuracy of the measurements and the repeatability of the PWM signals, every subsystem is powered by its own dedicated power converter. This isolated supply limits noise propagation that could otherwise affect sensor readings or reduce the precision of timing as a dosing mechanism for the pump drivers.

3.2.1 Peristaltic pumps control circuits

For the purpose of mixing, peristaltic pumps were employed because they are inexpensive and readily available in the laboratory. To quantify the **dosing precision** of the pump, the following test has been carried out:

- 1. A single pump was connected to two reservoirs: one representing the inlet and the other the outlet.
- 2. The tubing was filled with liquid, thereby neglecting any propagation delay through the lines.
- 3. A custom software interface (more details in paragraph 3.3.1) allowed the duty cycle of the PWM pump driver to be set. For each chosen duty cycle, ON times of 1, 2, 5 and 10 seconds were applied. For each ON time, the measurement was repeated three times, with the liquid dispensing stopped by software (to avoid adding human error).
- 4. The tubes were left largely untouched to avoid perturbing the experimental set-up.

Table 4: Partial port configuration of the STM32 micro-controller

Component	Port	Configuration	Description	
<u></u>			<u> </u>	
TIM17_CH1	PA10	PWM Generation	Control of the LED	
$TIM2_CH2$	PA1	PWM Generation	Control of the dosing pump 1 (forward)	
$TIM2_CH3$	PA2	PWM Generation	Control of the dosing pump 1 (reverse)	
$TIM16_CH1$	PA6	PWM Generation	Control of the dosing pump 2 (only forward)	
$TIM1_CH2$	PA9	PWM Generation	Control of the dosing pump 3 (forward)	
TIM1_CH3	PA10	PWM Generation	Control of the dosing pump 3 (reverse)	
ADC1_IN5	PA0	Single-ended ADC	NTC temperature acquisition	
ADC1_IN9	PA4	Single-ended ADC	Battery charge voltage acquisition	
GPIO_EXTI3	PC2	External interrupt	AS7431 mini-spectrometer interrupt	
GPIO_EXTI1	PD1	External interrupt	Hardware input button BTN1	
GPIO_EXTI5	PC5	External interrupt	Hardware input button BTN2	
$GPIO_OUT$	PA8	3.3V output	Enable battery voltage acquisition	
$GPIO_OUT$	PB14	3.3V output	PCB LED1 output	
$GPIO_OUT$	PB13	3.3V output	PCB LED2 output	
$GPIO_OUT$	PA1	3.3V output	Activate instrumentation amplifier for NTC acquisition	
$GPIO_OUT$	PC1	3.3V output	GPIO connection to AS7431 mini-spectrometer	
$GPIO_OUT$	PC3	3.3V output	Activate NTC temperature acquisition power supply	
$GPIO_OUT$	PA3	3.3V output	Activate AS7431 mini-spectrometer power supply	
$GPIO_OUT$	PC0	3.3V output	H-Bridge, toggle pump 1 PWM power supply	
$GPIO_OUT$	PC4	3.3V output	H-Bridge, toggle pump 2 PWM power supply	
$GPIO_OUT$	PA8	3.3V output	H-Bridge, toggle pump 3 PWM power supply	
I2C1_SCL	PB8	I2C bus	Provides the serial clock for the I2C1 bus	
I2C1_SDA	PB9	I2C bus	Carries the bidirectional data signal	
VREFBUF_OUT	VREF+	2.048V output	Delivers a stable reference voltage to the ADC	
USB_DM	PA11	Data line	Differential data line for USB signal's negative phase	
USB_DP	PA12	Data line	Differential data line for USB signal's positive phase	

Consequence of the principle of communicating vessels

To keep the tube fully filled during data collection and to prevent natural back-flow or forward-propagation when the pump is stopped, liquid level (subject to atmospheric pressure) and outlet port are positioned at the same vertical height. This significantly slowed down the back/forward propagation of the liquid in the tubes while the pump wasn't running.

The achievable precision of the weighing stage was ± 0.1 g. This precision was mainly limited by the following sources of noise:

- Variable pressure at the inlet and outlet, arising from the *principle of communicating* vessels;
- Air bubbles that form in the tubing and interfere with the flow;
- Execution delays introduced by the micro-controller firmware.

Mitigating timing related noise

The dosing algorithm is purely time-based, which **presupposes that the system's initial state is known**. If the delivery tubes contain residual fluid when a dispensing cycle starts, the volume pumped will deviate from the target. A robust countermeasure is to reverse the pump at maximum speed immediately before each new dosing cycle, thereby emptying the tube completely. This "flush-back" step restores a known starting volume and **substantially reduces timing-induced dosage variability**.

3.2.1.1 H-Bridge configuration

The circuit presented in Figure 42 is a **H-bridge configuration** used to drive a load, denoted as M (DC motor of the peristaltic pumps). The H-bridge consists of four MOSFET transistors arranged in a quadrilateral formation. On the high-side, there are two P-MOS that are activated by two N-MOS transistors, while on the low-side there are other two N-MOS transistors. The reason why P-MOS transistors have been employed on the high side is so that they can be turned on with a gate voltage that is lower than the supply voltage.

The load M is connected between the midpoint of two opposing transistors. When the appropriate pair of transistors is turned on, current flows through M in one direction; when the other pair is turned on, current flows in the opposite direction, thereby providing **bidirectional** control of the pump motor.

Diodes are placed in parallel with each transistor to protect against inductive kickback when driving inductive loads.

The circuit is powered by a voltage source $V_{DD}=12$ V. The voltage source is handled by a MAX1790EUA+T, which is a highly efficient DC-DC boost switching regulator. It features a quite high quiescent current of 2 mA when not used. However, this component can be disabled through a dedicated pin, effectively reducing the quiescent current to zero when not in use, making it particularly beneficial for battery-powered applications like this one. The device operates with an input voltage range of 2.6V to 5.5V and can provide an adjustable output voltage from 1.2V to 12V.

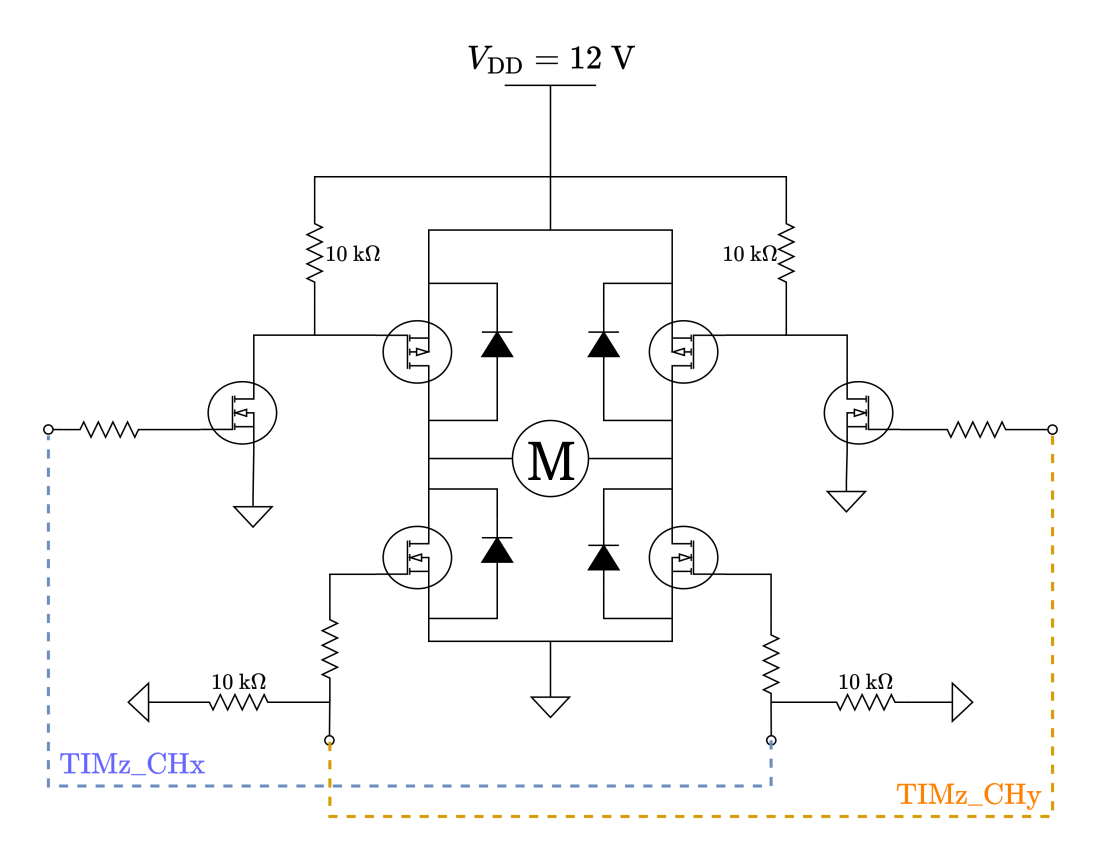


Figure 42: H-Bridge circuit for handling the peristaltic pumps

The dashed boxes indicate the two independent channels (TIMz_CHx and TIMz_CHy) used to control the transistors and, consequently, the direction of current through load M. This two channels are connected to pins of the microcontroller that can handle PWM signals through hardware timers, allowing to adjust the speed at which the DC motor spins.

Figure 43 shows the PCB schematic that implements the H-bridge configuration, enabling it to reverse the polarity applied to the pump, allowing for bidirectional rotation. The speed is controlled via Pulse Width Modulation (PWM). The signals TIM2_CH3_PWM and TIM2_CH4_PWM come from the microcontroller and provide the PWM control signals that modulate the motor speed. D_3 , D_4 , D_{10} and D_{11} are rectifier diodes. They are crucial for "flyback" protection: when the transistors switch off, the inductive load of the pump's motor generates a voltage spike (flyback voltage) that can damage the transistors. These diodes provide a path for the current to flow, preventing the voltage spike.

3.2.1.2 Characterization of the peristaltic pumps

In order to **characterize the pumps** and obtain a mathematical equation that correlates the quantity of liquid supplied by the pump given a period in which it has been switched on, the following steps have been followed: The **mean weights** have been evaluated as

$$\overline{W}_t = \frac{1}{|\mathcal{I}_t|} \sum_{k \in \mathcal{I}_{\sqcup}} W_t \tag{112}$$

where \mathcal{I}_t represents all the times t at which data was collected. The absolute spread (devi-

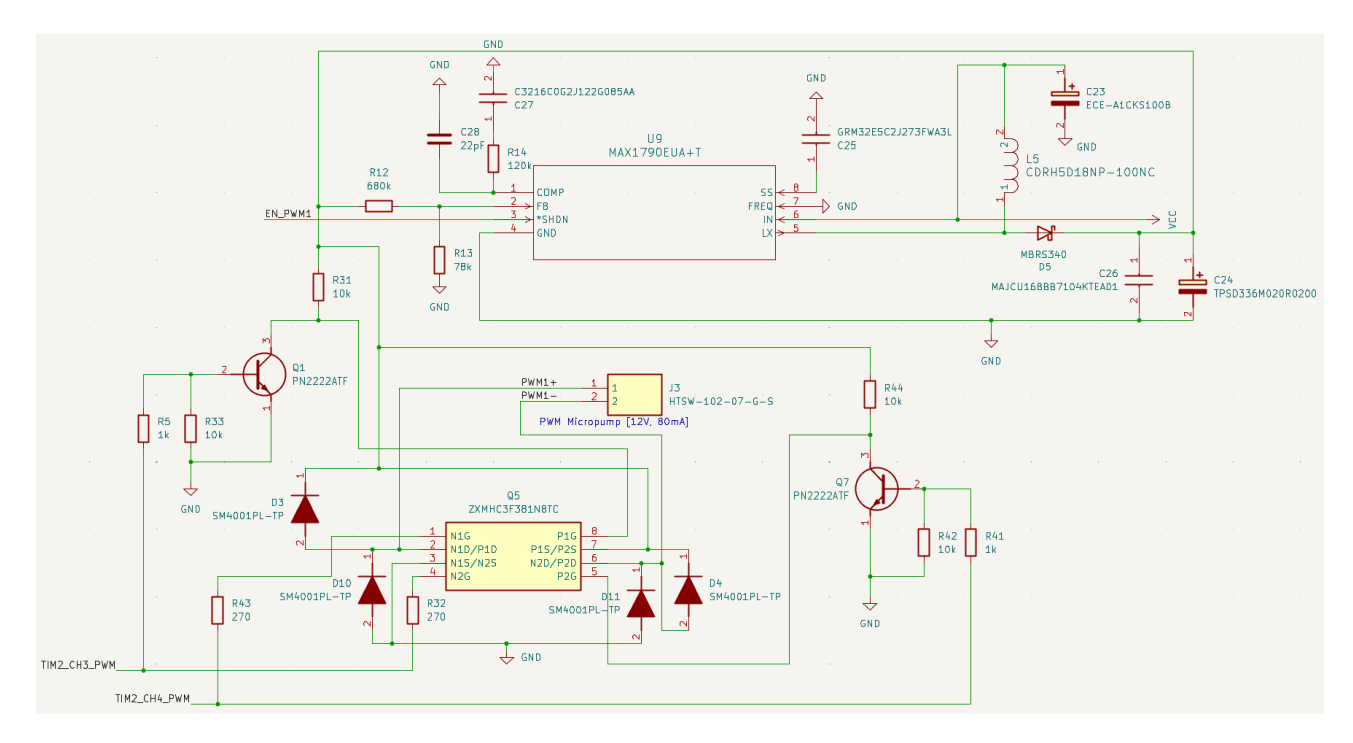


Figure 43: H-Bridge configuration implementation schematic for driving one of the peristaltic pumps (DC motor)

ation) is then given by

$$\Delta_t = \max W_t - \min W_t \tag{113}$$

The relative spread (percentage deviation) is finally

$$\delta_t = \frac{\Delta_t}{\overline{W_t}} \times 100\% \tag{114}$$

ON TIME [s]	MEAN WEIGHT [g]	DEVIATION	DEVIATION PERCENTAGE [%]
0.1	0.18	0.07	38.889 %
0.2	0.29667	0.04	13.483~%
0.5	0.675	0.05	7.4074~%
1	1.2017	0.11	9.154~%
1.5	1.7783	0.11	5.6232~%
3	3.39	0.11	3.2448~%
5	5.6133	0.12	2.1378 %
8	8.83	0.2	2.265~%

Table 5: Data table for the characterization of the quantity of liquid supplied by the peristaltic pump at PWM duty cycle 45%

Figure 44 shows the characterization of the pump when the duty cycle of the PWM is set to 50%. The numerical results are shown in Table 5. The **deviation** tells how much the actual delivery can swing around the mean quantity (taken as reference value for a given amount of

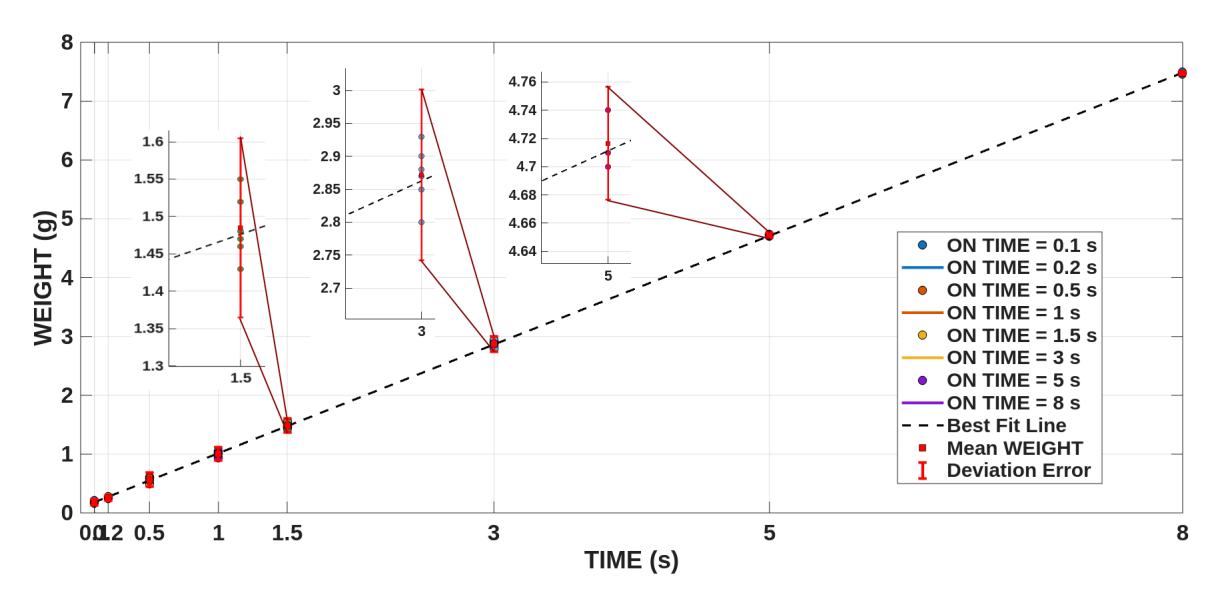


Figure 44: Characterization of the quantity of liquid supplied by the peristaltic pump at PWM duty cycle 45% ($W_t = 0.9243t + 0.0896$)

on time) useful for safety margins or for deciding if the pump is "good enough" for precision work.

Another parameter that should be characterized is the time needed for the empty tube to be filled with water. In fact, every time a new cycle starts, as already mentioned the tube must be emptied to guarantee that known initial conditions are reached. The tube should be filled as quickly and precisely as possible; then when fully filled, the speed should be reduced to increase precision and dispense the right quantity of liquid using the previously evaluated characterization.

Another parameter that should be quantified is the **time needed for the empty tube to be filled with water**. At the beginning of each new cycle the tube is emptied to ensure reproducible initial conditions, as previously mentioned. Once emptied, the tube must be refilled with water as quickly as possible. The strategy is to operate the pump at a high flow rate during the early phase of filling, thereby minimizing the time to reach a fully filled state, while retaining a high controllability. Once the tube is full, the flow is throttled to a lower speed. This second, slower regime improves the precision of the subsequent dispensing step and guarantees that the previously characterized pump-volume relationship is honored.

3.2.2 Temperature acquisition circuit

The circuit shown in *Figure 45* takes an analog voltage proportional to temperature from an NTC thermistor and converts it into a digital signal for the microcontroller.

The circuit leverages a Wheatstone bridge (Figure 46) for accurate temperature measurement and includes amplification and filtering to improve signal quality by filtering additive noise (differential acquisition). In fact, instrumentation amplifiers are specifically designed to reject common-mode noise. This helps ensure that the measurement is accurate, even in noisy environments.

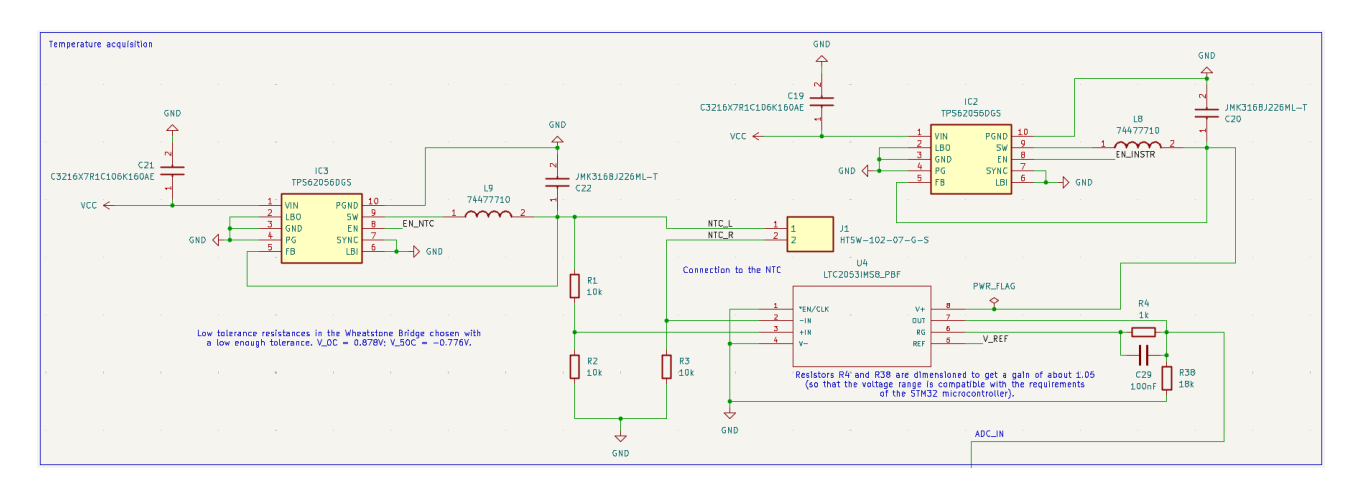


Figure 45: Temperature acquisition circuit

$$V_{\rm AB} = V_{\rm A} - V_{\rm B} = V_{\rm CC} \left(\frac{R_2}{R_1 + R_2} - \frac{R_3}{R_3 + R_{\rm NTC}} \right)$$
 (115)

where $R_{\rm NTC}$ is the resistance of the NTC sensor.

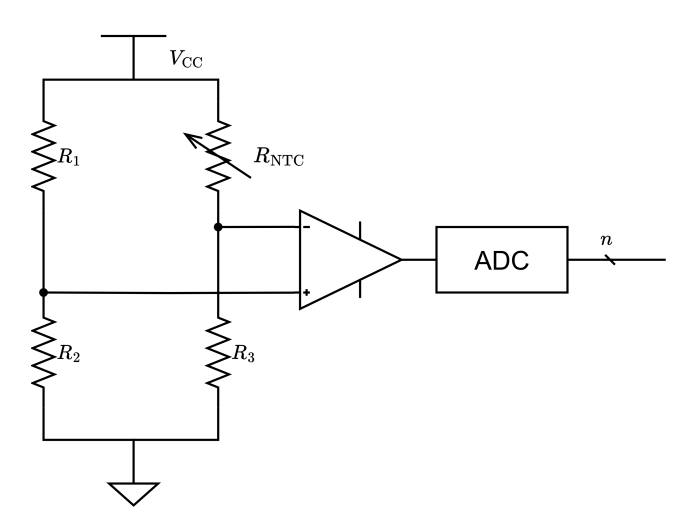


Figure 46: Wheatstone Bridge circuit

Let's pick $R_1=R_2=R_4=10~\mathrm{k}\Omega$, while $V_{\mathrm{CC}}=3.3\mathrm{V}$. The accuracy of the measurement relies on the bridge being well-balanced: careful component selection and tolerance matching are then critical. Considering the datasheet of a PT100 as a reference, at $25^{\circ}C$ we have that $R_{\mathrm{NTC}}=10k\Omega$, at $0^{\circ}C$ we have that $R_{\mathrm{NTC}}=32.74k\Omega$ and at 50° we have that $R_{\mathrm{NTC}}=3.604k\Omega$.

$$@25^{\circ}C \implies V_{AB} = 3.3V \left[\frac{10k}{10k + 10k} - \frac{10k}{10k + 10k} \right] = 0V$$
 (116)

$$@0^{\circ}C \implies V_{AB} = 3.3V \left[\frac{10k}{10k + 10k} - \frac{10k}{10k + 32.74k} \right] = 0.878V$$
 (117)

$$@50^{\circ}C \implies V_{AB} = 3.3V \left[\frac{10k}{10k + 10k} - \frac{10k}{10k + 3.604k} \right] = -0.776V$$
 (118)

As the ADC only accepts positive voltages, a precise $V_{\rm REF}$ is required. It's provided by the STM32 microcontroller: $V_{\rm REF+}=2.048{\rm V}$.

$$\implies V@0^{\circ}C = 2.048V + 0.878V = 2.926V$$
 (119)

$$\implies V@50^{\circ}C = 2.048V + (-0.776V) = 1.272V$$
 (120)

Taking into account the gain of the instrumentation amplifier

$$Gain = 1.1 \implies Gain = \frac{R_B}{R_A} + 1 \implies R_B = 1k\Omega \quad R_A = 10k\Omega$$
 (121)

$$\implies \begin{cases} V@0^{\circ} = 2.926 \text{V} \cdot 1.1 = 3.22 \text{V} \\ V@50^{\circ} = 1.272 \text{V} \cdot 1.1 = 1.40 \text{V} \end{cases}$$
 (122)

In order to stay away from the 3.3V limit, a gain of 1.055 is selected:

$$Gain \approx 1.05 \implies R_B = 1k\Omega \quad R_A = 18k\Omega$$
 (123)

$$\implies \begin{cases} V@0^{\circ} = 2.926 \text{V} \cdot 1.055 = 3.087 \text{V} \\ V@50^{\circ} = 1.272 \text{V} \cdot 1.055 = 1.342 \text{V} \end{cases}$$
 (124)

The 12-bit precision of the microcontroller's ADC can represent a voltage with $2^{12} = 4096$ discrete levels. This means the ADC can distinguish between 4096 different voltage values within its input range (the smaller the voltage range and the higher the accuracy of the ADC).

3.2.3 Battery charger circuit

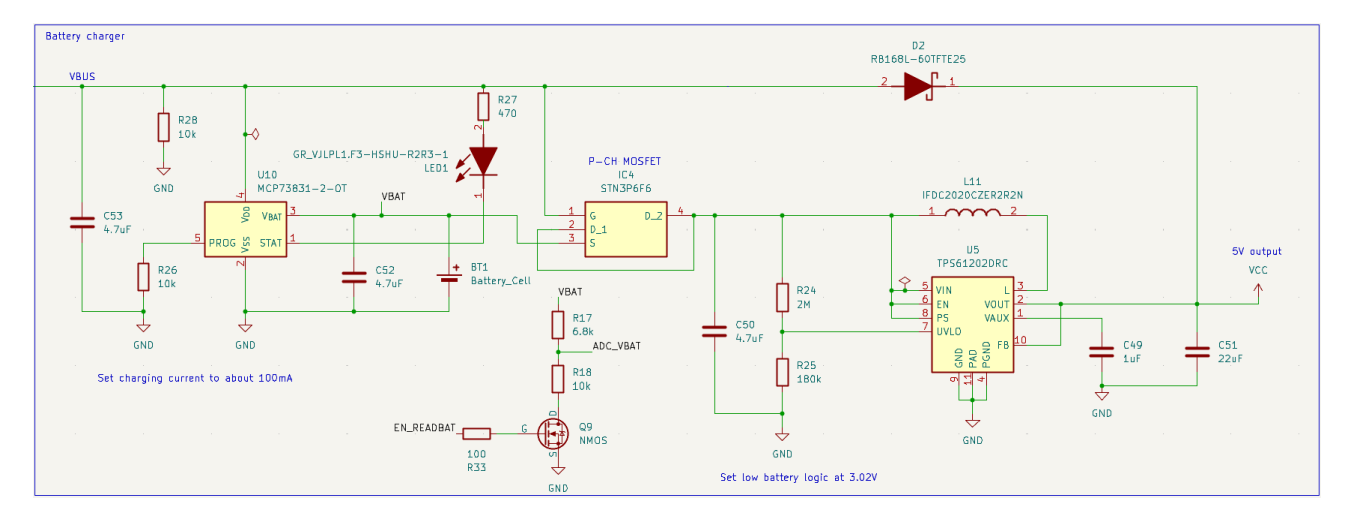


Figure 47: Battery charger circuit

Figure 47 shows a standard **constant-current charging circuit**, designed to charge a single-cell Lithium-Ion (Li-ion) or Lithium-Polymer (Li-Po) battery. *IC4* (STN3P66) is a PMOS used as a power switch, which allows the charging current to flow to the battery or bypass it completely to directly power the PCB circuitry. The *LED1* is used to signal to the user that the battery is being charged.

The MCP73831 initially provides a constant current. As the battery voltage approaches its full charge voltage (which is typically around 4.2 V for a Li-Ion battery), the controller switches to a constant-voltage mode, maintaining the voltage while reducing the current.

R25 (10 k Ω) is the key component for setting the charging current: the charging current is determined by the voltage at the PROG pin of the MCP73831, which depends on the value of this resistor. According to the official datasheet, scaling can be obtained by placing a programming resistor (R_{prog}) between the PROG input and V_{BUS} . The **program resistor** and the charge current are calculated using the following equation:

$$I_{\text{REG}} = \frac{1000 \text{ V}}{\text{R}_{\text{prog}}} = \frac{1000 \text{ V}}{10 \text{ k}\Omega} = 100 \text{ mA}$$
 (125)

This is the actual current that the battery will draw.

The main ability of this circuit is to power the PCB directly from the external power source (V_{BUS}) while the battery is charging. First, the charger pushes a constant current into it. Then, as the battery fills up, its voltage goes up. Once the battery reaches its maximum safe voltage, the charger stops pushing as much electricity. Instead, it focuses on keeping the battery's full charge voltage, even though the current continues decreasing. This is **constant-voltage mode**.

The P-MOS transistor plays a crucial role in this bypass functionality: it controls whether power is drawn from the $V_{\rm BUS}$ input or from the battery. Under normal operating conditions, the P-MOS is driven ON (conductive). This means $V_{\rm BUS}$ is connected directly to the input of the TPS61202DRC.

- Charging: When V_{BUS} is available, it allows the MCP7351 to charge the battery while simultaneously powering the load through the TPS63020.
- Direct Power Delivery: When the battery is disconnected, the P-MOS control keeps the load powered from $V_{\rm BUS}$.

The STAT pin allows the connection of a LED for hardware charge status indication Let's break down how the battery voltage is being measured and used to communicate charging status and potentially optimize charging parameters through the action of the microcontroller. The $V_{\rm BAT}$ node (where the battery connects) is directly connected to the built-in analog-to-digital converter (ADC) of MCP7351, which directly samples the battery voltage. Typically, a 6 μ A current is sourced to the $V_{\rm BAT}$ pin to determine if a battery is present or not. The PROG pin acts as charge enable, as it sets the UVLO conditions to start the charging cycle. An internal UVLO circuit monitors the input and waits for the input supply to rise over the UVLO threshold. When the input supply rises to a level 150 mV greater than the battery voltage before the MCP7351 became operational, the event of the battery being present is detected. Based on the voltage data, the microcontroller could deactivate the charging procedure when the battery reaches the full voltage, or a defined battery preservation threshold.

3.2.4 LED driver circuit

Figure 48 shows a boost converter topology that allows a lower input voltage $(V_{\rm CC})$ to be stepped up to a higher voltage for driving an LED. Ceramic capacitors act as input and output

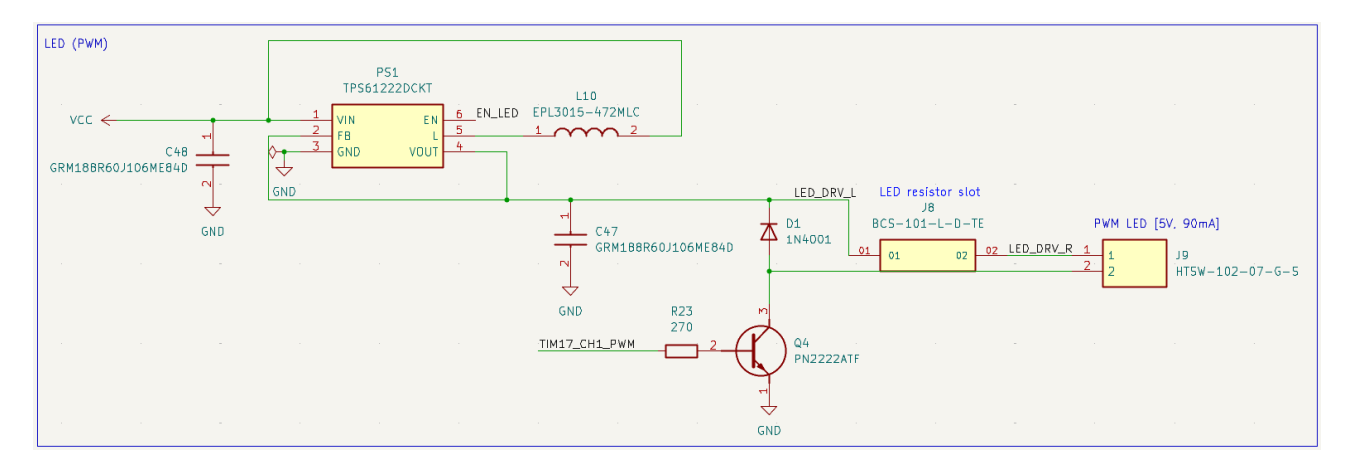


Figure 48: LED intensity control circuit (PWM)

filter capacitors to help smooth out the voltage ripple and noise on both the input and output sides of the boost converter.

The EN input enables or disables the boost converter and is directly controlled by a GPIO_OUT pin of the microcontroller. This allows to avoid quiescent current when this part of the circuit isn't used.

The PWM signal from TIM17_CH1_PWM controls the transistor that generates the PWM signal. A user-accessible resistor slot allows the board to be tuned to any LED, eliminating the need for a separate prototype for each light source.

3.3 Software design: data harvesting and evaluation

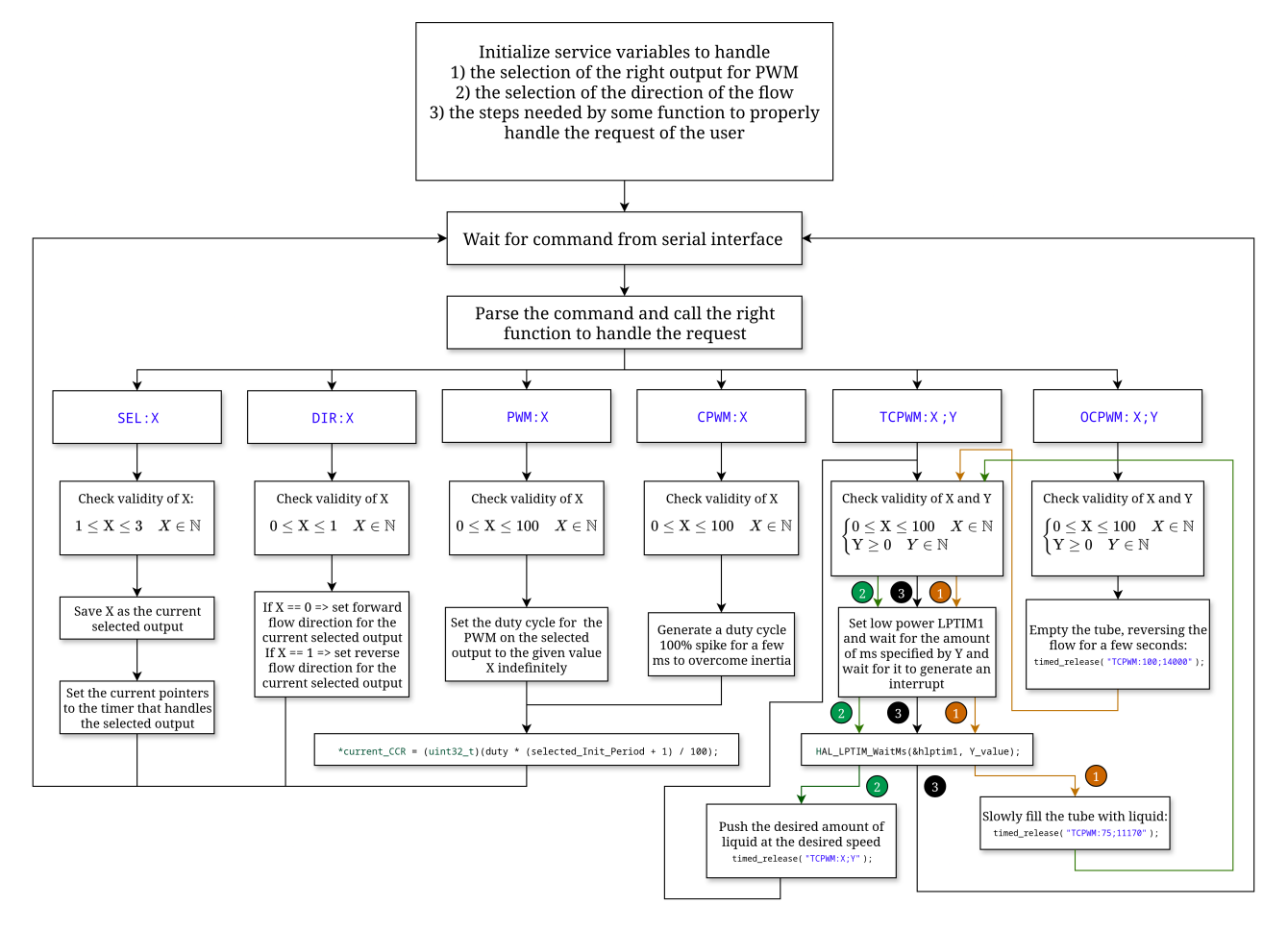


Figure 49: Simplified execution flow of the primitive API system for PWM peristaltic pump control of the microcontroller

The simplified flowchart shown in Figure 49 describes a system for controlling peristaltic pumps using PWM, providing a flexible set of commands for speed control, timed dispensing, and tube clearing. The system starts by listening for a command to be sent over a serial communication link (USB or Bluetooth). When a command arrives, it is parsed. This means the microcontroller analyzes the command to determine what action it should take. Then, it calls a specific function or specific sequence of functions tailored to that command.

Here's a description of the API commands for driving the peristaltic pumps using the custom made firmware:

- SEL:X (Select Output): the internal variables (pointers) are updated to point to the selected output (peristaltic pump).
- DIR:X (Select Direction): sets the desired direction for the currently selected pump, by setting a flag. One of the outputs doesn't support direction inversion. In that cases, an error is returned.

- PWM: X (PWM): sets the PWM duty cycle to the value X, effectively controlling the speed of the currently selected pump. This action is performed indefinitely.
- CPWM:X (Controlled PWM): sets the PWM duty cycle to the value X after performing a brief 100% duty cycle spike. This is used to overcome the pump's inertia, ensuring it starts moving smoothly.
- TCPWM:X:Y (Timed Controlled PWM): sets the PWM duty cycle to the value X after performing a brief 100% duty cycle spike. A low-power timer (LPTIM1) is setup and started. The timer is configured to trigger an interrupt after Y milliseconds have elapsed. This interrupt signal is used to time the dispensing.
- OCPWM:X:Y (Optimized Controlled PWM): reverses the flow of the pump for a defined time (a few seconds) to empty the tube. Then, the tube is slowly filled with water (this should take a predictable time according to the pump's speed) to obtain known initial conditions. This is crucial to make timing a good mechanism for precise dosing. For the three timed controls, the function TCPWM:X:Y is called in rapid succession (to obtain a non-blocking system, a step variable defines what function to call in a switch case code snippet in the same interrupt).

Each time a function encounters an exception, the error's code and description is sent inside a text string via serial communication to the user.

3.3.1 Web interface to test and characterize the available peristaltic pumps

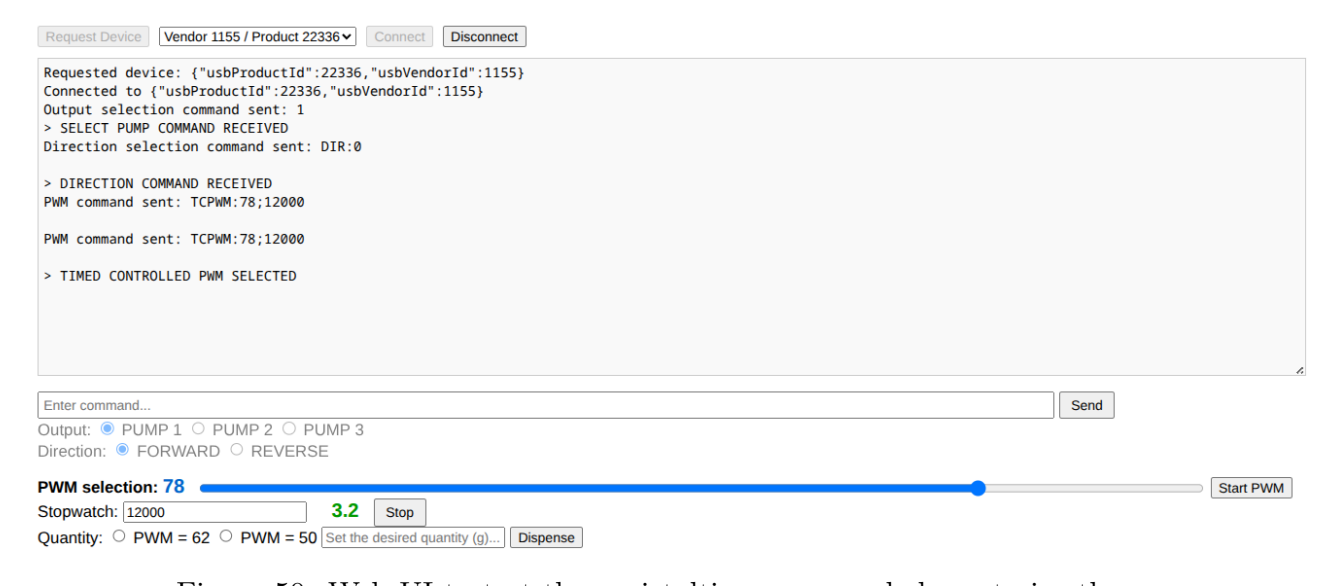


Figure 50: Web UI to test the peristaltic pumps and characterize them.

A simple UI written in HTML, CSS and Javascript was made to pilot the peristaltic pumps and test the custom serial API of the microcontroller (*Figure 50*). The interface handles connection using a operating system agnostic Chromium API to achieve easy multi-platform support. The serial communication log is provided to the user, together with a text field to send a manual command to the microcontroller and some controls to handle the various pumps without

knowing the details of the API. This is an early work in progress and it's just a framework to test the functionalities of the prototype in an easy to install environment.

3.3.2 Measurement cycle flow control

In order to allow the measurement procedure to be fast and cheap for the consumer, a lot of factors should be taken into account. Among them, the most relevant aspects to focus on are:

- Power efficiency: because the device is intended to be battery-powered, every watt-hour must be used efficiently. All electromechanical subsystems (peristaltic pumps, LED driver, mini-spectrometer interface, etc.) should be powered only when they are actively needed. As an example, to keep the initial conditions of the mixing tube consistent, the pump is run at a high flow rate long enough to remove any residual liquid; this flush step, while essential for repeatability, is one of the most power-intensive parts of the cycle. Therefore the firmware must schedule this high-current operation in the shortest possible time (this requires a thorough testing and characterization of the prototype), then immediately place the pumps (and any other idle peripherals) into a shutdown state to eliminate quiescent currents. By dynamically gating power to each circuit block, the system achieves a high duty-cycle efficiency, extending battery life while maintaining the precision required for continuous pH monitoring.
- Deterministic control for repeatability: the flow that drives passive mixing must be reproducible (this is feasible thanks to the properties of laminar flows in microfluidic circuits). The software stack therefore relies on hardware timers and a deterministic scheduler to guarantee that the exact volume of liquid is pumped into each microfluidic channel, and that the flow rate remains stable. This demands tight integration across the mechanical, electronic and software subsystems so that every actuation event is precisely timed and every pump command is executed without introducing excessive errors.
- Software compensation for lower quality hardware: the main role of the machine learning stack is supporting the hardware limitations of cheaper components and compensate their noise sources.

The measurement cycle should start from the system in idle state. First, every sub-system on the PCB is powered down so that the quiescent consumption is minimal. The sequence of operations for the first mixing phase is carried out by the firmware command OCPWM:X;Y, whose diagram is shown in Figure 49. The tubes that pump water into the microfluidic circuit are pumped dry by driving the peristaltic pumps for a short period at a high flow rate. The microcontroller then controls the inlet peristaltic pumps to deliver the exact volumes of tracer solution and water sample into the passive mixing chamber. The command string specifies the number of milliseconds X and the duty cycle percentage of the PWM Y (which defines the flow rate). When the mixed sample reaches the outlet, the microcontroller activates the NTC temperature sensor, reads the value and stores it for the current measurement. The blue-LED driver is switched on for a few milliseconds and the mini-spectrometer is powered up at the same instant. Simultaneously the LED-drift compensation photodiode is sampled; the two measurements are time-aligned so that the received light intensity can be normalised to the instantaneous LED peak. The AS7341 captures the emitted fluorescence on its eight channels

and places the data on the I2C bus. A third peristaltic pump is driven in reverse with a high suction flow: this guarantees that no tracer or sample remains in the outlet tubing, **preventing** carry-over contamination in the next cycle.

The micro-controller forwards all the collected data over the USB-Type-C serial interface to a connected host computer (this data can also be sent over Bluetooth). The host runs the machine-learning pipeline on the received vector and renders the inferred pH value through the web interface.

This **deterministic workflow** keeps power consumption low, synchronizes the optical and electrical events, and guarantees **repeatable**, **contamination-free pH readings**.

3.3.3 Initial hints at a machine learning stack

The spectral measurements recorded by the AS7341 (e.g., those displayed in *Figure 31*) can be supplied to a Support Vector Machine (SVM), a robust supervised learning method suitable for both classification and regression.

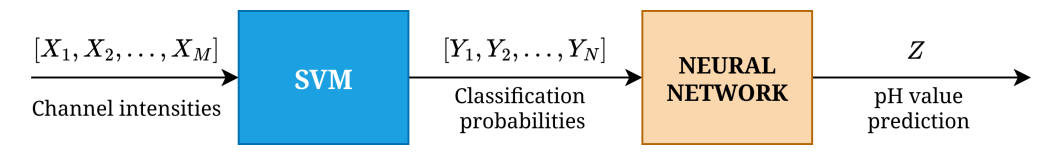


Figure 51: Machine learning data analysis simplified structure

Big limitation of this approach

The SVM model was trained exclusively on data obtained from calibration buffers spaced 0.5pH units apart. Consequently, the maximum distinguishable Δ pH that the model can resolve is limited to the spacing of these test points; finer pH discrimination would require additional training data at intermediate values.

A viable strategy is to analyze the probability outputs of the SVM classifier to map intermediate pH values between two adjacent clusters using a Neural Network (Figure 51). By analyzing how the classifier's probability estimates vary for samples that fall between clusters, one can infer a continuous relationship between the spectral fingerprint and pH, effectively enhancing the measurement resolution. This technique resembles the fingerprinting approach described in 2.5, where the combined intensities of several AS7341 channels are used to generate a unique fingerprint for each buffer. In practice, however, the fingerprint method demands that the AS7341 be characterized experimentally, as simulations alone would not reflect the real-world behavior of the device. In contrast, using the SVM-derived cluster map and adding only a handful of labeled intermediate points allows the model to be refined with substantially less effort and without needing to directly test the mini-spectrometer. Classical, deterministic methods should still be preferred if they achieve comparable accuracy, since they are less reliant on probabilistic inference.

3.3.3.1 Effect of the LED drift on data analysis

In 2.2 it was already mentioned that one of the main goals is to replace a high-end laboratory spectrometer with an inexpensive 8-channel mini-spectrometer. This replacement inevitably reduces the spectral information available to capture the pH-dependent fluorescence.

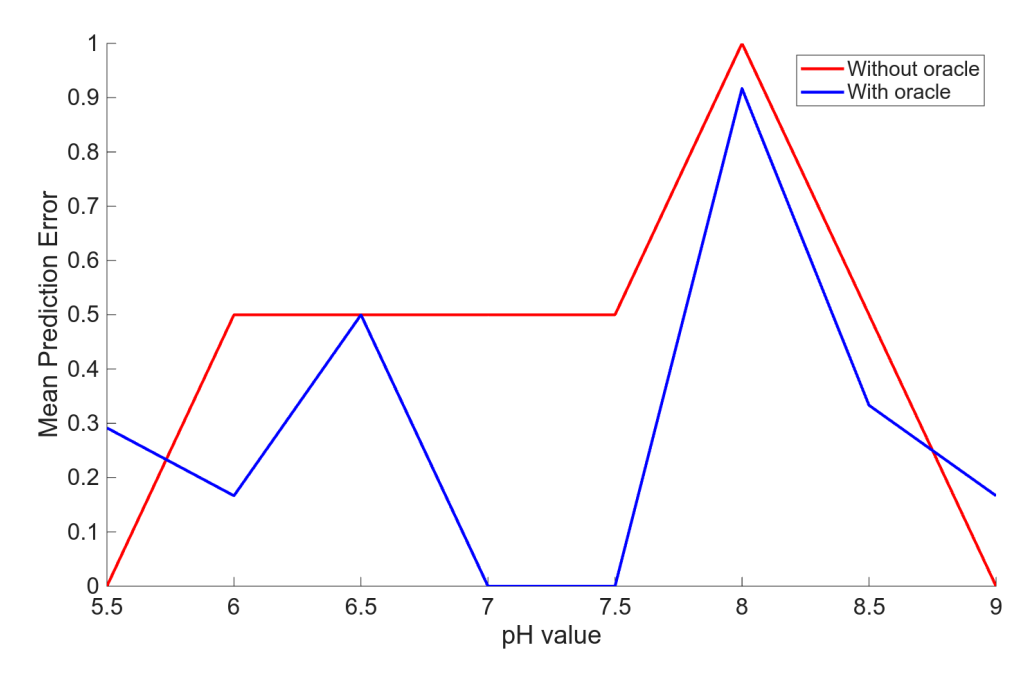


Figure 52: Impact of LED drift on normalization relative to LED Peak

Figure 52 clearly illustrates this limitation: when the data are normalized using the true LED peak (with an imaginary "oracle" that knows the exact, drifting peak wavelength), the SVM prediction error drops markedly compared with normalization performed with a fixed 445 nm channel. Because the LED peak drifts over time (see 2.3), its wavelength shift cannot be tracked by a single fixed-frequency channel. Consequently, the drift has a non-negligible impact on measurement accuracy and must either be compensated (e.g., by real-time LED monitoring, like the one proposed in Figure 28) or mitigated by selecting a more stable light source.

The success rate in correctly predicting the pH of the test sample drops from 51.04% to a markedly lower 25% without the help of the "oracle".

The extremely detrimental effect of an imprecise normalization can be clearly seen by the fact that completely eliminating normalization allows to obtain a far better performance of SVM in this specific case. The correct predictions percentage rises to 75%.

4 Conclusions

The work presented in this thesis represents an initial feasibility study toward a compact, autonomous pH-monitor. Its primary aim was to address a major limitation of inexpensive commercial sensors: the frequent requirement for calibration. The proposed system delivers continuous, self-contained pH measurement; the only user-intervention needed is the periodic refilling of the tracer solution and the removal of the waste liquid that is drawn from the device for analysis. While this waste stream poses no safety hazard, it shouldn't be re-introduced into the measured stream. The prototype is designed to operate autonomously: it will draw a small aliquot from the continuous flow, passively mix this aliquot with a fluorophore-tracker solution, direct the mixture into a dark measurement chamber where the AS7341 mini-spectrometer collects spectral data, simultaneously record auxiliary parameters that influence measurement accuracy, like liquid turbidity, instantaneous LED emission spectrum, and temperature, and route the analyzed liquid to a dedicated waste container for safe disposal. This integrated workflow eliminates the need for manual sampling, tries to maximize measurement precision, and ensures that the analyzed fluid does not re-enter the main process stream. Figure 53 shows the scheme for the prototyped device. The next steps include but are not limited to:

- PCB verification: perform a comprehensive electrical test of the board, including a full characterization of the PWM outputs. Accurate PWM models are needed to predict the timing behavior of the dosing mechanism.
- Microfluidic circuit validation: conduct detailed experiments to confirm that the serpentine + split and recombine architecture can reliably mix the fluorescein-based tracer solution with the sample fluid. Mixing efficiency will be quantified by measuring the homogeneity of the mixture at the outlet that directly affects repeatability.
- Extended pH range: investigate in greater detail the limits imposed by photobleaching in very acidic and very alkaline environments. Strategies to broaden the usable pH window will be explored.
- Mini-spectrometer assessment: evaluate the AS7341's measurement noise and repeatability under tightly controlled chamber conditions. The goal is to determine whether the sensor can deliver the required precision for pH monitoring.
- LED drift compensation: test the proposed normalization circuit to verify that the calculated reference constant effectively reduces the impact of LED drift, especially when the pH resolution is increased. In parallel, potential low-drift LED alternatives will be examined, balancing cost against performance improvements.
- Refinement of the machine-learning pipeline for data analysis: achieving cost-effectiveness for the device inevitably introduces additional noise sources. By refining the machine-learning stack, the system can automatically compensate for the variable noise that affects the measurements, thereby maintaining accuracy without inflating hardware cost.
- Expansion the measurement portfolio: extend the system's analytical capabilities beyond pH to include additional physicochemical parameters.

• Rigorous isolation tests on the measurement chamber: because the primary measurement depends on the fluorescence emitted by the liquid sample, any leakage into the chamber would introduce a significant optical noise source and could render the data unusable.

These steps will refine the prototype, reduce its maintenance requirements, and broaden its applicability to a wider range of pH conditions.

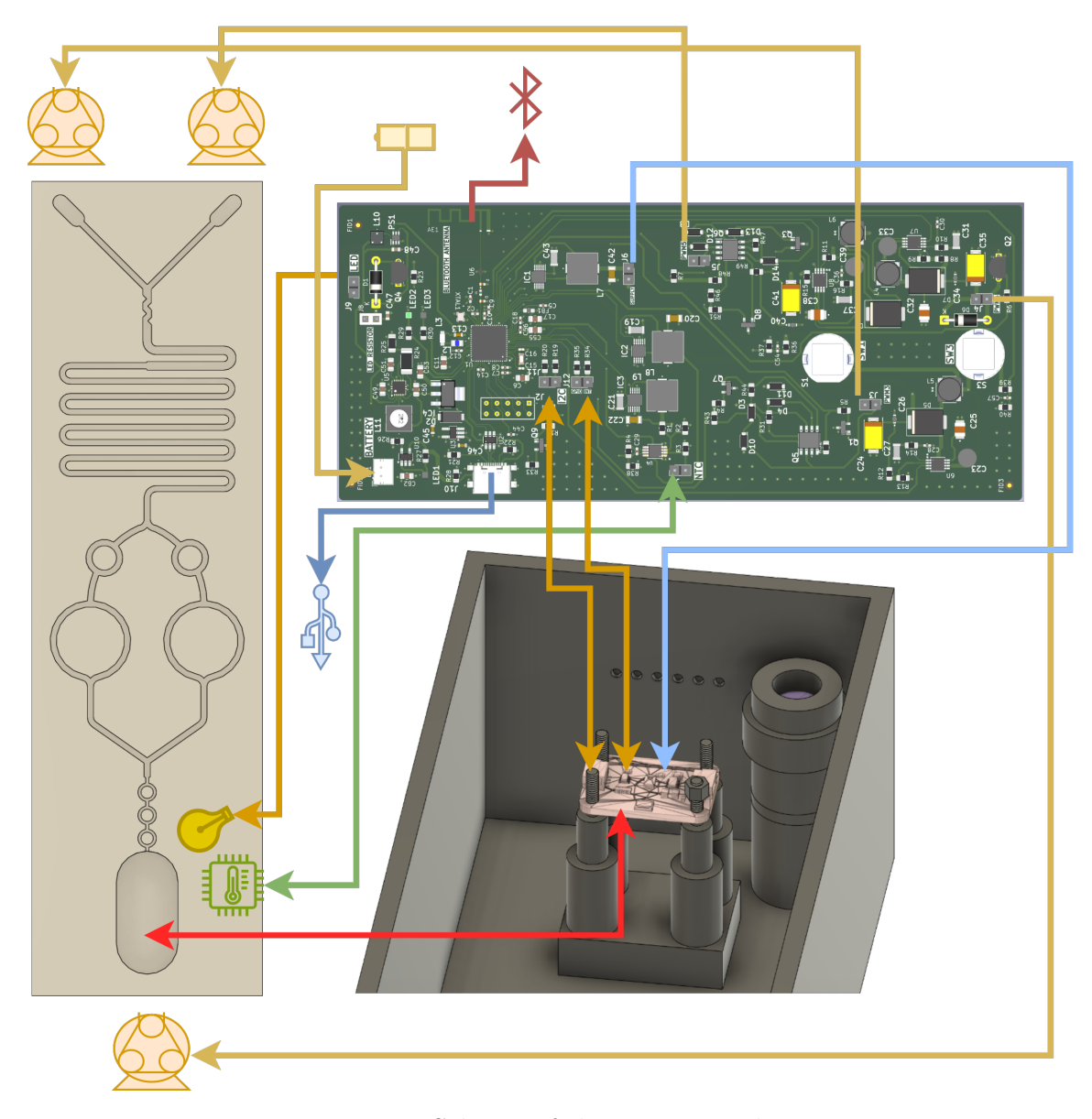


Figure 53: Scheme of the prototype device

Figure 53 shows a visual representation of the main components of the prototyped device.

References

- [1] Misuratore bluelab ph pen. URL https://cdn.idroponica.it/db_img/pdf/Bluelab-pHPen-ManualENG-JAN17.pdf. Datasheet of the pH pen used in the laboratory.
- [2] Franck-condon principle. URL https://it.wikipedia.org/wiki/Principio_di_Franck-Condon. Image taken from Wikipedia.
- [3] D. Ahmed, X. Mao, B.K. Juluri, and et al. A fast microfluidic mixer based on acoustically driven sidewall-trapped microbubbles. *Microfluidics and Nanofluidics*, 7:727–731, 2009. doi: 10.1007/s10404-009-0444-3.
- [4] Liedl G. Bassani, E. and P. Wyder. *Encyclopedia of Condensed Matter Physics. 1st ed.* Elsevier, Amsterdam, 2005.
- [5] A. Di Lorenzo. Combinatorial deposition of thin films: Study of ph variation using fluorescent dyes., 2024. URL https://webthesis.biblio.polito.it/31508/. Tesi magistrale. Rel. Sabrina Grassini, Yuval Golan. Politecnico di Torino, Corso di laurea magistrale in Ingegneria Chimica E Dei Processi Sostenibili, 2024.
- [6] Elveflow. What is pdms soft lithography URL https://elveflow.com/microfluidic-reviews/introduction-about-soft-lithography-and-polymer-molding-for-microfluidic-reviews/introduction-about-soft-lithography-and-polymer-molding-for-microfluidic-reviews/introduction-about-soft-lithography-and-polymer-molding-for-microfluidic-reviews/introduction-about-soft-lithography-and-polymer-molding-for-microfluidic-reviews/introduction-about-soft-lithography-and-polymer-molding-for-microfluidic-reviews/introduction-about-soft-lithography-and-polymer-molding-for-microfluidic-reviews/introduction-about-soft-lithography-and-polymer-molding-for-microfluidic-reviews/introduction-about-soft-lithography-and-polymer-molding-for-microfluidic-reviews/introduction-about-soft-lithography-and-polymer-molding-for-microfluidic-reviews/introduction-about-soft-lithography-and-polymer-molding-for-microfluidic-reviews/introduction-about-soft-lithography-and-polymer-molding-for-microfluidic-reviews/introduction-about-soft-lithography-and-polymer-molding-for-microfluidic-reviews/introduction-about-soft-lithography-and-polymer-molding-for-microfluidic-reviews/introduction-about-soft-lithography-and-polymer-molding-for-microfluidic-reviews/introduction-about-soft-lithography-and-polymer-molding-for-microfluidic-reviews/introduction-about-soft-lithography-and-polymer-molding-for-microfluidic-reviews/introduction-about-soft-lithography-and-polymer-microfluidic-reviews/introduction-about-soft-lithography-and-polymer-microfluidic-reviews/introduction-about-soft-lithography-and-polymer-microfluidic-reviews/introduction-about-soft-lithography-and-polymer-microfluidic-reviews/introduction-about-soft-lithography-and-polymer-microfluidic-reviews/introduction-about-soft-lithography-and-polymer-microfluidic-reviews/introduction-about-soft-lithography-and-polymer-microfluidic-reviews/introduction-about-soft-lithography-and-polymer-microfluidic-reviews/introduction-about-soft-lithography-about-soft-lithography-about-soft-lithography-about-soft-lithography-abo
- [7] EVIDENT. Fluorescence excitation and emission fundamentals. URL https://evidentscientific.com/en/microscope-resource/knowledge-hub/lightandcolor/fluoroexcitation.
- [8] T.S.i.C. Jim Clark. What causes molecus to absorb uv and visible light. URL https://chem.libretexts.org/Bookshelves/Physical_and_Theoretical_Chemistry_Textbook_Maps/Supplemental_Modules_(Physical_and_Theoretical_Chemistry)/Spectroscopy/Electronic_Spectroscopy/Electronic_Spectroscopy_Basics/What_Causes_Molecules_to_Absorb_UV_and_Visible_Light.
- [9] F. Le Guern, V. Mussard, A. Gaucher, M. Rottman, and D. Prim. Fluorescein derivatives as fluorescent probes for ph monitoring along recent biological applications. *Int J Mol Sci*, 21(23):9217, 2020. doi: 10.3390/ijms21239217.
- [10] PubChem. Sodium fluorescein, 2024. URL https://pubchem.ncbi.nlm.nih.gov/compound/Sodium-Fluorescein. Accessed: 2025-08-22.
- [11] Wasim Raza, Shakhawat Hossain, and Kwang-Yong Kim. A review of passive micromixers with a comparative analysis. *Micromachines*, 11:455, 04 2020. doi: 10.3390/mi11050455.
- [12] Thermo Fisher Scientific. Photobleaching principles, 2023. URL https://www.thermofisher.com/it/en/home/life-science/cell-analysis/cell-analysis-learning-center/molecular-probes-school-of-fluorescence/fluorescence-basics/fluorescence-fundamentals/photobleaching-principles. html. Accessed: 2023-10-15. This is a commercial source; consult peer-reviewed literature for authoritative information on photobleaching mechanisms.